University of Strathclyde Glasgow

DEPARTMENT OF PHYSICS

Optimisation and control of high intensity laser accelerated ion beams

by

Olivier TRESCA

in partial fulfilment of the requirements for the degree of
Doctor of Philosophy in Physics

2012

Copyright Declaration

This thesis is the result of the author's original research. It has been composed by the author and has nor been previously submitted for examination which has led the award of a degree.

The copyright of the thesis belongs to the author under the terms of the United Kingdom Copyright Act as qualified by University of Strathclyde Regulation 3.50. Due acknowledgement must always be made of the use of any material contained in, or derived from, this thesis.
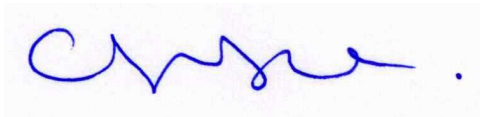
Signed:

Date:
February 23, 2012

Remember that all models are wrong, the practical question is how wrong do they have to be to not be useful.

George E. P. Box

Abstract

The interaction of a laser pulse of relativistic intensity ($\geq 1 \times 10^{18}$ Wcm^{-2}) with a solid target results in the creation of a quasi-electrostatic field at the rear surface of the target. This field is strong enough (TVm^{-1}) to ionise and accelerate ions from the target surface via the Target Normal Sheath Acceleration (TNSA) mechanism. The resulting beam has many desirable properties for a large range of potential applications. The work presented in this thesis aims at optimising and controlling the ion beam properties.

Firstly, an investigation of laser driven ion acceleration using ultrahigh contrast (10^{10}), ultrashort (50 fs) laser pulses focused to intensities up to 10^{21} Wcm^{-2} on thin foil targets is presented. It is found that irradiation at normal (0°) incidence produces higher energy ions than oblique incidence (35°), contrasting sharply with previous work at lower intensities. These findings are confirmed by 1D boosted PIC simulations and can be explained by the acceleration of fast electrons being dominated by a new absorption process. The effects of target composition and thickness on the acceleration of carbon ions are also discussed and compared to calculations using analytical models of ion acceleration.

Next, an investigation of the transverse refluxing of fast electrons in targets of limited lateral size is reported. The targets were irradiated by high intensity ($\sim 1 \times 10^{19}$ Wcm^{-2}), picosecond laser pulses. The maximum energy of the resulting TNSA proton beams is found to increase with decreasing target surface area. This is explained by the presence of a laterally spreading electron population that reflects off the target edges and enhances the TNSA accelerating field. In addition it is demonstrated that this laterally refluxing electron population can be used to control the spatial intensity distribution of the TNSA proton beam, by changing the geometry of the target. This technique offers encouraging prospects for many applications of laser accelerated ions.

Finally, a characterisation study of debris emission generated by the interaction of high power laser pulses with solid targets is presented. Targets of thickness ranging from 1 mm to 5 nm were irradiated by high intensity ($\sim 1 \times 10^{20}$ Wcm^{-2}), picosecond laser pulses. The resulting debris emission is found to be directed along the target normal axis at both the rear and front of the target. The front emission profile is found to be similar to a plasma expansion profile. Hollow debris depositions of radius increasing with target thickness are measured from the target rear surface. This emission profile is explained by the propagation and breakout of a laser driven shock at the rear of the target.

Acknowledgements

The work presented in this thesis is the result of three years of research done in collaboration with a number of people who deserve all my gratitude.

First and foremost, I would like to thank my PhD supervisor, Prof. Paul McKenna. His continuous support and encouragements in addition to his patience and attention to detail have been most valuable during those three years. I must also thank him for the host of invaluable opportunities he made available to me, without which this thesis would have never been completed.

I would also like to thank Dr David C. Carroll and Dr Xiaohui H. Yuan whose seemingly endless knowledge of laser driven ion acceleration and willingness to help have been precious over the last three years. Their dedication and work ethic has been the cornerstone of the many successful experimental campaigns I had the chance to be involved in.

My gratitude also goes to my fellow PhD students at the University of Strathclyde Ross Gray, Mireille Coury, David MacLellan, Haydn Powel, Ceri Brenner, Pablo Gallegos and particularly Mark N. Quinn with whom I had the pleasure of sharing an office for three years. They have provided me with much needed distractions from my everyday office work and made the life on experiment more enjoyable.

This work was carried out as part of the LIBRA consortium including a large number of UK based research groups. Our closest collaborators were Prof David Neely of the Central Laser Facility, Prof. Marco Borghesi and Prof. Matt Zepf of the Queen's University Belfast and Prof. Zulfikar Najmudin of the Imperial College London. Other collaborations were also made with groups based at the PHELIX department at GSI lead by Prof. Thomas Kühl, The Beijing National Laboratory lead by Prof. Yutong Li and the Ecole Polytechnique lead by Dr. Julien Fuchs.

The experimental campaigns would not have been possible without the help of the support staff at the different facilities. Peta Foster at GEMINI, Bernhard Zielbauer at PHELIX and Kate Lancaster at VULCAN, you have my utmost gratitude for your precious help. I would also like to thank the laser technicians of the Central Laser Facility and PHELIX whose commitment to the prompt delivery of the best possible laser pulses made this work a reality. A special thank goes to Dr Chris Spindloe and the target fabrication team at the CLF.

I also have to thank Dr Alex P. L. Robinson of the CLF and Prof. Roger G. Evans of Imperial College London for providing the much needed simulation support.

Finally, I would also like to thanks the great people I have met in Glasgow

over the last three years, and particularly the members of the Glasgow Sharks for providing me with a weekly escape from the world of high power lasers.

Ces remerciements ne seraient pas complets sans une mention à toutes les personnes qui m'ont accompagné tout au long de mes études en France, et particulièrement à Annie Soulayrol sans qui je n'aurais peut-être pas choisi d'étudier la physique. Je tiens aussi à remercier mes amis les plus chers Pablo, Annette et David qui m'ont apporté tant de choses depuis de nombreuses années. Il me faut également remercier mes parents et mes frères pour leur soutien sans faille depuis toujours. Enfin, du plus profond de mon cœur, un grand merci à Katherine qui a transformé mon séjour en Ecosse en l'un des meilleurs moments de ma vie.

Role of the author

The work presented in this thesis is the result of a collaborative effort of researchers from various institutions and is performed within the context of the LIBRA (Laser Induced Beams of Radiation and their Applications) project. The author is the main contributor to the analysis and was heavily involved in the experimental campaigns for the work presented in this thesis.

Chapter 5: The author played a key role during the experimental campaign. He was responsible for installing and running the Thomson parabola ion spectrometers used to measure the ions with help from R. Prasad (Queens University Belfast). The secondary cleaning laser was set up by the author with help from Dr. D. C. Carroll (University of Strathclyde). The author had a leading role in the extraction and analysis of the data. Analysis of the target composition effect was carried out by Dr. D. C. Carroll. The 1D boosted PIC simulations presented in section 5.6 were performed by Dr. A. P. L Robinson (Central Laser Facility).

Chapter 6: The author played a major role in planning and running the experiment. The proton dosimetry film stacks were designed, assembled and scanned by the author. The optical probe was operated by Dr. B. Zielbauer (GSI). The $K\alpha$ imager was designed and ran by Dr. X. H. Yuan (University of Strathclyde). The analysis presented in this chapter was principally conducted by the author with the exception of the Hybrid-PIC simulations done by Prof. R. G. Evans (Imperial College London). The electron lateral spreading model used for the analysis was developed by the author. Dr. M. N. Quinn (University of Strathclyde) wrote the code used to estimate the proton spatial intensity distribution from the TNSA field distribution.

Chapter 7: The author played a major role in planning and running the experiment. The author was responsible for the installation of Thomson parabola spectrometers as well as running the other diagnostics (dosimetry film stacks, $K\alpha$ imager and spectrometer and electron spectrometer). The glass plates used to collect the debris were also the responsibility of the author. The totality of the data presented in this chapter were extracted and analysed by the author. The model developed in this chapter is the work of the author.

List of publications

Publications directly resulting from the work presented in this thesis

1. **"Carbon ion acceleration from thin foil targets irradiated by ultra high contrast ultra intense laser pulses"**, D. C. Carroll, **O. Tresca**, R. Prasad, L. Romagnani, P. S. Foster, P. Gallegos, S. Ter-Avetisyan, J. S. Green, M. J. V. Streeter, N. Dover, C. A. J. Palmer, C. M. Brenner, F. H. Cameron, K. E. Quinn, J. Schreiber, A. P. L. Robinson, T. Baeva, M. N. Quinn, X. H. Yuan, Z. Najmudin, M. Zepf, D. Neely, M. Borghesi and P. McKenna, *New Journal of Physics*, **12**, 045020, 2010.

2. **"Controlling the properties of ultra-intense laser-proton sources using transverse refluxing of hot electrons in shaped mass-limited targets"**, **O. Tresca**, D. C. Carroll X. H. Yuan, B. Aurand, V. Bagnoud, C. M. Brenner, M. Coury, J. Fils, R. J. Gray, T. Kühl, C. Li, Y. T. Li, X. X. Lin, M. N. Quinn, R. G. Evans, B. Zielbauer, M. Roth, D. Neely and P. McKenna, *Plasma Physics and Controlled Fusion*, **53**, 10, 2011

Additional publications resulting from PhD work

3. **"Calibration of Thomson parabola-MCP assembly for multi-MeV ion spectroscopy"**, R. Prasad, D. Doria, S. Ter-Avetisyan, P. S. Foster, K. E. Quinn, L. Romagnani, C. M. Brenner, J. S. Green, P. Gallegos, M. J. V. Streeter, D. Carroll, **O. Tresca**, N. Dover, C. A. J. Palmer, J. Schreiber, D. Neely, Z. Najmudin, P. McKenna, M. Zepf and M. Borghesi, *Nuclear Instruments & Methods in Physics Research Section A: Accelerators Spectrometers Detectors and Associated Equipment*, **6232**, 712-715, 2010.

4. **"Spatially resolved X-ray spectroscopy using a HOPG crystal"**, X. H. Yuan, D. C. Carroll, M. Coury, R. J. Gray, C. M. Brenner, X. X. Lin, Y. T. Li, M. N. Quinn, **O. Tresca**, and B. Zielbauer, D. Neely, and P. McKenna, *Nuclear Instruments and Methods in Physics Research Section A: Accelerators, Spectrometers, Detectors and Associated Equipment*, **6531**, 145-149, 2011.

5. **"Relativistic plasma surfaces as an efficient second harmonic generator"**, M. J. V. Streeter, P. S. Foster, F. H. Cameron, M. Borghesi, C. M. Brenner, D. C. Carroll, E. Divall, N. P. Dover, B. Dromey, P. Gallegos, J. S. Green, S. Hawkes, C. J. Hooker, S. Kar, P. McKenna, S. R. Nagel, Z. Najmudin, C. A. J. Palmer, R. Prasad, K. E. Quinn, P. P. Rajeev, A. P. L.

Robinson, L. Romagnani, J. Schreiber, C. Spindloe, S. Ter-Avetisyan, **O. Tresca**, M. Zepf and D. Neely, *New Journal of Physics*, **13**, 023041, 2011.

6. **"Refluxing of fast electrons in solid targets irradiated by intense, picosecond laser pulses"**, M. N. Quinn, X. H. Yuan, X. X. Lin, D. C. Carroll, **O. Tresca**, R. J. Gray, M. Coury, C. Li, Y. T. Li, B. Aurand, J. Fils, T. Kühl and P. McKenna, *Plasma Physics and Controlled Fusion*, **532**, 025007, 2011.

7. **"Scintillator based ion beam profiler for diagnosing laser accelerated ion beams"**, J. S. Green, M. Borghesi, C. M. Brenner, D. C. Carroll, N. P. Dover, P. S. Foster, P. Gallegos, S. Green, D. Kirby, k. J. Kirkby, P. McKenna, M. J. Merchant, Z. Najmudin, C. A. J. Palmer, D. Parker, R. Prasad, K. E. Quinn, P. P. Rajeev, M. P. Read, L.; Romagnani, J. Schreiber, M. J. V. Streeter, **O. Tresca**, C-G. Wahlström, M. Zepf and D. Neely, *Laser Acceleration of Electrons, Protons and Ions and Medical Applications of Laser-Generated Secondary Sources of Radiation and Particles*, Proceedings of SPIE: The International Society for Optical Engineering, **8079**, 807919, 2011.

8. **"Ion source development and radiobiology applications within the LIBRA project"**, M. Borghesi, S. Kar, R. Prasad, F. K. Kakolee, K. E. Quinn, H. Ahmed, G. Sarri, B. Ramakrishna, B. Qiao, M. Geissler, S. Ter-Avetisyan, M. Zepf, G. Schettino, B. Stevens, M. Tolley, A. Ward, J. S. Green, P. S. Foster, C. Spindloe, P. Gallegos, A. P. L. Robinson, D. Neely, D. C. Carroll, **O. Tresca**, X. H. Yuan, M. N. Quinn, P. McKenna, N. P. Dover, C. A. J. Palmer, CJ. Schreiber, Z. Najmudin, I. Sari, M. Kraft, M. Merchant, J. C. Jeynes, K. Kirkby, F. Fiorini, D. Kirby, and S. Green, *Laser Acceleration of Electrons, Protons and Ions and Medical Applications of Laser-Generated Secondary Sources of Radiation and Particles*, Proceedings of SPIE: The International Society for Optical Engineering, **8079**, 80791E, 2011.

9. **"Effect of Lattice Structure on Energetic Electron Transport in Solids Irradiated by Ultraintense Laser Pulses"**, P. McKenna, A. P. L. Robinson, D. Neely, M. P. Desjarlais, D. C. Carroll, M. N. Quinn, X. H. Yuan, C. M. Brenner, M. Burza, M. Coury, P. Gallegos, R. J. Gray, K. L. Lancaster, Y. T. Li, X. X. Lin, **O. Tresca** and C-G. Wahlström, *Physical Review Letters*, **106**, 185004, 2011.

10. **"Fast ion acceleration from thin foils irradiated by ultra-high intensity, ultra-high contrast laser pulses"**, R. Prasad, A. A. Andreev, S. Ter-Avetisyan, D. Doria, K. E. Quinn, L. Romagnani, C. M. Brenner, D. C. Carroll, N. P. Dover, D. Neely, P. S. Foster, P. Gallegos, J. S. Green, P. McKenna, Z. Najmudin, C. A. J. Palmer, J. Schreiber, M. J. V. Streeter, **O. Tresca**, M. Zepf, and M. Borghesi , *Applied Physics Letters*, **99**, 121504, 2011.

11. **"Surface transport of energetic electrons in intense picosecond laser-foil interactions"**, R. J. Gray, X. H. Yuan, D. C. Carroll, C. M. Brenner, M. Coury, M. N. Quinn, **O. Tresca**, B. Zielbauer, B. Aurand, V. Bagnoud, J. Fils, T. Kühl, X. X. Lin, C. Li, Y. T. Li, M. Roth, D. Neely, and P. McKenna, *Applied Physics Letters*, **99**, 171502, 2011.

12. **"Influence of laser irradiated spot size on energetic electron injection and proton acceleration in foil targets"**, M. Coury, D. C. Carroll, A.P.L. Robinson, X. H. Yuan, C. M. Brenner, M. Burza, R. J. Gray, M. N. Quinn, K. L. Lancaster, Y. T. Li, X. X. Lin, **O. Tresca,** C.-G. Wahlström, D. Neely, and P. McKenna, *Applied Physics Letters*, **100**, 074105, 2012.

Contents

List of Figures

List of Tables

Chapter 1

Introduction

With the advent of particle physics in the early 20th century various methods were developed to accelerate charged particles to ever increasing energy using electric fields. The first particle accelerators developed in the 1920's used simple electrostatic fields to accelerate particles. In 1928, Wilderøe [1] proposed to use a series of oscillating electric fields along a linear beam line to accelerate charged particles and in 1929 Lawrence [2] suggested that similar electric fields be applied to particles trapped in orbits using magnetic fields. These two ideas form the basis of the LINAC and cyclotrons accelerators, both of which are still widely used today.

In the case of a LINAC greater energy can be achieved by adding successive accelerating cavities of increasing length. For example, electrons with energies of up to 50 GeV can be obtained at the Stanford Linear Accelerator Center (SLAC) over an acceleration length of 3 km. For a cyclotron accelerator the particles can only be accelerated if they stay in phase with the oscillating field. If the frequency of the oscillations is kept constant it is not possible to accelerate particles above a few percent of the speed of light. To overcome this limitation, cyclotrons with oscillating fields of varying frequencies have been developed, the synchrocyclotrons. Synchrotron accelerators are similar to synchrocyclotrons in that they accelerate particles using field frequencies adjusted to the particles energy, but the radius of the particles orbit is kept constant by using a varying magnetic field. Synchrotrons are able to accelerate charged particles to much

higher energies than all other types of accelerators. The recently completed Large Hadron Collider (LHC) is a synchrotron capable of accelerating protons up to 7 TeV and Pb nuclei up to 574 TeV.

In the case of a synchrotron the size of the machine is determined by the strength of the magnetic field used to contain the particles. In the case of the LHC the circumference of the ring is approximately 27 km making it a very large and expensive machine. For a LINAC, the RF cavities used to accelerate the particles have an acceleration gradient of 10-50 MeVm^{-1}, which means that in order to reach energies equivalent to the LHC the acceleration length has to be in excess of 100 km, making such a machine cost prohibitive.

In the 1960s, shortly after the laser was first demonstrated it was realised that energetic ions were emitted from laser produced plasmas [3]. Ions with energies in the keV-MeV range have been measured with a wide range of laser parameters, for pulse durations ranging from 25 ps to 120 ns and intensities from 10^9 Wcm^{-2} to 10^{16} Wcm^{-2} [4]. This ion emission is the result of large electric fields present at the front of the target generated by charge separation. It is believed that large self generated magnetic fields produced in the laser-solid interaction are responsible for this charge separation [5].

However, it is only in the last 15 years that the relativistic laser-plasma regime has been reached using ultra intense laser pulses ($> 10^{18}$ Wcm^{-2}) resulting in high energy charged particle beams. Electron beams of energy in the GeV range have been demonstrated using wakefield acceleration in underdense plasmas [6–9]. This is achieved over a distance of a few millimetres with an accelerating gradient approximately 1000 times greater than in RF cavities [10]. This technique could be used to build table top laser driven accelerators capable of reaching energies greater than 1 GeV.

1.1   Laser driven ion acceleration

In the last decade it has become possible to generate high energy ion beams using high power lasers with intensities in the relativistic regime [11–13]. The

energy of the ions in those beams can reach multi-MeV and the maximum energy is generally found to scale with the laser intensity I_L and wavelength λ_L as $\propto \sqrt{I_L \lambda_L^2}$. These beams are accelerated over a short distance (a few microns) and in a short time (of the order of the laser pulse duration - tens of femtoseconds to picoseconds [14]).

Various mechanisms are responsible for the acceleration of ions in laser-plasma interaction. They can be accelerated via simple expansion of the laser generated plasma into vacuum. Or, if the electrons are expelled from the plasma by the laser, the Coulomb force between the ions can accelerate them via the Coulomb explosion mechanism. For laser intensities in the ultra-relativistic regime ($>10^{20}$ Wcm^{-2}), the laser ponderomotive force and radiation pressure are mainly responsible for the acceleration of the ions, as described in chapter 3.

The most widely investigated laser-driven ion acceleration scheme is the Target Normal Sheath Acceleration (TNSA) mechanism. The laser is incident on the front surface of the target and creates a plasma. A fraction of the energy contained in the laser pulse is transferred to the electrons via different absorption mechanisms described in chapter 2. This resulting fast electron population propagates through the target. Upon reaching the opposite (rear) surface, this electron population breaks out into the vacuum and generates a strong quasi-electrostatic field ($\sim$TVm^{-1}) responsible for the ionisation of the target surface and the acceleration of the resulting ions. This mechanism will be described in detail in chapter 3. Fig. 1.1 gives a summary of the different stages of the laser driven TNSA ion acceleration mechanism.

The resulting ion beams have been reported to be very bright, $>10^{12}$ ions per pulse, and to have a very low longitudinal and transverse emittance, $<4\times10^{-3}$ mm.mrad [15]. The highest proton energy reported to this date is $\sim$70 MeV [16], although recent reports suggest the detection of protons with energies above 100 MeV measured using the TRIDENT laser at the Los Alamos National Laboratory. Compared to LINACs and synchrotrons the acceleration occurs over a very short distance of the order of a few microns. These properties make laser driven ion beams highly desirable for a wide range of applications, some of which are
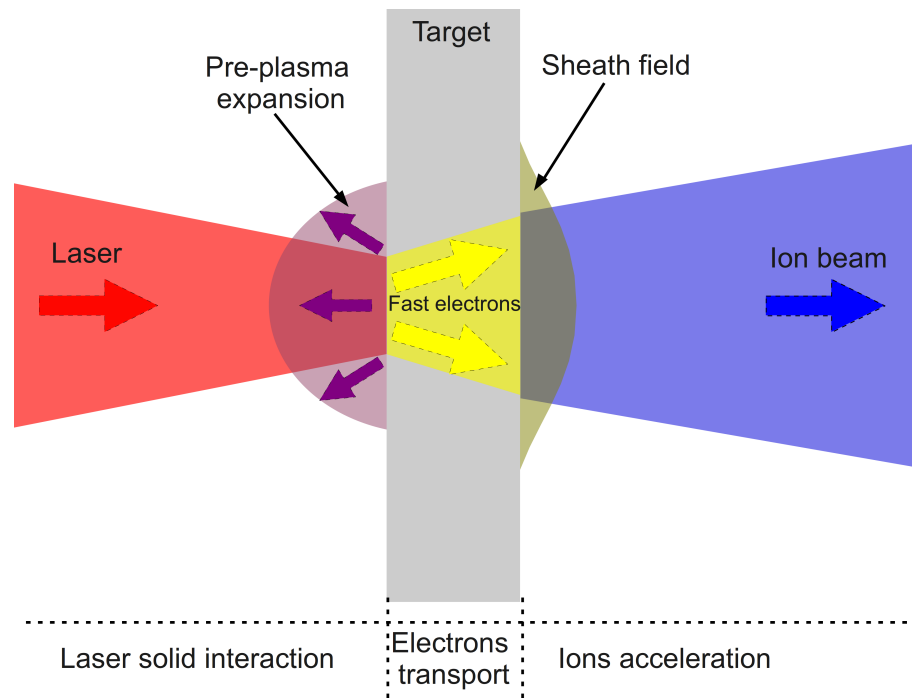
Figure 1.1: Schematic of the TNSA ion acceleration mechanism. A detailed explanation is given in chapter 3

introduced in the following section.

1.2 Applications of laser driven ion beams

1.2.1 Medical applications

Ion oncology

The use of protons to irradiate cancer tumours was first proposed in 1946 by Wilson [17] and the first patients were treated 10 years later using facilities primarily built for scientific research. Heavier ions such as carbon ions have also been used to irradiate tumours [18]. Today, dedicated facilities are operated based on LINAC or cyclotron technology [19–21], but their number remain limited as they are expensive to build. Currently there are only 38 facilities in operation, mainly in Japan and the USA, with 25 more being built. Approximately 100 000 patients have been treated worldwide [22].

A proton therapy centre consists of an ion accelerator, such as a cyclotron,

connected to various delivery systems, as shown in Fig. 1.2 (c). Most commonly, the beams are delivered to the patient in a fixed horizontal geometry with the patient simply seating at the end of the beam line. This is usually used to treat ocular tumours. Alternatively, a rotating gantry can be used to direct the ions to any part of the body. The use of gantries enables a large variety of tumours to be treated, but is expensive to build and requires a lot of space due to the large magnets required to steer the high energy ion beam, as seen in Fig. 1.2 (d).

The use of ions to irradiate tumours located deep inside the body has many advantages over the other radiological techniques using X-rays or electrons. The main advantage with ions is that as they propagate inside a material they deposit most of their energy at a given depth, in the Bragg peak. In the case of X-rays or electrons the energy deposition tends to remain quite high for most of the propagation depth of the radiation, as shown in Fig. 1.2 (a). The presence of a fixed stopping range for ions means that it is possible to irradiate a tumour with minimal damage to the surrounding healthy tissue, as is shown in Fig. 1.2 (b). Depending on how deep the targeted tumour is in the body the required proton energy is between 60 MeV and 250 MeV.

Laser driven ion sources have attracted interest as potential ion beam driver for proton oncology facilities [26–30] due to their compactness and potentially lower cost compared to conventional LINAC and synchrotron ion accelerators. The use of a laser as an ion driver would make the use of multiple treatment rooms easier as it is much simpler to transport a laser beam than a particle beam. In such a scenario the acceleration of the ions by the laser could potentially take place in the treatment room [26]. This would however require a great deal of control of the laser generated ion source. A more flexible option would be to use the laser driven ion beam as a high energy injector for a more conventional accelerator [31].

Radioisotope production

Laser driven ion beams, when incident on a secondary target, can be used to produce radioisotopes. This technique can potentially be applied to medical pur-
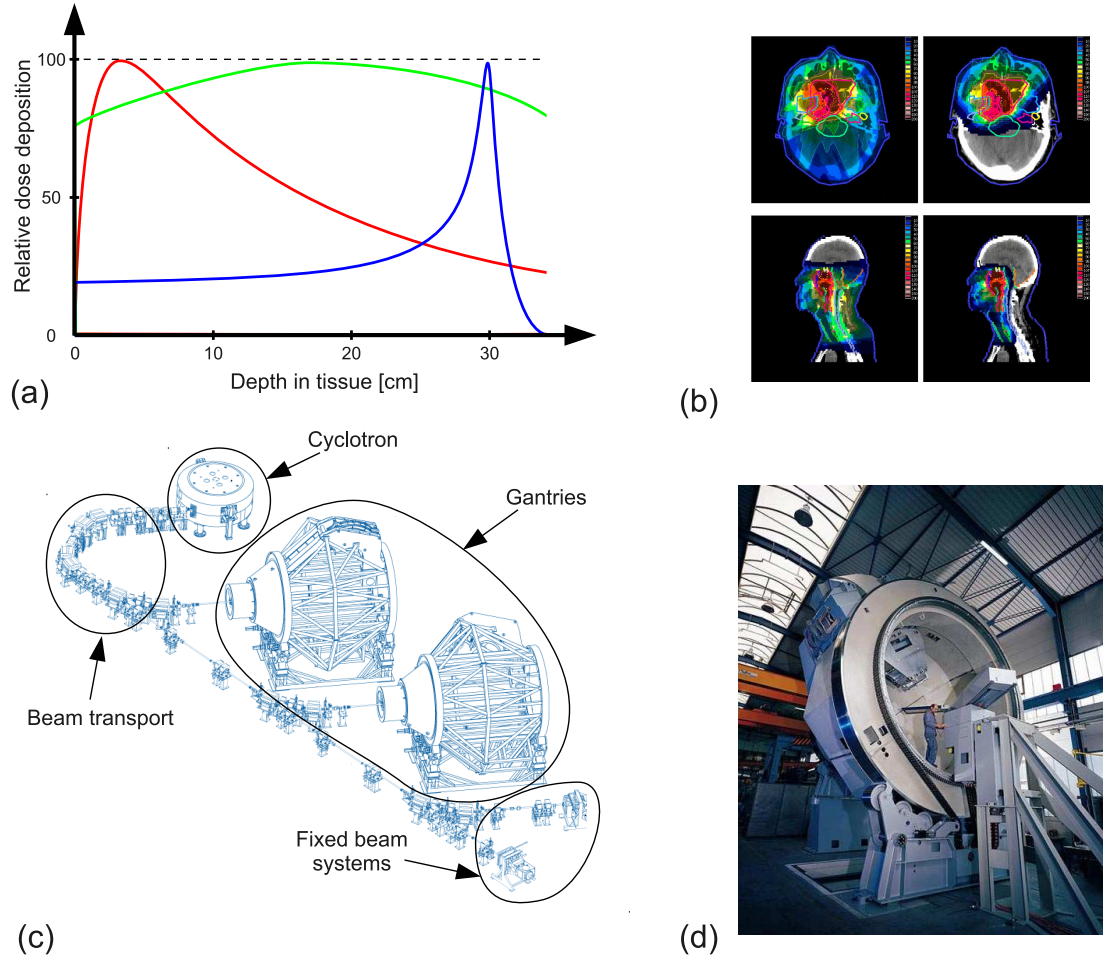
Figure 1.2: (a) Difference in the dose deposition as a function of the penetration depth in tissue for different radiations (green 250 MeV electrons, blue 250 MeV protons and red 20 MeV X-ray); (b) difference in the dose deposition inside a patient with X-rays (left column) and protons (right column) [23]; (c) schematic of a proton therapy facility [24]; (d) a gantry used to direct proton beams under construction [25].

poses such as Positron Emission Tomography (PET) [32]. The short lived low-Z isotopes, typically ^{11}C, ^{13}N or ^{15}O, are bounded to a pharmaceutical given to the patient. The organ that metabolises the pharmaceutical can be imaged by detecting the positron emission from the isotope. To this date the activities produced with laser driven ion beams are too low to be used in the medical field.

However, laser driven isotope sources have many advantages. Due to the short life of the isotopes, they have to be produced near the treatment facility. This can be easily done using the same laser facility as the one used for ion oncology simply by changing the target configuration. In addition, the production of X-

rays and γ-rays used for medical imaging can also be achieved via laser plasma interaction. This means that one laser driver can be used for multiple applications in one medical facility.

1.2.2 Inertial confinement fusion (ICF)

After the second world war large efforts were conducted by the military to exploit the energy released by the fusion of light elements. Consequently the first ever man made fusion reaction occurred in 1951 when the Ivy Mike device was detonated in the Pacific ocean by the US military [33]. At the same time, attempts to control fusion reactions were already taking place, mostly in the UK where George Thomson and Moses Blackman filed the first patent for a fusion reactor in 1946 [34]. Since then the plasma physics community has been working towards achieving controlled nuclear fusion in the hope of using it as a cheap and almost limitless energy source.

Multiple fusion reactions can be used in order to release energy, but the easiest one to achieve is the D-T reaction:

$$D + T = He + n \tag{1.1}$$

It has a maximum cross section at a temperature of about 64 keV, and each reaction releases 17.6 MeV of energy, shared between the alpha particle (3.5 MeV) and the neutron (14.1 MeV). The conditions necessary to sustain a fusion reaction are not trivial to achieve. They are defined using the Lawson criteria [35] which in the case of the D-T reaction is:

$$n\tau > 1.5 \times 10^{20}\,\mathrm{sm^{-3}} \tag{1.2}$$

where n is the plasma density and τ is the confinement time. There are two main approaches to satisfy the Lawson criteria, one is to confine for a long duration a low density plasma, the Magnetic Confinement Fusion (MCF) approach. The other is to use a highly compressed plasma contained for a very short period of

time, the Inertial Confinement Fusion (ICF) approach.

Shortly after the laser was first demonstrated Nuckolls *et al.* proposed to use lasers as a driver for ICF [36]. A large number of laser beams are focused on a spherical cryogenic pellet containing the D-T fuel in gaseous and solid form. The resulting ablation of the pellet surface launches a spherical shock wave inside the fuel compressing it to the required density. Once the compression of the fuel is sufficient, fusion reactions will occur igniting the pellet. As the fuel starts to burn the highly energetic neutrons escape the target and are captured and used to generate electricity while the less energetic alpha particles are absorbed by the cold fuel and heats it up sufficiently to sustain a burn wave which propagates outwards in the fuel. The resulting self sustaining burn wave propagates through the fuel until all of it has ignited. The different steps of these process are summarised in Fig. 1.3 (a-c).
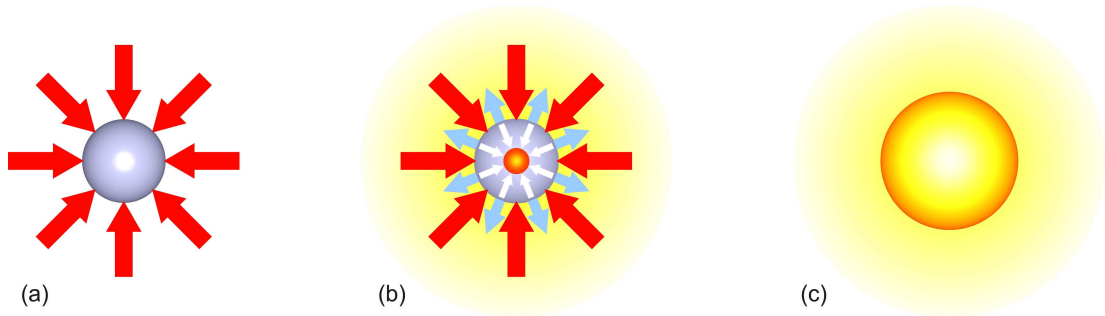
Figure 1.3: Different stages of the direct drive approach to ICF. (a) A large number of laser beams are focussed on a spherical fuel pellet. (b) The resulting ablation of the surface launches a shock wave that compresses the fuel. Upon reaching the right density and temperature conditions the fusion reactions are triggered and the fuel ignites. (c) The remaining of the fuel is burnt by fusion reactions generating a large quantity of energy.

The approach in which the lasers are directly focused on the fuel pellet is called the direct drive approach. However in order to obtained ignition the compression of the pellet must be highly homogeneous. Any irregularity in the pellet surface or the laser beams spot will trigger hydrodynamic instabilities which will prevent the ignition and burn being achieved. In order to circumvent this issue the indirect drive approach has been developed. This involves encapsulating the fuel pellet in a high Z material case, a hohlraum. The laser beams are then focussed on the

inner walls of the hohlraum where they are converted to X-rays. The X-rays act to compress the pellet until ignition occurs. This technique relaxes the constraints on the uniformity of the laser beams and allow for a much more symmetrical illumination of the pellet making the compression of the fuel easier. However, the main drawback of this approach is the extra laser energy required due to the losses occurring during the X-ray generation. This is the approach taken by the National Ignition Facility (NIF) project in the USA which aims to achieve ignition by the end of 2012.

The fast ignition approach

Both the direct and indirect drive approach rely on a high compression of the fuel to trigger the fusion reactions. Tabak *et al.* [37] proposed in 1994 an alternative scheme in which the compression and ignition stage are decoupled, called the fast ignition approach. In this scheme, a high intensity laser pulse is focussed on the compressed pellet to ignite the fuel. To do this a third laser can be used to bore a channel in the expanding ablation plasma, to enable the ignition beam to propagate to the compressed fuel. Alternatively, a cone of high Z material (gold) can be used to contain the plasma expansion, leaving a clear path for the ignition beam.

One of the main advantages of using an external source to ignite the fuel is that the required compression density is lower ($\sim$300-400 gcm^{-3}) than in the direct or indirect drive approach ($\sim$1000 gcm^{-3}). This means that the energy of the compression lasers can be greatly reduced (300 kJ compared to >1 MJ) and the compression does not need to be as uniform. The lower compression needed in this scheme also means that a larger quantity of fuel can be used in a pellet. Therefore the maximum gain achievable is expected to be higher than in the direct/indirect drive approach.

On the other hand the deposition of the secondary laser energy into the fuel pellet is a critical issue for fast ignition. The main approach to delivering the laser energy to the fuel is via the generation and transport of fast electrons [37]. Another approach is to use a laser driven ion beam [38]. In that approach, shown
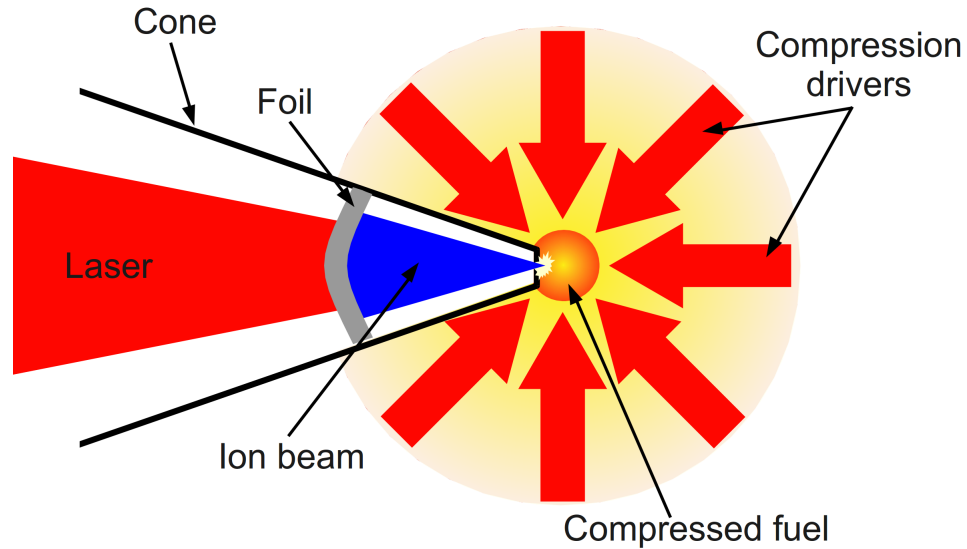
Figure 1.4: Summary of the proton approach to the fast ignition scheme.

schematically in Fig. 1.4, the ignition laser is incident on a thin convex metallic foil encased in the protective gold cone. The beam of protons is generated via the TNSA mechanism and focussed on the tip of the cone by curving the foil appropriately. The characteristic energy deposition of the protons inside a material as presented in Fig. 1.2 (a), compared to the electrons means that it is possible to only heat a small part of the compressed pellet when igniting the fuel, which is required for the maximum gain to be achieved. The use of protons also avoids the issues of fast electron beam transport.

1.2.3   Protons as a probe of field evolution and radiography

Due to their small spatial source size and high degree of laminarity, laser driven ion beams are particularly suited for imaging applications. Ion beams from conventional accelerators are routinely used to probe objects in order to detect density variations and locate defects [39]. This has also been demonstrated with laser driven proton beams by Roth *et al.* [40]. But one of the most exciting applications is the time resolved probing of electric fields.

As demonstrated by Borghesi *et al.* [14] it is possible to use a laser driven proton beam to probe a varying electric field with a high temporal resolution.

This relies on the broad energy spectrum of the proton beam and the fact that the whole proton beam is produced over a very short period of time. The time of flight spreading of the energies also plays a key role. Protons with increasing energy will propagate at increasing velocity, therefore a short time after the beam generation the highest energy part has overtaken the lowest energy part of the beam, and will reach the probed field earlier. If the proton beam is then imaged using a spatial and energy resolving detector such as the one described in chapter 4, it is possible to obtain snapshots of the electric field evolution, as shown in Fig. 1.5 (b). By measuring the deflection of the proton beam it is possible to measure the temporal evolution and the magnitude of the electric field as demonstrated by Romagnani *et al.* [41].
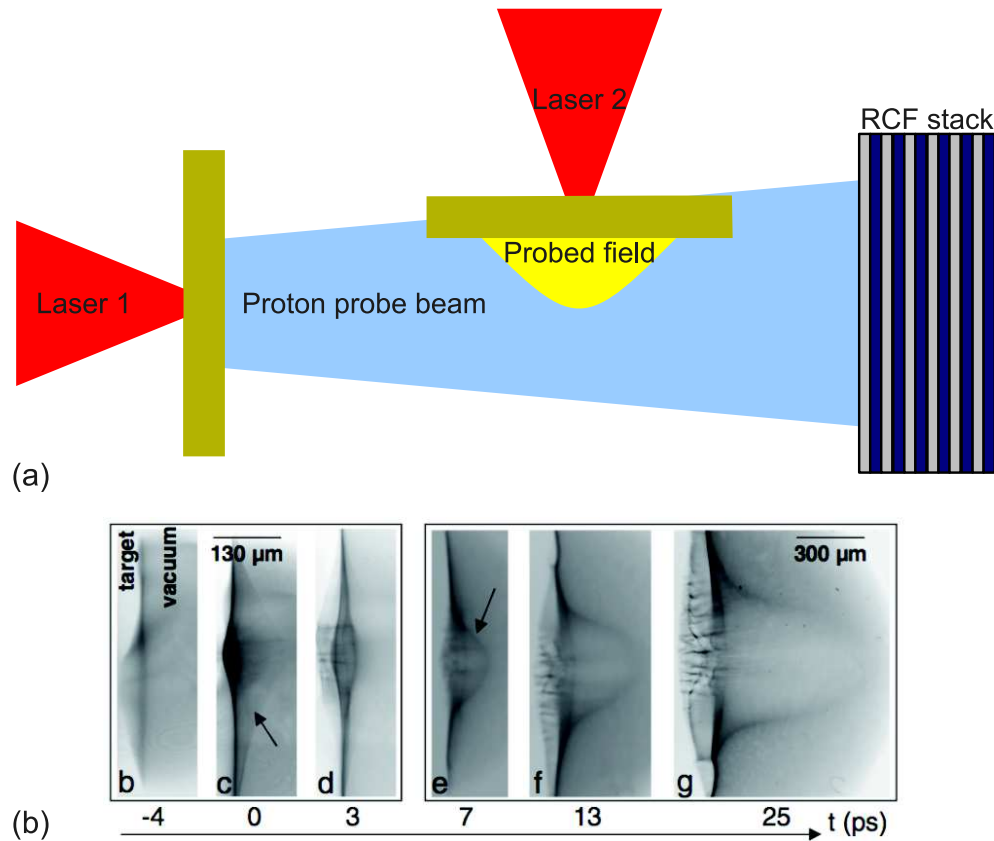
Figure 1.5: (a) A typical experimental set up to perform proton probing of TNSA electric fields. (b) Results of a proton probing experiment conducted by Romagnani *et al.* [41] showing the time evolution of a TNSA electric field driven by a 3×10^{18} Wcm^{-2} laser pulse incident on a 10 μm thick Al foil.

1.2.4   Other applications

Proton heating of matter

Equations of state and opacity of matter can be experimentally investigated by rapidly heating a volume of plasma. This can be achieved by using laser driven proton beams [42] as the proton pulse duration is of the order of the laser pulse, i.e. tens of femtoseconds to a few picoseconds. A target foil is irradiated by the laser pulse, generating protons. The sample to be investigated is placed in the path of the proton beam at a short distance from the foil, and probed.

Neutron production

Neutrons can be generated using laser accelerated ion beams. For examples, a metallic foil with a rear layer of deuterium is irradiated by a relativistic laser pulse. D^+ ions are accelerated via the TNSA mechanism and directed towards a secondary targets containing deuterium. Neutrons are generated by the D-D fusion events occurring in the secondary target [43]. This results in a short duration collimated neutron beam.

Industrial techniques

Laser driven ion sources can also be used in industrial applications such as micro-machining and lithography [44, 45]. The stopping range of ions at a specific energy is an advantage for 3D machining [46], but a drawback for 2D applications.

1.3   Thesis outline

The results from studies carried out while investigating the properties of laser driven ion beams and developing techniques to control the ion beam properties are presented in this thesis. Characterisation of debris emission from ultra-relativistic laser solid interactions is also presented. This work was conducted as part of the Laser Induced Beams of Radiations and their Applications (LIBRA) project involving several institutions throughout the UK.

The thesis is divided in a number of chapters each addressing a different part of the work. **Chapter 2: Fundamentals of laser plasma interaction** presents a physical and mathematical description of the plasma state of matter, the processes responsible for its creation, the physics governing the interaction of a laser pulse with a plasma and the mechanisms responsible for the absorption of the laser energy into the plasma. Next, **Chapter 3: Ion acceleration mechanisms** presents the different mechanisms responsible for the acceleration of laser driven ion beams. This is followed by **Chapter 4: Methods** in which the experimental methods used to perform this work (the laser facilities and diagnostic techniques) are presented. A description of the numerical tools applied to this work is also given in this chapter.

The experimental results are divided in three chapters. In **Chapter 5: Ion acceleration by ultra-high intensity, ultra-high contrast laser irradiation of thin foil targets** the acceleration of ions with laser pulses of intensity equal to 7×10^{20} Wcm^{-2} is presented. The effects of target material, thickness and laser incidence angle on the maximum ion energy are investigated. Then **Chapter 6: Controlling the properties of laser accelerated proton beam using mass limited targets** presents a study on the use of laterally refluxing fast electrons in foil targets of limited transverse dimensions irradiated with laser pulses of 1×10^{19} Wcm^{-2} intensity. The use of different target geometries to control the spatial distribution of the proton beam is also demonstrated. This is followed by **Chapter 7: Characterisation of debris generated by high power laser-solid interactions** in which an investigation of the generation of debris from solid targets irradiated with laser pulses of 1×10^{20} Wcm^{-2} intensity is presented.

Finally, **Chapter 8: Conclusions** summarises the work presented in chapters 5 to 7 of this thesis and gives potential directions for future work.

Chapter 2

Fundamentals of laser plasma interactions

2.1 What is a plasma?

The term plasma is used to described a quasi-neutral physical system constituted of neutral and charged particles in sufficient number to exhibit collective behaviour due to electro-magnetic interactions [47, 48]. In a gas or liquid the constitutive particles (atoms or molecules) only interact with each other via collisions as they are not charged. In the case of the plasma the constituents (ions and electrons) are charged and therefore the Coulomb interaction plays a significant role in their dynamics. The long range of the Coulomb force is responsible for the collective behaviour of the plasma, as any given particle influences the others via the apparition of local electric fields. On a macroscopic scale the plasma can be considered neutral as the number of positive and negative charges are approximately the same, but the neutrality can be broken on a microscopic scale by localised fields. Therefore the plasma is dubbed quasi-neutral.

A number of criteria must be satisfied before the term plasma can be applied:

1. The size of the system must be larger than the distance over which the local electric field can influence the particles (shielding distance).

2. The number of particles within the shielding distance must be sufficient for

the shielding effects to occur

3. The plasma frequency must be greater than the collision rate.

Plasmas were first observed in the late 1800s by Crookes and Thomson [49] while studying glowing discharge in Crookes tubes, but the term plasma was only introduced in 1928 by Langmuir [50]. A wide range of physical systems can be described as plasma, each with very different density and temperatures as shown in Fig. 2.1 [51]. As a consequence, contributions to the understanding of plasma physics comes from a large variety of physics communities. Until the 1950's it was dominated by astrophysicists and geophysicists as well as people studying gas discharges. Therefore most of the plasmas studied experimentally were weakly ionised plasmas containing a large proportion of neutral atoms. It was only with the advent of research on controlled fusion that fully ionised plasmas were studied, in turn drastically expanding the understanding of plasma physics.
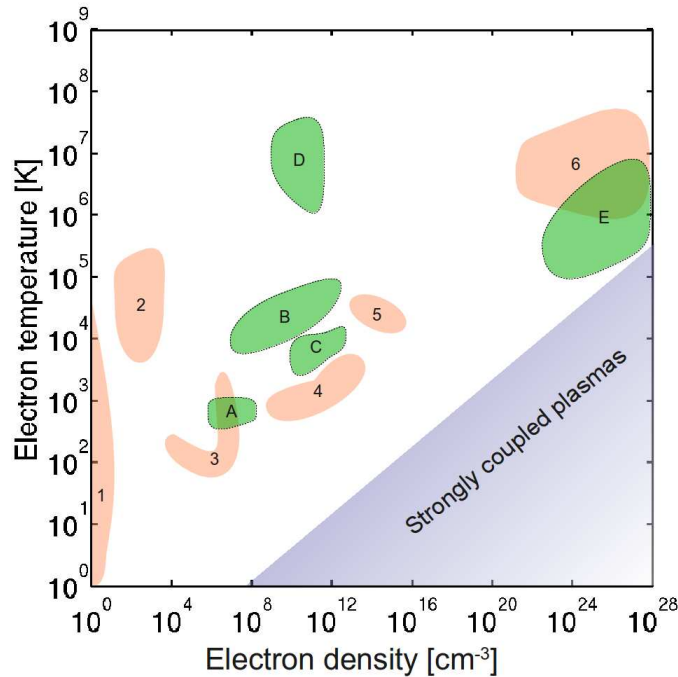
Figure 2.1: Different types of plasma according to their electronic temperature and density. In orange are naturally occurring plasmas while green represents experimental and industrial plasmas. Each plasma type is identified in Table 2.1.

	Natural plasmas
1	Interstellar and interplanetary space
2	Solar wind
3	Ionosphere
4	Stellar atmosphere
5	Lightnings
6	Stellar cores
	Experimental plasmas
A	Flames
B	Flash lamps
C	Industrial plasmas
D	Tokamaks
E	ICF plasmas

Table 2.1: Types of plasmas represented in Fig. 2.1

Today, plasmas are not only a research subject but are also used in many industrial applications such as spacecraft propulsion, ozone generator, waste treatment, welding, signs and TVs. Plasma is often referred to as the 4th state of matter and is by far the most common form of matter in the visible universe.

2.1.1 Coupling factor

Fully ionised plasmas, such as the ones presented in this thesis, can be divided into two types, kinetic plasmas and strongly correlated plasmas. They are usually distinguished by the value of their coupling parameter Ξ, which represents the ratio of the average interaction potential energy per particle, V, and the average kinetic energy per particle, K. The value of the coupling parameter can be obtained using the following formula [51]:

$$\Xi = \frac{V}{K} = \frac{n_e^{4/3} e^2}{6\pi\varepsilon_0 k_B T_e} \simeq 10^{-5} \left(\frac{n_e}{10^{12}[\text{cm}^{-3}]}\right)^{1/3} \frac{10^6[\text{K}]}{T_e} \qquad (2.1)$$

where n_e is the electron density and T_e the electron temperature. In the case of $\Xi > 1$ the plasma is strongly coupled, and if $\Xi < 1$ the plasma is kinetic. The plasmas created by the interaction of a laser pulse with a solid target have a coupling parameter of $\sim 1 \times 10^{-3}$ and are therefore considered kinetic. However the colder and denser bulk of the target has a higher coupling parameter. In this

chapter only kinetic plasmas are discussed.

2.1.2   Plasma frequency

The plasma frequency corresponds to the frequency at which the electrons in the plasma will oscillate if they are displaced from their equilibrium position. It is one of the key parameters in describing the response of a plasma to an electrostatic or electromagnetic perturbation.

Considering a neutral homogeneous one-dimensional plasma, perturbed in such a way that at t>0 the electrons, initially at z_0, are displaced by $\xi(z_0, t)$. The charge separation resulting from the electron displacement will create an electrostatic force that will bring the electrons back to their equilibrium position. By integrating Poisson's equation between $z = -\infty$ and $z = z_0 + \xi$ and by considering that the electrons move as a slab, the electrostatic field generated by the charge separation can be estimated as [48]:

$$E(z, t) = \frac{n_e e}{\varepsilon_0} \xi \tag{2.2}$$

The resulting equation of motion for the electron is then:

$$\frac{d^2\xi}{dt^2} = -\frac{e}{m_e} E \tag{2.3}$$

Eq. (2.3) is the equation of an harmonic oscillator and can be rewritten as:

$$\frac{d^2\xi}{dt^2} = -\omega_p^2 \xi \tag{2.4}$$

where ω_p is the electron plasma frequency with:

$$\omega_p = \sqrt{\frac{n_e e^2}{m_e \varepsilon_0}} \tag{2.5}$$

Similarly an ion plasma frequency, ω_{pi}, can be defined simply by using the ion density n_i and the ion mass m_i in place of n_e and m_e in Eq. (2.5). It is usually neglected due to the much greater mass of the ions compared to the electrons.

2.1.3   Debye length

Another important parameter when characterising a plasma is the shielding distance, or Debye length. This corresponds to the distance that a particle can travel in the time $t = \omega_p^{-1}$. If we consider an electron with a velocity $v_e = \sqrt{\frac{k_B T_e}{m_e}}$ the Debye length λ_D is [48]:

$$\lambda_D = \frac{v_e}{w_p} = \sqrt{\frac{\varepsilon_0 k_B T_e}{n_e e^2}} \tag{2.6}$$

This can be numerically approximated as:

$$\lambda_D[m] \simeq 7.43 \times 10^3 \sqrt{\frac{T_e[eV]}{n_e[m^{-3}]}} \tag{2.7}$$

For T_e=1 MeV and n_e=10^{27} m^{-3} we have $\lambda_D \simeq$0.23 μm.

For most plasmas the velocity of the ions is negligible compared to the electrons and only the latter are considered in the calculation of the Debye length. But in the case of fast moving ions, as at the rear surface of a laser irradiated target, the contribution of the ions to the Debye length must be considered and Eq.(2.6) becomes:

$$\lambda_D = \sqrt{\frac{\varepsilon_0 k_B}{e^2 \left(\frac{n_e}{T_e} + \sum_{iq} q^2 \frac{n_{iq}}{T_i} \right)}} \tag{2.8}$$

where n_{iq} is the density of the ion species i with a charge qe.

For the shielding effect to occur the number of particles in the charge cloud N_D must be sufficient. This can be quantitatively estimated by using Eq.(2.9) [47]:

$$N_D = \frac{4}{3} n_e \pi \lambda_D^3 \tag{2.9}$$

2.2   Describing the plasma

The evolution of a physical system containing N charged particles can be fully described by solving the equation of motion of each particle in given $\vec{B}(\vec{r_i}, t)$ and

$\vec{E}(\vec{r_i}, t)$ fields [48]:

$$\vec{a_i} = \frac{d\vec{v_i}}{dt} = \frac{q}{m_i}\left[\vec{E}(\vec{r_i}, t) + \vec{v_i} \times \vec{B}(\vec{r_i}, t)\right] \tag{2.10}$$

where $\vec{r_i}$ and $\vec{v_i}$ represent the position and velocity of the particles (i=1, N) and $\vec{E}(\vec{r_i}, t)$ and $\vec{B}(\vec{r_i}, t)$ are obtained by solving Maxwell's equations.

This approach is suitable for microscopic systems where N is small. In the case of a plasma the system is often macroscopic and the number of particle is too large for each of them to be tracked individually and therefore distribution functions have to be used instead. Distribution functions, written $f(\vec{r}, \vec{v}, t)$, are widely used in statistical physics to describe the statistical average number of particles in a given volume of the phase space.

2.2.1 Maxwell's equations

As stated previously the electric and magnetic fields present in a plasma can be fully described by solving Maxwell's equations [52]:

$$\nabla \cdot \vec{B} = 0 \qquad\qquad \text{(Gauss' law)} \tag{2.11}$$

$$\nabla \times \vec{E} = -\frac{\partial \vec{B}}{\partial t} \qquad\qquad \text{(Faraday's law)} \tag{2.12}$$

$$\nabla \cdot \vec{E} = \frac{\rho}{\varepsilon_0} \qquad\qquad \text{(Poisson's equation)} \tag{2.13}$$

$$\nabla \times \vec{B} = \mu_0 \left(\vec{j} + \varepsilon_0 \frac{\partial \vec{E}}{\partial t}\right) \qquad\qquad \text{(Ampère's law)} \tag{2.14}$$

where ρ and $\vec{j}$ are the charge and current density respectively. If distribution functions are used they are defined as:

$$\rho = q \int f(\vec{v}) \, d\vec{v} \tag{2.15}$$

$$\vec{j} = q \int \vec{v} f(\vec{v}) \, d\vec{v} \tag{2.16}$$

2.2.2   The kinetic model

A kinetic approach can be used to describe in detail the temporal and spatial evolution of the distribution function for a given particle type. If we consider a given volume V in the phase space described by the six dimensions $\vec{V}$ vector (3 velocity dimensions $\vec{v}$ and 3 acceleration dimensions $\vec{a}$), then the equation of continuity of the distribution function in the phase space can be written as [48]:

$$\frac{\partial f}{\partial t} + \nabla \cdot \left(f\vec{V} \right) = 0 \tag{2.17}$$

The 3 spatial dimensions and the 3 velocity dimensions can be explicitly written and Eq. (2.17) becomes:

$$\frac{\partial f}{\partial t} + \frac{\partial}{\partial \vec{r}} \cdot (\vec{v}f) + \frac{\partial}{\partial \vec{v}} \cdot (\vec{a}f) = 0 \tag{2.18}$$

Because $\partial \vec{a}/\partial \vec{v} = 0$ Eq. (2.18) is equivalent to:

$$\frac{\partial f}{\partial t} + \vec{v}\frac{\partial f}{\partial \vec{r}} + \vec{a}\frac{\partial f}{\partial \vec{v}} = 0 \tag{2.19}$$

Eq. (2.19) is known as the Vlasov equation. Coupled together Eq. (2.11 - 2.14) and Eq. (2.19) form a closed system of equations that can be used to describe a plasma. However this system does not consider collisions between the particles, ionisation or recombination. The collisions between the different species constituting the plasma can be accounted for if Eq. (2.19) is replaced by the Vlasov-Fokker-Planck equation:

$$\frac{\partial f}{\partial t} + \vec{v}\frac{\partial f}{\partial \vec{r}} + \vec{a}\frac{\partial f}{\partial \vec{v}} = C_{ei}(f) + C_{ee}(f) \tag{2.20}$$

where C_{ei} and C_{ee} are the electron-ion and electron-electron collision operators respectively.

2.2.3   The hydrodynamic model

Another approach to describe a plasma is to consider each constitutive species as a fluid of charge. This hydrodynamic approach leads to simpler equations than

the kinetic approach but remains sufficiently accurate to describe most of the plasma phenomena.

This approach hinges on a number of equations, the first of which is the fluid continuity equation:

$$\frac{\partial n}{\partial t} + \nabla \cdot (n\vec{v}) = 0 \tag{2.21}$$

where n is the density of the fluid and $\vec{v}$ its velocity. The second equation required is the fluid force equation:

$$\frac{\partial \vec{v}}{\partial t} + (\vec{v} \cdot \nabla)\,\vec{v} = \frac{q}{m_i}\left(\vec{E} + \vec{v} \times \vec{B}\right) - \frac{1}{nm_i}\nabla \cdot \vec{P} + \Phi_{coll} \tag{2.22}$$

where $\vec{P}$ is the pressure tensor in the fluid and Φ_{coll} is a function describing the collisions in the fluid.

Each physical variables needed to solve Eq. (2.21 & 2.22) corresponds to an integration over the velocity of product of the distribution function and an appropriate function of the velocity. The density of the particles in space and time is described by:

$$n = \int f(\vec{r}, \vec{v}, t)\,d\vec{v} \tag{2.23}$$

The average velocity $\vec{v_i}$ is defined as:

$$n\vec{v}(\vec{r}, t) = \int \vec{v} f(\vec{r}, \vec{v}, t)\,d\vec{v} \tag{2.24}$$

The pressure tensor $\vec{P}$ is defined by:

$$\vec{P}(\vec{r}, t) = m_i \int \vec{v}^{\,2} f(\vec{r}, \vec{v}, t)\,d\vec{v} \tag{2.25}$$

In the case of a system in thermodynamic equilibrium at the temperature T, the distribution function f is given by a Maxwellian distribution:

$$f(\vec{v}) = n\left(\frac{m_i}{2\pi k_B T}\right)^{3/2} \exp\left(-\frac{m_i \vec{v}^{\,2}}{2k_B T}\right) \tag{2.26}$$

In this situation Eq. (2.25) gives $P_i = n_i k_B T$ which is the pressure in a perfect

gas as expected.

2.2.4 Collisions in a plasma

In a fully ionised plasma all collisions are Coulomb collisions. Two types of collisions can occur:

- Collisions between like particles (electron-electron and ion-ion)

- Collisions between unlike particles (electron-ion and ion-electron)

In the case of like particles colliding, the most extreme case is a 90° change in the velocity direction of each particles. In such a collision the centre of mass of the two colliding particles remains stationary and therefore the collision generates very little diffusion. However, this is very different in the case of unlike particles colliding. In such collisions the velocity of the particles will be reversed and the centre of mass of the two particles will be displaced generating a lot of diffusion [47]. As a direct consequence of the differences between the two types of collisions, only the collisions between unlike particles are usually considered when describing the plasma.

The momentum variation in the case of an electron-ion collision is defined as [47]:

$$\vec{P}_{ei} = m_e n_e \left(\vec{v}_i - \vec{v}_e \right) \nu_{ei} \tag{2.27}$$

where $\vec{v}_i$ and $\vec{v}_e$ are the ion and electron velocity respectively and ν_{ei} is the collision frequency defined further. It should be noted that due to momentum conservation electron-ion and ion-electron collisions are similar and $\vec{P}_{ei} = -\vec{P}_{ie}$. The Coulomb force applied on the electron by the ion is defined as:

$$F_C = -\frac{qe^2}{4\pi\varepsilon_0 r^2} \tag{2.28}$$

where r is the distance between the two particles. In the absence of Coulomb force the closest possible distance between the two particles is called the impact parameter p given by:

$$p = \frac{qe^2}{4\pi\varepsilon_0 m_e v_e^2} \frac{1}{tan(\theta/2)} \tag{2.29}$$

where θ is the scattering angle. The force F_C applied on the electron is felt for the time when the electron is in the vicinity of the ion, $t \simeq p/v_e$, therefore the momentum variation is:

$$\vec{P}_{ei} \simeq \frac{qe^2}{4\pi\varepsilon_0 p_0 v_e} \tag{2.30}$$

In the case of a 90° interaction the impact factor becomes:

$$p_0 = \frac{qe^2}{4\pi\varepsilon_0 m_e v_e^2} \tag{2.31}$$

and the Coulomb cross section of the collision can be defined as:

$$\sigma_{ei} = \pi p_0^2 = \frac{qe^2}{16\pi\varepsilon_0^2 m_e^2 v_e^4} \tag{2.32}$$

The collision frequency ν_{ei} can then be defined as:

$$\nu_{ei} = n_e \sigma_{ei} v_e = \frac{n_e q^2 e^4}{16\pi\varepsilon^2 m_e^2 v_e^3} \tag{2.33}$$

Because the interaction between the two colliding particles is defined by the Coulomb force, the momentum variation $\vec{P}_{ei}$ is proportional to the density and charge of the particles involved. Therefore:

$$\vec{P}_{ei} = \eta q e^2 n_e^2 \left(\vec{v}_i - \vec{v}_e \right) \nu_{ei} \tag{2.34}$$

where η is the resistivity of the plasma which can be defined as a function of the collision frequency:

$$\eta = \frac{m_e}{n_e e^2}\nu_{ei} = \frac{qe^2}{16\pi\varepsilon_0^2 m_e v_e^3} \tag{2.35}$$

In the case of a Maxwellian distribution of the velocities an order of magnitude of the resistivity is given by:

$$\eta \simeq \frac{q\pi e^2 \sqrt{m_e}}{16\pi^2\varepsilon_0^2(k_B T_e)^{3/2}} \tag{2.36}$$

So far only the large angle collisions have been considered in the estimation of the resistivity. Because the Coulomb force has a long range, small angle deflections

are very frequent and their cumulative effect cannot be neglected. Spitzer *et al.* [53] have demonstrated that the small angle deflections can be accounted for by multiplying Eq. (2.36) by the Coulomb logarithm, $\ln \Lambda$.

$$\eta_{Spitzer} \simeq \frac{q\pi e^2 \sqrt{m_e}}{16\pi^2 \varepsilon_0^2 (k_B T_e)^{3/2}} \ln \Lambda \tag{2.37}$$

Λ is defined as the ratio of the minimum and maximum impact factor, $\Lambda = p_{max}/p_{min}$. Usually $p_{max} = \lambda_D$ and $p_{min} = p_0$ are chosen, which gives $\Lambda = 4\pi n_e \lambda_D^3$. For T_e=100 eV and n_e=10^{27} m^{-3}, $\ln \Lambda \simeq 5$.

2.3 Creating the plasma

In the work presented in this thesis, plasmas are created by the interaction of highly energetic laser pulses with solid targets. For the transition from the solid state to the plasma state to occur, the laser must ionise the target by depositing enough energy to overcome the binding energy of the electrons with the atoms. To reach a high level of ionisation, electrons must be stripped from the outer most to the inner most orbitals, each with an increasing ionisation potential.

A hydrogen atom in its ground state requires an energy of 13.6 eV to be ionised, this corresponds to a binding electric field E_a=5×10^{11} Vm^{-1}. In order to overcome the ionisation potential the laser field must be greater than E_a, corresponding to an intensity $I_L \geq 10^{16}$ Wcm^{-2}. However, when the laser field is applied to the atom, a number of physical processes can occur enabling ionisation with field smaller than E_a. These effects include multi-photon ionisation, collisional ionisation, tunnel ionisation and barrier suppression, and are represented in Fig. 2.2.

2.3.1   Ionisation mechanisms

To determine which of the ionisation processes is more likely, Keldysh [54] introduced a dimensionless parameter, K:

$$K = \omega_L \sqrt{\frac{2U_k}{I_L}} \qquad (2.38)$$

where U_k is the ionisation potential of the atom considered and ω_L is the frequency of the laser pulse. For moderate laser intensity, $K>1$ and multiphoton ionisation is the dominant process, while for high laser intensity, $K<1$ and tunnel and barrier suppression ionisation are the dominant mechanisms.

Multi-photon ionisation

The simplest way to ionise an atom is to irradiate it with a single photon with an energy higher than the ionisation potential. This constraint on the energy can be relaxed if a large number of photons with total energy greater than the ionisation potential are absorbed in a very short time. This process is referred to as multi-photon ionisation and is shown schematically in Fig. 2.2 (a).

Collisional ionisation

Once atoms are ionised, even partially, the plasma contains a certain density n_e of free electrons. If their kinetic energy is sufficient, i.e. greater than the electron binding energy, these free electrons can ionise atoms by colliding with them. This process is termed collisional ionisation, and the rate of such collisions ν_C can be calculated [55]:

$$\nu_C \simeq n_e v_e 4\pi a_b^2 \left(\frac{U_H^2}{U_k k_B T_e} \right) \ln \left(\frac{k_B T_e}{U_k} \right) \qquad (2.39)$$

where U_H is the ionisation potential of a ground state hydrogen atom, and a_b is the Bohr radius. This process is presented in Fig. 2.2 (b).

Tunnel and barrier suppression ionisation

As shown in Fig. 2.2 (c-d) the presence of an external field, in this case the laser field, can modify the binding potential of the ion. Barrier suppression occurs if the laser field is strong enough to suppress the Coulomb barrier enabling the electron to escape the binding field. This occurs if the intensity of the laser reaches a threshold intensity defined as:

$$I_{BSI} = \frac{U_k^4 c \pi^2 \varepsilon_0^3}{2 q^2 e^6} = \frac{4 \times 10^9}{q^2} \frac{U_k^4}{[\text{eV}]} [\text{Wcm}^{-2}] \tag{2.40}$$

In the case of a ground state hydrogen atom $I_{BSI} = 10^{14}$ Wcm^{-2}. If the laser intensity is below the barrier suppression threshold ionisation can still occur via tunnelling, as the Coulomb barrier may be low enough for the tunnelling probability to be non negligible.

The rate of these ionisation processes can be estimated using the ADK ionisation rate formula [56]:

$$\nu_{ADK} \approx 6.6 \times 10^{16} \frac{q^2}{n_{ef}^{4.5}} \exp \left\{ -\frac{2q^3}{3n_{ef}^3} \left[\frac{E_a}{E(t)} \right]^{1/2} \right\} \left\{ 10.87 \frac{q^3}{n_{ef}^4} \left[\frac{E_a}{E(t)} \right]^{1/2} \right\}^{(2n_{ef} - 1.5)} \tag{2.41}$$

where $E_a = e/4\pi\varepsilon_0 a_B^2$ is the strength of the electric field that keeps the electron on its orbit and $n_{ef} = q/\sqrt{U_k/U_H}$ with U_H the ionisation potential of a ground state hydrogen atom.

2.4   Interaction of a laser with the front surface plasma

As described previously, the laser irradiated surface of the target is ionised in the early stage of the laser-target interaction. This results in the generation of a front surface plasma with which the laser interacts over the duration of its pulse.

The front surface plasma expands into the vacuum at a velocity close to the
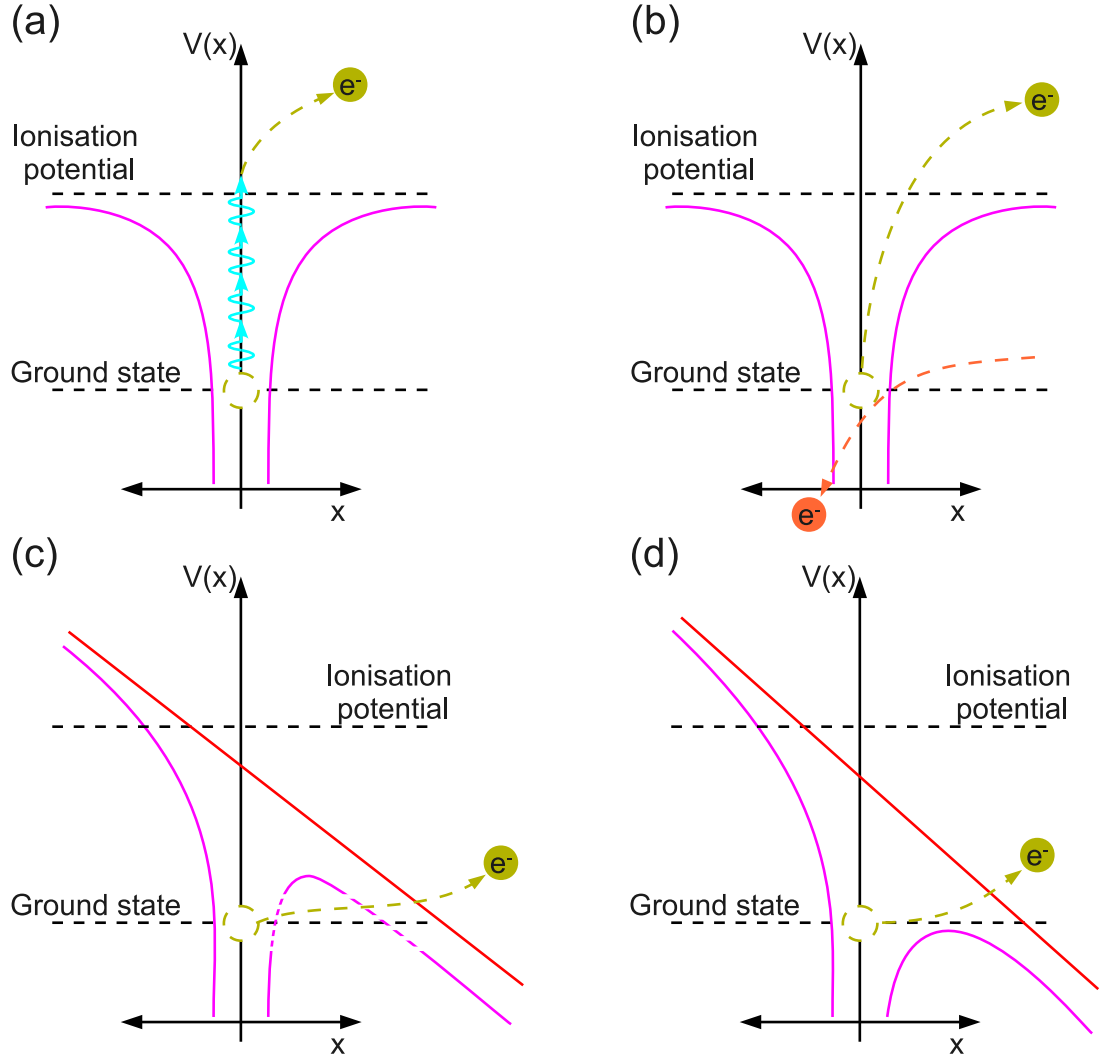
Figure 2.2: Illustration of the different ionisation processes responsible for the creation of the plasma as described in the main text. (a) Multiphoton ionisation. (b) Collisional ionisation. (c) Tunnel ionisation. (d) Barrier suppression ionisation. The solid red line represents the laser field while the solid magenta lines represent the binding field.

ion sound speed:

$$c_s = \sqrt{\frac{q k_B T_e}{m_i}} \tag{2.42}$$

In the case of a one-dimensional isothermal expansion, the density of the plasma falls off exponentially from the initial density n_0 as shown in Fig. 2.3:

$$n_e(z) = n_0 \exp\left(-\frac{z}{L_s}\right) \tag{2.43}$$

where L_s is the density scale length and z is the distance from the target surface.

L_s corresponds to the distance at which $n_e(L_s) = n_0/e_N$ and characterises the scale length of the front surface plasma ($e_N \simeq 2.719$).

L_s can be estimated using the ion sound speed and the laser pulse duration (τ_L) as $L_s \simeq c_s\tau_L$. In the case of a low intensity ($\sim10^{12}$ Wcm^{-2}) laser pulse with a duration of 3 ns, $L_s \simeq 200$ μm. Such a large scale length plasma can be generated by the laser pedestal, and in this case the propagation of the main laser pulse occurs in a plasma. The amount of front surface plasma can be drastically reduced if the intensity of the laser pedestal is lowered using the techniques described in chapter 4.
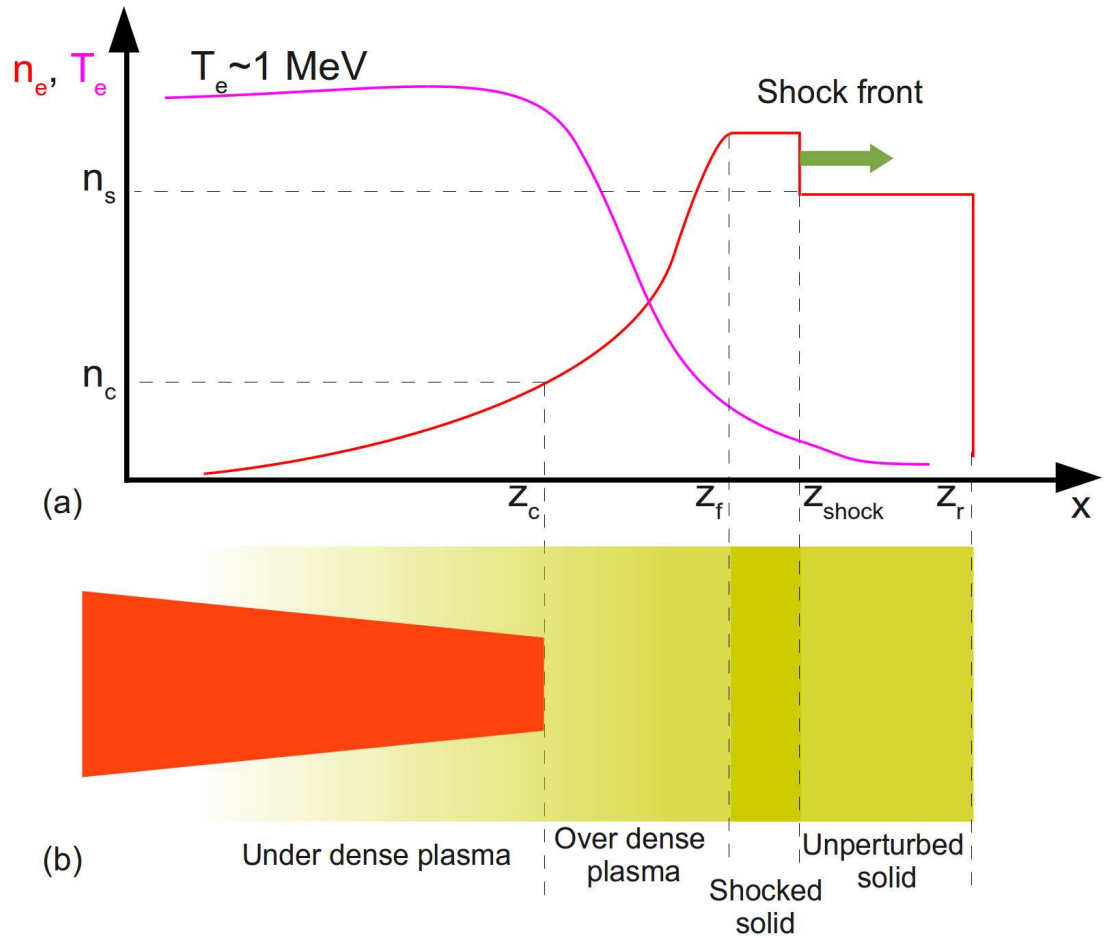
Figure 2.3: (a) Schematic of the density and temperature profiles during laser interaction with a solid target. (b) Different regions of the interaction. z_f and z_r mark the position of the front and rear surface of the target respectively. z_c represents the position of the critical density and z_{shock} the position of the shock front launched by the laser. n_c is the critical density, as described in the main text, and n_s is the solid density.

2.4.1   Propagation of the laser pulse in a plasma

The equation of propagation of an electromagnetic wave is obtained by combining the curl of Faraday's law (Eq. (2.12)) with Ampère's law (Eq. (2.14)) and gives [48]:

$$\nabla \times \nabla \times \vec{E_L} + \frac{1}{c^2}\frac{\partial^2 \vec{E_L}}{\partial t^2} = -\mu_0 \frac{\partial \vec{j}}{\partial t} \tag{2.44}$$

where $\vec{E_L}$ is the laser electric field and $\vec{j}$ is the electric current density in the plasma. Considering a stationary plasma with an electromagnetic field $\vec{E_L}$ oscillating at the laser frequency ω_L:

$$\vec{E_L}(\vec{r}, t) = \Re\left[\vec{E_L}(\vec{r})\exp(-i\omega_L t)\right] \tag{2.45}$$

$$\vec{j}(\vec{r}, t) = \Re\left[\vec{j}(\vec{r})\exp(-i\omega_L t)\right] \tag{2.46}$$

In a cold non magnetised plasma $\vec{E_L}(\vec{r})$ and $\vec{j}(\vec{r})$ are linked by the following relation:

$$\vec{j} = -i\omega_L \varepsilon_0 \psi(\omega_L)\vec{E} \tag{2.47}$$

where $\psi(\omega_L)$ is the electric susceptibility. Eq. (2.44) can be rewritten as:

$$\Delta \vec{E_L} - \nabla\left(\nabla \cdot \vec{E_L}\right) + \frac{\omega_L^2}{c^2}\varepsilon_0(\omega)\vec{E_L} = 0 \tag{2.48}$$

with $\varepsilon_0(\omega_L)$ defined as:

$$\varepsilon_0(\omega_L) = 1 + \psi(\omega_L) \tag{2.49}$$

In the case of a cold non-collisional plasma Eq. (2.49) becomes:

$$\varepsilon_0(\omega_L) \simeq 1 - \frac{\omega_p^2}{\omega_L^2} \tag{2.50}$$

Critical density

Considering the case of an electromagnetic wave such that $\nabla \cdot \vec{E_L} = 0$, Eq. (2.48) becomes:

$$\Delta \vec{E_L} + \frac{\omega_L^2}{c^2}\varepsilon_0(\omega_L)\vec{E_L} = 0 \tag{2.51}$$

In the case of an homogeneous plasma the solutions are of the form $\vec{E}_L(\vec{r}) = \vec{E}_L \exp(i\vec{k} \cdot \vec{r})$ and Eq. (2.51) gives the dispersion relation of an electromagnetic wave in a plasma:

$$k = \frac{\omega_L}{c} \sqrt{\varepsilon_0(\omega_L)} \tag{2.52}$$

which becomes, using Eq. (2.50):

$$\omega_L^2 = \omega_p^2 + k^2 c^2 \tag{2.53}$$

For an electromagnetic wave to propagate inside the plasma, the wave number k must be real, this is the case only if $\varepsilon(\omega_L) > 0$, which implies $n_e < n_c$ where n_c is the critical density defined as [57]:

$$n_c = \frac{m_e \varepsilon_0 \omega_L^2}{e^2} \tag{2.54}$$

If $n_e > n_c$ the laser is fully reflected. For a laser pulse with a 1 μm wavelength, $n_c \simeq 10^{27}$ m^{-3}.

As shown in Fig. 2.3, the density of the preformed plasma increases as the laser gets closer to the target front surface. The position where it becomes equal to the critical density is referred to as the critical surface. This surface defines two regions of the front surface plasma:

1 the underdense region, where $n_e < n_c$ and;

2 the overdense region, where $n_e > n_c$.

At relativistic laser intensities n_c increases by a factor γ due to the relativistic increase of the electron mass. This increase in the critical density enables the laser to propagate further inside the plasma. This processed is termed laser-induced transparency.

Skin depth

An evanescent electric field defined as:

$$E_L(z) = E_L(z_c) \exp\left(-\frac{z}{l_s}\right) \tag{2.55}$$

where z_c is the position of the critical surface, and l_s is the characteristic distance, called the skin depth, can be generated beyond the critical surface by the laser field. In the collisionless case l_s is defined as [57]:

$$l_s = \frac{c}{\sqrt{\omega_p^2 - \omega_L^2}} \tag{2.56}$$

In the case of the highly overdense limit $(n_e \gg n_c)$ $l_s \simeq c/\omega_p$ [58]

Laser self-focussing

The refractive index n_r of a plasma is a function of the plasma frequency ω_p and the laser frequency ω:

$$n_r = \sqrt{1 - \left(\frac{\omega_p}{\omega_L}\right)^2} \tag{2.57}$$

It can also be expressed as a function of the plasma density n_e and the critical density n_c:

$$n_r = \sqrt{1 - \frac{n_e}{n_c}} \tag{2.58}$$

As illustrated in Fig. 2.4, when the focussed laser propagates into the plasma, the ponderomotive force of the laser expels the electrons from the beam path. As will be described in Section 2.4.3, the ponderomotive force is greater in the region of high laser intensity, and pushes the electrons radially (with respect to the laser propagation axis) towards the regions of lower laser intensity. This results in a radial density gradient in the plasma, with the highest density in the region of lowest laser intensity. This creates a refractive index profile with a maximum on the laser axis, which acts as a focussing lens, therefore leading to self focussing of the laser [59]. The intensity of the laser is consequently increased [60, 61] leading to more self focusing.
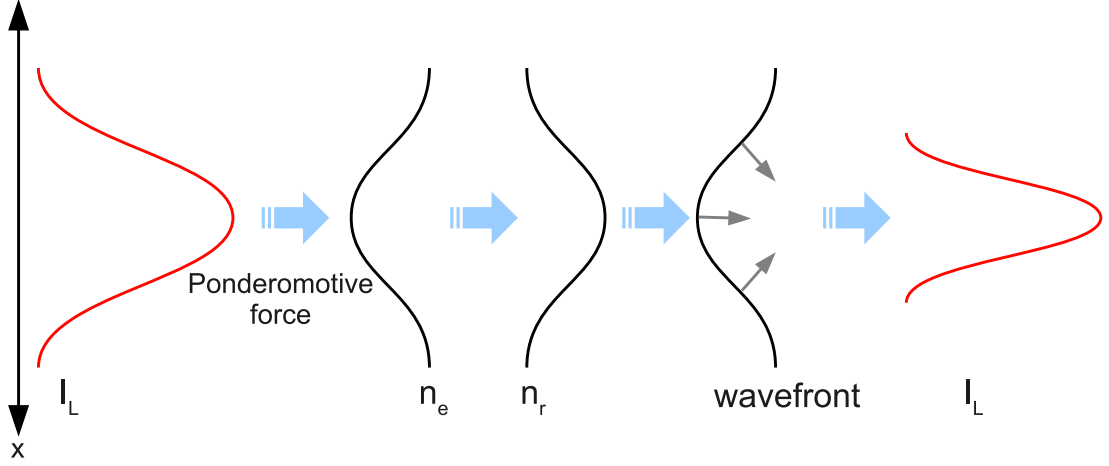
Figure 2.4: The self focussing of a laser pulse in an underdense plasma.

2.4.2   A free electron in a laser field

As the laser pulse propagates through the front surface plasma, the free electron motion is governed by the laser field and can be described using the Lorentz equation (see Eq. (2.10)). Due to their much larger mass, the ions in the plasma are considered stationary, and only the motion of the electrons is considered. The force felt by the electrons can be split in two components:

- a transverse one (with respect to the laser propagation direction) due to the electric field of the laser, $F_\perp$ and

- a parallel one due to the magnetic field of the laser, $F_\parallel$.

The components of the force can be described as:

$$F_\perp = eE_{L0}\cos(\omega_L t) \tag{2.59}$$

and

$$F_\parallel = ev_\perp B_{L0} = e\,\frac{v_\perp}{c}\frac{E_{L0}}{2}\sin(\omega_L t) \tag{2.60}$$

where E_{L0} and B_{L0} are the amplitude of the electric and magnetic laser fields respectively, and $v_\perp$ is the quiver velocity of the electrons oscillating in the laser electric field of frequency ω_L:

$$v_\perp = \frac{eE_{L0}}{m_e\omega_L} \tag{2.61}$$

32

It is clear from Eq. (2.60) that for the $\vec{v} \times \vec{B}$ component of the Lorentz force to be taken into account $v_\perp$ must be close to c, which corresponds to the relativistic regime. This regime can be attained if $E_{L0} > 3.2 \times 10^{12}$ Vm^{-1} corresponding to a laser intensity $I_L > 1.37 \times 10^{18}$ Wcm^{-2}. Traditionally, to indicate if the laser intensity is in the relativistic regime, the dimensionless light amplitude a_0 is used. It is defined as the ratio of the classical electron momentum to the relativistic electron momentum:

$$a_0 = \frac{eE_{L0}}{m_e c \omega_L} = \sqrt{\frac{I_L \lambda_L^2}{1.37 \times 10^{18}}} \tag{2.62}$$

where I_L is in Wcm^{-2} and λ_L in microns. $a_0 \ll 1$ corresponds to the non-relativistic regime while $a_0 \sim 1$ corresponds to the relativistic regime.

2.4.3 Ponderomotive force

In the case of a spatially homogeneous laser field intensity, the electrons do not gain net energy. Once the laser pulse has passed, the electrons return to their equilibrium position. However, in reality, the spatial profile of a tightly focussed beam is not homogeneous, it is typically Gaussian. The spatial variations in the intensity create strong gradients in the oscillating field resulting in a force that gradually pushes the electrons away from the regions of highest intensity. This is illustrated in Fig. 2.5.

Considering an electron positioned on the laser axis where the laser field is the strongest. During one half of the laser field oscillation it experiences a strong transverse force pulling it away from the laser axis. During the second half of the oscillation, the electron experiences a transverse force directed towards the laser axis. But the electron is now located in a region where the laser field is lower than at the laser axis, therefore it does not return to the laser axis at the end of the laser cycle. When averaged over many oscillations this results in a net force that pushes the electron towards regions of lower laser intensity. This force is called the ponderomotive force.

The ponderomotive force felt by an electron in the non relativistic case is
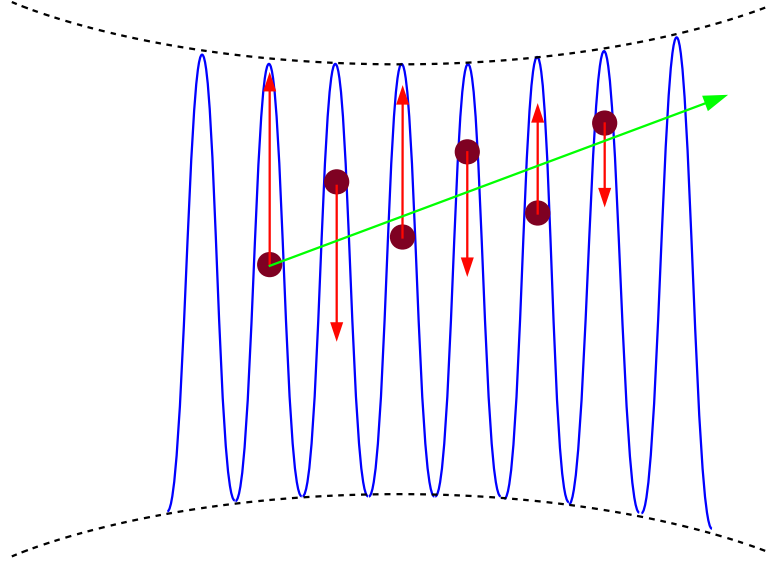
Figure 2.5: Position of a sample electron in the laser electric field (in blue) at different times. The red arrows symbolise the electric field applied on the electron, the green arrow corresponds to the time integrated motion of the electron and dashed lines represents the laser beam profile.

defined as [57]:

$$F_P = -\frac{e^2}{4m_e\omega_L^2}\nabla E_{L0}^2 = -\frac{e^2}{8\pi^2\varepsilon_0 m_e c^3}\nabla(I_L\lambda_L^2) \tag{2.63}$$

In the relativistic case, the time averaged kinetic energy gained by the electron during one laser cycle is equivalent to the ponderomotive potential U_P is defined as [62]:

$$U_P = m_e c^2(<\gamma>-1) \tag{2.64}$$

For a linearly polarised laser pulse $<\gamma_L>=\sqrt{1+a_0^2/2}$ and for a circularly laser pulse $<\gamma_C>=\sqrt{1+a_0^2}$ [62]. Therefore in linear polarisation:

$$U_{PL} = m_e c^2(\sqrt{1+\frac{a_0^2}{2}}-1) \tag{2.65}$$

and in circular polarisation:

$$U_{PC} = m_e c^2(\sqrt{1+a_0^2}-1) \tag{2.66}$$

2.5 Absorption of the laser energy in the plasma

As the laser pulse propagates through the under-dense plasma part of its energy is absorbed by the plasma. This energy transfer from the laser to the electrons, and subsequently to the ions, is governed by several different mechanisms presented below.

2.5.1 Vacuum heating

This mechanism is one of the main absorption mechanisms at relativistic laser intensities. It becomes dominant when the laser is incident at an angle onto a short density scale length plasma.

Consider an electron in the under-dense region of the front surface plasma oscillating in the laser electric field. In this situation the electron gains no net kinetic energy. However, if the electron is driven past the critical density surface by the electric field, it will not be affected by the laser any more as the laser field cannot propagate beyond the skin layer. Therefore the electron is accelerated into the target with a fraction of the laser energy. At a laser incident angle θ_L the fraction of energy transferred to the electrons is estimated as [62]:

$$f_{VH} = \frac{\eta_{osc}}{2\pi} \frac{v_n^3}{cv_\perp^2 \cos\theta_L} \qquad (2.67)$$

where v_n is the quiver velocity of the electron due to the laser electric field component normal to the target surface $E_N = 2E_{L0}\sin\theta_L$. η_{osc} is a dimensionless factor representing the loss of electron oscillatory motion to the plasma [63, 64]:

$$\eta_{osc} = \frac{1}{\left(1 - \frac{\omega_L^2}{\omega_p^2}\right)} \qquad (2.68)$$

At a constant incidence angle this mechanism is most effective if the laser is p-polarised as was demonstrated by Ceccotti *et al.* [65].

2.5.2   Resonance absorption

Resonance absorption is the dominant absorption mechanism at laser irradiances in the range 10^{14} Wcm^{-2} μm$^2 < I_L\lambda_L^2 < 10^{17}$ Wcm^{-2} μm^2. For higher intensities however, resonance absorption is still present but it no longer dominates the absorption process. It is shown schematically in Fig. 2.6.
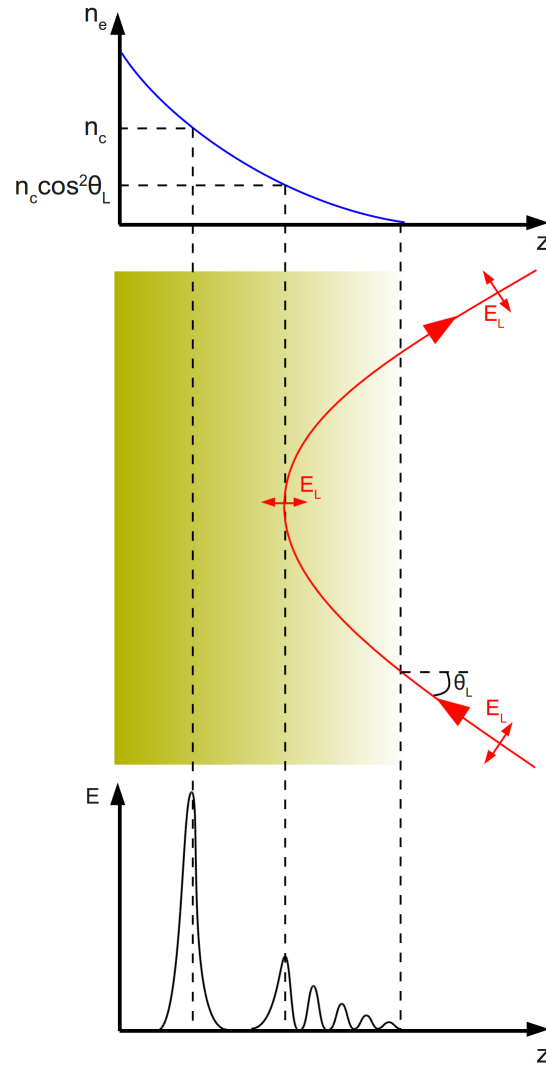
Figure 2.6: Resonance absorption of a laser pulse. As the laser reaches the density $n_c\cos^2(\theta_L)$ it resonantly excites a plasma wave in the over-dense plasma.

Resonance absorption occurs when the laser is p-polarised and incident at an angle (θ_L) through a plasma density gradient. In this situation the laser electric field can only propagate up to a plasma density equal to $n_c\cos^2(\theta_L)$ but the component of the field normal to the target can tunnel through to the critical

surface and resonantly excite an electron plasma wave at the laser frequency. The resulting plasma wave can then transfer its energy to the plasma via wave breaking or damping effects. The fraction of energy that is transfered from the laser pulse to the plasma via the resonance absorption mechanism is defined as [62]:

$$f_{RA} \approx \frac{1}{2} \left[2.3 \, Q \exp \left(-\frac{2 \, Q^3}{3} \right) \right] \tag{2.69}$$

with:

$$Q = \left(\frac{\omega_L L_s}{c} \right)^{1/3} \sin \theta_L \tag{2.70}$$

It is clear from Eq. (2.69 & 2.70) that f_{RA} strongly depends on the laser incidence angle θ_L for a given L_s. As shown in Fig. 2.7, f_{RA} is equal to zero for normally incident laser pulses and has a maximum at a given angle depending on L_s.
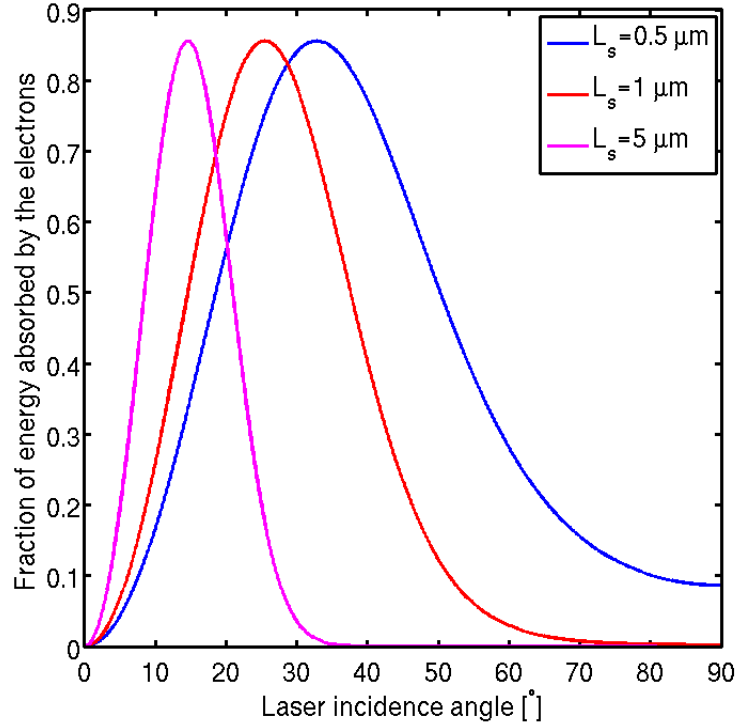
Figure 2.7: Variation of f_{RA} as a function of the laser incidence angle for different pre-plasma scale length, 0.5 μm (blue), 1 μm (red) and 5 μm (magenta).

2.5.3   Inverse bremsstrahlung

When an electron is de-accelerated by a collision with another charged particle it emits a characteristic radiation called bremsstrahlung radiation. The opposite phenomenon can also occur, in which the electron is accelerated by the laser electric field, and this is simply called inverse bremsstrahlung. Normally, this would not result in a net gain of energy by the electron, as it will experience an equal and opposite acceleration during the following laser half cycle. However, if the electron collides with an ion during its oscillation it will transfer a fraction of its energy to the ion, thereby transferring laser energy to the plasma.

For a laser of intensity $< 10^{14}$ Wcm^{-2} propagating into a plasma with a linear density profile and a Maxwellian energy distribution, the fraction of laser energy transferred to the plasma is given by [62]:

$$f_{IB} = 1 - \exp\left(-\frac{32}{15}\frac{\nu_{ei}(n_c)}{c}L_s\right) \tag{2.71}$$

with $\nu_{ei}(n_c)$ the electron-ion collision frequency at the critical density.

At higher laser intensity the electron population can no longer be considered Maxwellian, but is instead determined by the oscillatory motion of the electron in the laser field. The resulting inverse bremsstrahlung absorption will be lower than predicted by Eq. (2.71). Wilks and Kruer [62] introduced a correction factor:

$$C_{WK} = \left[1 + 1.5\left(\frac{eE_{L0}}{\omega_L m_e c}\right)^2\right] \tag{2.72}$$

An additional correction factor is introduced by Langdon [66] which accounts for the modification of the electron distribution due to the higher ionisation state of the plasma. The Langdon factor reduces the absorption by a factor 2.

2.5.4   **Ponderomotive acceleration**

As discussed in Section 2.4.2 at relativistic laser intensities the $\vec{v} \times \vec{B}$ term of the Lorentz equation becomes significant for the electron motion. The resulting force acts along the laser propagation axis and is able to accelerate the electrons to

such energies that they escape the laser field and enter the overdense plasma. The average kinetic energy of these electrons is equal to the ponderomotive potential defined in Eq. (2.65 & 2.66).

At relativistic intensity the ponderomotive acceleration and the vacuum heating are the two main laser energy absorption mechanisms. As presented in section 2.5.1, vacuum heating depends strongly on the component of the laser electric field that is along the target normal direction E_N. Therefore for p-polarised laser pulses at oblique incidence the vacuum heating mechanism is likely to play a key role in the absorption process. In the case of a normal or near normal incidence $E_N \ll 1$, the ponderomotive absorption dominates. At ultra-relativistic intensities the ponderomotive acceleration dominates over the vacuum heating mechanism at any laser incidence. At a laser intensity $\sim 10^{20}$ Wcm^{-2} a total laser energy absorption into hot electrons of 60% has been measured for a 6° laser incidence [67].

2.6   Laser generated shock

Material is ablated by the interaction of the laser pulse with the target surface. This induces a pressure wave inside the unperturbed material in order to conserve momentum, i.e. a shock wave is launched inside the target, as shown in Fig. 2.3. High power lasers are capable of creating pressures in excess of 500 Mbar [58]. The pressure applied on the target by the laser pulse can be estimated as [68]:

$$P = 400 \left(\frac{I_L}{\lambda_L} \right)^{2/3} \tag{2.73}$$

with I_L in Wcm^{-2} and λ_L in microns.

Shock propagation is usually studied in 1D and the state of the shocked material can be described using the equations of conservation of mass and momentum between the shocked and un-shocked material. In this approximation the shock is considered as a piston propagating inside the target at a given constant velocity.

The velocity of the shock front can be estimated as [69]:

$$v_s = \frac{c_s}{2}\left(\sqrt{1+\chi}+1\right) \tag{2.74}$$

Behind the shock front the velocity of the particles in this region can be estimated as:

$$v_p = \frac{c_s}{2\alpha}\left(\sqrt{1+\chi}-1\right) \tag{2.75}$$

where α is an empirical material constant and:

$$\chi = \frac{4\alpha P}{\rho_0 c_s^2} \tag{2.76}$$

where ρ_0 and c_s are the density and the sound speed in the unperturbed material.

After the end of the laser pulse a rarefaction wave is launched inside the target as the target front surface is allowed to expand in the vacuum. The rarefaction front propagates inside the target at a velocity $v_r \approx v_p$. A second rarefaction wave is generated when the shock wave reaches the rear surface and is reflected back inside the target material. The two counter propagating rarefaction waves will intersect creating a spall. As the shock wave reaches the target rear surface it deforms the surface and launches material in the vacuum at a velocity $v_{rs} \approx 2v_p$ [58].

Shock wave breakout can alter the characteristic of the debris formed in the interaction of a high power laser pulse with a solid target, as will be discussed in chapter 7. In addition low temperature shocks launched by the low intensity ASE pedestal can give rise to a plastic deformation of the target rear surface. This has been shown to change the direction of proton beams accelerated from the target rear surface as demonstrated by Lundh *et al.* [69].

Chapter 3

Ion acceleration mechanisms

3.1 Introduction

The mechanisms responsible for ion acceleration in the context of laser plasma interaction have been extensively studied both theoretically and experimentally during the last decade. The dominant mechanism is strongly linked to the characteristics of the laser driver used, as shown in Fig 3.1. It is important to note that there are no sharp transitions from one acceleration mechanism to another, but rather a gradual change. Another important factor not included in Fig. 3.1 is the target thickness. As will be described in the following sections, it is possible to suppress or enhance a given acceleration mechanism by changing the target thickness.

Fig. 3.1 also includes typical intensities and pulse durations achievable by the laser facilities used for the work presented in this thesis. Those lasers mostly operate in the region dominated by the Target Normal Sheath Acceleration (TNSA) mechanism, and therefore TNSA will be the subject of a detailed presentation. The domain of intensity and pulse duration covered by the ASTRA-GEMINI and VULCAN lasers are situated in a transition region between the TNSA regime and the Radiation Pressure Acceleration (RPA) regime. As a consequence, RPA acceleration will also be discussed.
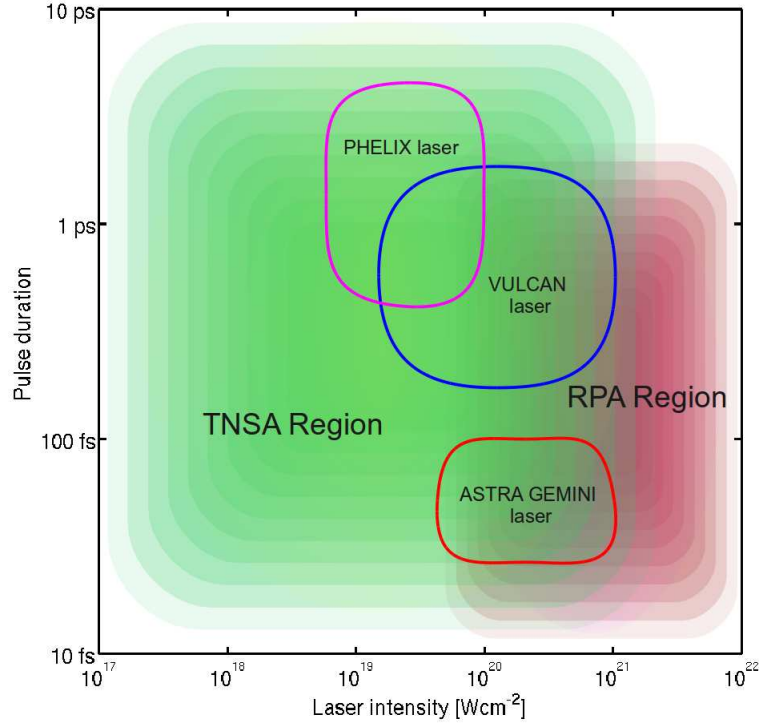
Figure 3.1: Relevance of the different ion acceleration mechanism as a function of the laser driver intensity and pulse duration. It should be noted that the boundaries of the regions are not well defined. Operating parameters of the different laser systems used in this work are also represented.

3.2   Target Normal Sheath Acceleration

3.2.1   Principle

The majority of the experiments on high power laser driven ion acceleration carried out to this day were performed using lasers that can deliver pulses of intensity between 1×10^{18} and 1×10^{20} Wcm^{-2}, with pulse durations between 1 ps and 50 fs. This places the experiments in the region of the TNSA regime, as shown in Fig. 3.1. In the TNSA mechanism, the acceleration of the ions is caused by a strong quasi-electrostatic field at the back of the target resulting from a spatial charge separation of energetic electrons and residual ions.

At the beginning of the laser interaction with the target, part of the laser energy is absorbed and accelerates electrons via various absorption mechanisms described in chapter 2. These hot electrons are accelerated by the laser pulse to relativistic energies ($\sim$MeV) and form a collisionless high current (multi MA)

population that propagates through the target material [70]. Upon reaching the target rear surface, these electrons break out into the vacuum forming a charged cloud that extends over several Debye lengths [70]. The break out of the hot electron population leaves the bulk of the target positively charged. This charge separation is responsible for the generation of a strong quasi-electrostatic field at the rear of the target, with a magnitude of a few TVm^{-1}. The strength of the electrostatic field can be estimated using Eq. (3.1), taken from Wilks *et al.* [71]:

$$E_{sheath} \simeq \frac{k_B T_e}{e \lambda_d} \tag{3.1}$$

for an electron energy $k_B T_e$=1 MeV and λ_D=1 μm, E_{sheath} $\simeq$1 TVm^{-1}.

This field is strong enough to ionise the surface of the target and accelerate the resulting ions away from the target to energy in the tens of MeV range [11–13, 72–76]. A summary of the TNSA mechanism is presented in Fig. 3.2.
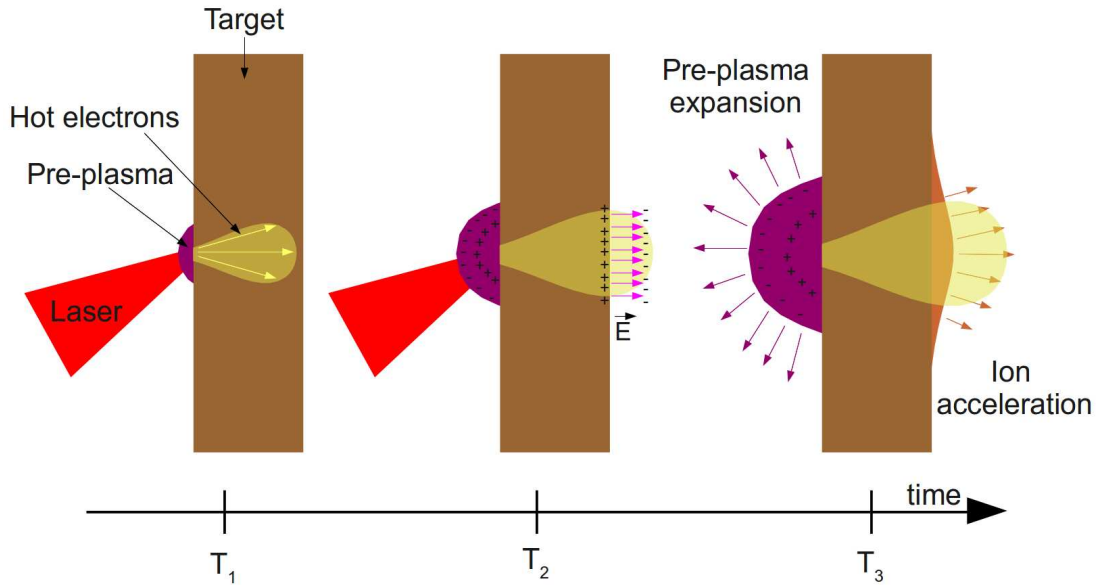
Figure 3.2: Principle of the TNSA mechanism. T_1, the laser pulse irradiates the front surface of the target generating a plasma. Fast electrons are accelerated and propagate through to the rear surface. T_2, once the hot electrons reach the target rear surface they break out into the vacuum and some escape the target. A strong quasi-electrostatic field ($\sim$$TVm^{-1}$) appears caused by the charge separation. T_3, the field is strong enough to ionise the target surface and accelerate the ions away from the target. Ion acceleration also occurs at the front surface, mainly due to the expansion of the laser-generated plasma.

At this point it is necessary to consider the transport of the fast electrons in the target. The fast electrons produced in the laser absorption region form a beam that propagates within the target with a typical divergence angle between 20° and 40° [77]. Such beams will generate peak currents of a few MA [78] which in turn can generate electric and magnetic fields of magnitude high enough to prevent the propagation of the electrons in the target bulk.

The electric field E generated by the fast electron beam can be approximated by:

$$\frac{\partial \vec{E}}{\partial t} = -\frac{\vec{j_f}}{\varepsilon_0} \tag{3.2}$$

where $\vec{j_f}$ is the current density of the fast electrons $\vec{j_f} = -en_f\vec{v_f}$ with n_f and $\vec{v_f}$ the density and the velocity of the fast electrons respectively. In typical conditions the magnitude of the field obtained using Eq. (3.2) is $E=10^{15}$ Vm^{-1}.

The magnitude of the resulting magnetic field can be estimated using [79]:

$$B = \frac{\mu_0 I_f}{2\pi r_L} \tag{3.3}$$

where I_f is the fast electron current intensity, and r_L is the laser focal spot radius. For typical laser conditions $B \simeq 10^6$ T.

The current intensity limit below which the electron beam can propagate without self generating sufficiently strong electric and magnetic fields to stop it is governed by the Alfvèn limit [80]:

$$I_A = 1.7 \times 10^4 \beta\gamma \tag{3.4}$$

where $\beta = v/c$ with v the electron velocity, and $\gamma = 1/\sqrt{1-\beta^2}$. In conditions relevant to this work I_A is of the order of a few 10s of kA, which is significantly lower than the intensity of the fast electron current.

For the hot electrons to be able to propagate a balancing return current $\vec{j_r}$ must appear that satisfies:

$$\vec{j_f} + \vec{j_r} = 0 \tag{3.5}$$

If Eq. (3.5) is satisfied then the Alfvèn limit will not be breached and the fast

electron will be able to propagate through the target bulk. The electrons constituting the return current originate from the target material itself. In the case of conductors this is possible via the free electrons present in the material, while ionisation is responsible for the return current in the case of insulator targets. As stated previously, the fast electron current can be considered collisionless as the electron mean free path is greater than the target thickness, whereas the return current, being significantly colder than the fast electrons, is collisional and is affected by the target material properties such as the resistivity.

The two currents, being counter-propagating, are prone to develop instabilities which can lead to filamentation of the fast electron beam. This will affect the ion acceleration by modifying the TNSA field.

Once the fast electron current has reached the rear surface of the target the most energetic electrons are able to escape before the electrostatic sheath field is established. The rest of the hot electron population is pulled back inside the target by the field and travel to the front surface where a similar reflection can occur. This is referred to as electron recirculation or refluxing and typically lasts over a period of the order of the laser pulse duration. Recirculation of the electrons plays an important role in the TNSA mechanism as it can increase the duration of the accelerating field [81, 82].

3.2.2   Modelling the TNSA mechanism

The acceleration of ions is a complex process involving a variety of physical phenomenon such as:

1. laser pulse energy absorption to fast electrons at the target front surface;

2. fast electron transport within the target and

3. the temporal and spatial evolution of the sheath field giving rise to ion acceleration at the rear surface.

Only a limited number of these phenomenon are accessible to direct measurements. Therefore it is necessary to make a series of assumptions in order to

develop a model that can be used to predict some of the ion beam characteristics and which can be benchmarked against measurable experimental parameters such as the maximum ion energy. Many different models have been developed in recent years these fit into the categories of:

- fluid models [83, 84];

- hybrid-PIC models [85] and

- quasi-static field models [70, 86–88]

The fluid approach: the Mora model

The 1D plasma expansion model proposed by Mora [83] is one of the most widely used models and is therefore discussed below. This model is based on the isothermal 1D free expansion of a plasma into the vacuum [89, 90]. It assumes that the ions are cold and initially at rest with a sharp boundary with the vacuum, while the electron density n_e follows a Boltzmann distribution:

$$n_e(z) = n_{e0} \exp\left[-\frac{e\Phi(z)}{k_B T_e}\right] \tag{3.6}$$

where n_{e0} is the electron density of the unperturbed plasma and Φ is the electrostatic potential chosen to satisfy the Poisson equation:

$$\frac{\partial^2 \Phi(z)}{\partial z^2} = \frac{e}{\varepsilon_0}(n_e - qn_i) \tag{3.7}$$

where n_i is the ion density and q the ion charge number. At $z \rightarrow -\infty$ (inside the target) charge neutrality is assumed and $n_e = qn_i$. The electric field E at the border of the plasma with the vacuum is obtained by integrating Eq. (3.7), and is responsible for the ion expansion in the vacuum, described by the equations of continuity and motion:

$$\frac{\partial n_i}{\partial t} + v_i \frac{\partial n_i}{\partial z} = -n_i \frac{\partial v_i}{\partial z} \tag{3.8}$$

$$\frac{\partial v_i}{\partial t} + v_i \frac{\partial v_i}{\partial z} = -\frac{qe}{m_i}\frac{\partial \Phi}{\partial z} \tag{3.9}$$

where v_i is the ion velocity.

Self-similar solutions to Eq. (3.8) & (3.9) can be found if the plasma is assumed to be quasi-neutral ($n_e \simeq q n_i$). The final position and velocity of the ions is given by the solutions:

$$z_f \simeq 2\sqrt{2\,e_N}\,\lambda_{D0}\left[\tau \ln\left(\tau + \sqrt{\tau^2 + 1}\right) - \sqrt{\tau^2 + 1} + 1\right] \tag{3.10}$$

$$v_f \simeq 2\,c_s \ln\left(\tau + \sqrt{\tau^2 + 1}\right) \tag{3.11}$$

where $\tau = \omega_p t_a / \sqrt{2\,e_N}$.

It is clear from Eq. (3.11) that when the acceleration time $t_a \to \infty$, $v_f \to \infty$, which is clearly a non physical result. Therefore an upper limit must be imposed to t_a. The laser pulse duration τ_L constitute an obvious choice. However previous work by Fuchs *et al.* [91] shows that for laser intensities greater than 3×10^{19} Wcm^{-2} the acceleration time can be approximated as:

$$t_a \simeq 1.3\,\tau_L \tag{3.12}$$

A number of other assumptions have to be made in order to estimate the value of the parameters relevant to Eq. (3.11). First the hot electron energy can be calculated using the ponderomotive potential [62] defined in chapter 2. The electron density in the sheath is estimated using:

$$n_{e0} = \frac{N_e}{c\tau_L\pi r_{sheath}^2} \tag{3.13}$$

where r_{sheath} is the sheath radius and N_e is the electron number in the sheath. The radius of the electric sheath r_{sheath} is obtained by assuming that the hot electrons have a ballistic propagation through the target [92, 93]:

$$r_{sheath} = r_L + l\tan\theta \tag{3.14}$$

where r_L is the laser focal spot radius, l is the target thickness and θ is the

divergence half angle of the fast electron beam, which is of the order of a few tens of degrees and depends on the laser intensity as demonstrated by Green *et al.* [77]. The electron number N_e is calculated as follow:

$$N_e = \frac{\eta_{L \to e} \mathcal{E}_L}{k_B T_e} \qquad (3.15)$$

where $\mathcal{E}_L$ is the laser energy and $\eta_{L \to e}$ is the conversion efficiency of the laser energy to the hot electrons, calculated as [86]:

$$\eta_{L \to e} = 1.2 \times 10^{-15} I_L^{0.74} \qquad (3.16)$$

with a maximum value of 0.5 when $I_L \geq 3 \times 10^{19}$ Wcm^{-2} [72, 86]. The average electron energy $k_B T_e$ is estimated using the ponderomotive potential defined in Chapter 2.4.3.

Figure 3.3: Comparison of the Mora model predictions for two different pulse durations, 1 ps (solid line) and 50 fs (dashed line) with experimental data for various laser facilities as detailed in the main text.

Fig. 3.3 shows the maximum proton energy calculated with the Mora model for

different laser pulse durations, 1 ps and 50 fs, as a function of the laser intensity, at a constant target thickness of 1 μm, compared with previous experimental results obtained for a range of laser and target conditions. Previous experimental data are included, as obtained from Ref. [32, 94–96] for short pulses (50-100 fs), from Ref. [81, 93, 94] for medium duration pulses (100-300 fs) and from Ref. [12, 73–76, 97–99] for the long pulse duration (400 fs-1 ps). We can see from Fig. 3.3 that the fluid model proposed by Mora reproduces the increasing trend of the maximum energy quite well. However, in the case of the longer pulse duration (1 ps) it over estimates the maximum energy.

The hybrid-PIC approach: the Robinson *et al.* model

In the model proposed by Robinson *et al.* [85] the accelerating field experienced by protons beyond the heavy ion front is obtained by integrating the non linear Poisson's equation derived by Passoni [100]:

$$\frac{\partial^2 \Phi}{\partial z^2} = \frac{en_e}{\varepsilon_0} \exp\left(\frac{e\Phi(z)}{k_B T_e}\right) \tag{3.17}$$

where Φ is the electric potential applied to the proton beyond the heavy ion front. Eq. (3.17) can be integrated to obtain the spatial variations of the electric field felt by the proton:

$$E_{sheath} = \frac{k_B T_e \sqrt{2}}{e\lambda_D} \exp\left(\frac{e\Phi_0}{k_B T_e}\right) \left[1 + \frac{z - z_f}{\lambda_D \sqrt{2}} \exp\left(\frac{e\Phi_0}{k_B T_e}\right)\right]^{-1} \tag{3.18}$$

where z_f is the position of the heavy ion front given by Eq. (3.10) and Φ_0 is the electric potential at the heavy ion front. However to simplify the calculation of the maximum proton energy the accelerating field at the ion front is neglected ($\Phi_0 = 0$). $k_B T_e$ is estimated using the ponderomotive potential defined in Chapter 2.4.3. The maximum proton energy can then be obtained by integrating the motion of a proton in the field E_{sheath}. The results of the calculation for varying laser intensity and two different pulse durations (1 ps and 50 fs) and a 1 μm target thickness are shown in Fig. 3.4 along side experimental data from previous work as detailed above.

As seen in Fig. 3.4 the trend given by the model proposed by Robinson *et al.* [85] is in good agreement with the experimental data. In the case of the longer pulse duration the maximum proton energy is slightly over estimated for the highest intensities and so is the energy for the lowest intensities in the short pulse case. Nonetheless the vast majority of the experimental data points are between the predictions of the model for the range of laser pulse duration used experimentally.

Figure 3.4: Comparison of the Robinson *et al.* model [85] for two different laser pulse durations, 1 ps (solid line) and 50 fs (dashed line) with experimental data from previous work as detailed in the main text.

The quasi-static field approach: the Schreiber *et al.* model

The model proposed by Schreiber *et al.* [86] is based on a surface charge being set up by the hot electrons on the target rear surface. The electrons are assumed to uniformly fill a circular region with radius r_{sheath}, obtained using Eq. (3.14). It is assumed that when these electrons break out into the vacuum they set up a positive charge Qe on the target rear surface, with Q the number of charge. This

leads to a surface charge density $Qe/\pi r_{sheath}^2$ for which the resulting potential can be calculated by solving Poisson's equation:

$$-e\Phi(\xi) = \frac{Qe^2}{2\pi\varepsilon_0 r_{sheath}} s(\xi) \tag{3.19}$$

If z is the target normal direction with the rear surface at $z = 0$, ξ is defined as $\xi = z/r_{sheath}$ and $s(\xi) = 1 + \xi - \sqrt{1 + \xi^2}$. Eq. (3.19) can be used to calculate the energy $\mathcal{E}_i(\xi)$ gained by an ion of charge qe over a given distance:

$$\mathcal{E}_i(\xi) = -qe\Phi(\xi) = \mathcal{E}_{i,\infty} s(\xi) \tag{3.20}$$

where $\mathcal{E}_{i,\infty} = qk_B T_E r_{sheath}/\lambda_D$ represents the maximum theoretical energy that can be gained by an ion in the potential Φ. Considering that the number of fast electrons accelerated by the laser can be estimated using Eq. (3.15) $\mathcal{E}_{i,\infty}$ can be rewritten:

$$\mathcal{E}_{i,\infty} = 2qm_e c^2 \sqrt{\frac{\eta_{L\to e}P_L}{P_R}} \tag{3.21}$$

where P_L is the laser power, P_R is the relativistic power unit, $P_R =$ 8.71 GW. $\mathcal{E}_{i,\infty}$ represents the theoretical maximum energy an ion could gain in the potential Φ for a certain laser power P_L in the case of an infinitely long acceleration.

By integrating the equation of motion:

$$\frac{\partial\xi}{\partial t} = \sqrt{\frac{2\mathcal{E}_i(\xi)}{m_i r_{sheath}^2}} \tag{3.22}$$

the following equation is obtained:

$$\frac{\tau_L}{\tau_0} = X\left[1 + \frac{1}{2(1 - X^2)}\right] + \frac{1}{4}\ln\frac{1 + X}{1 - X} \tag{3.23}$$

where $\tau_0 = m_i r_{sheath}^2/(2\mathcal{E}_{i,\infty})$. The dependence in maximum ion energy of Eq. (3.23) is given through:

$$X = \sqrt{\frac{\mathcal{E}_{max}}{\mathcal{E}_{i,\infty}}} \tag{3.24}$$

Unfortunately it is not possible to explicitly define $\mathcal{E}_{max}$ using Eq. (3.23) and

therefore the value of X must be numerically interpolated. This is done by solving Eq. (3.23) for a wide range of values of X. The ratio τ_L/τ_0 is then calculated using the experimental laser conditions, and the solution of Eq. (3.23) is interpolated to find the value of X that will match τ_L/τ_0.

Fig. 3.5 shows the results of the Schreiber model for a fixed target thickness of 1 μm and two laser pulse durations (1 ps and 50 fs) with varying laser intensity compared with experimental results from previous work, as detailed above. The increasing trend of the maximum proton energy with increasing laser intensity is reproduced by the model. However the rate of increase is largely over estimated. For higher laser intensity the model over-estimates the maximum energy for both the short pulse and the long pulse case. However for laser intensities between 1×10^{18} Wcm^{-2} and 5×10^{19} Wcm^{-2}, the range of energies given by the model for the two laser pulse durations is in good agreement with the experimental data.
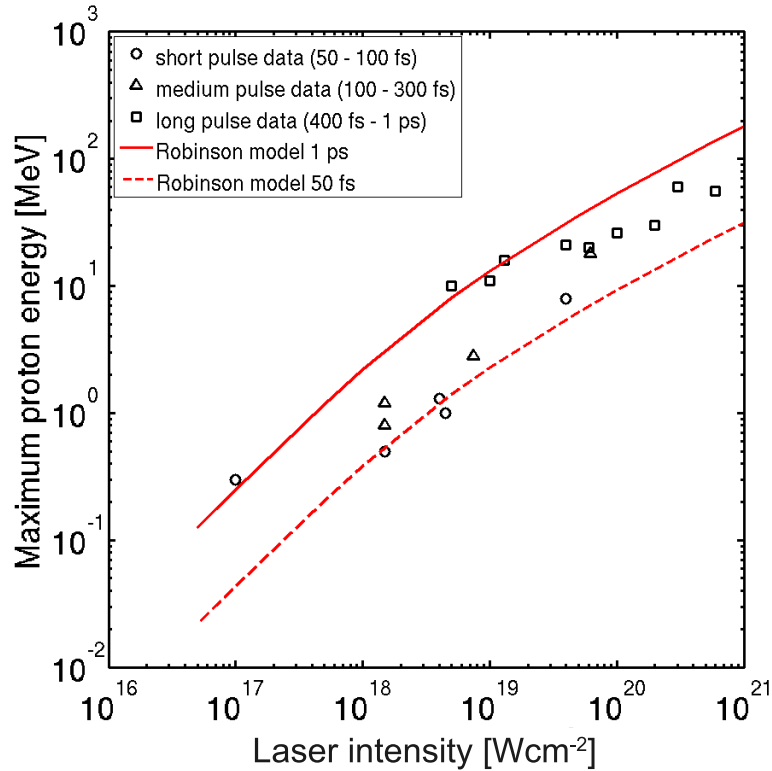

Figure 3.5: Comparison of the Schreiber *et al.* model for two different pulse durations, 1 ps (solid line) and 50 fs (dashed line) with experimental data for various laser facilities as detailed in the main text.

3.2.3 TNSA ion beam characteristics

Origin of the ions

The properties of the TNSA generated ion beam have been extensively studied both experimentally [11, 12, 74, 75, 93, 98, 101] and with PIC simulations [75, 82, 102–105]. One of the first issues to arise concerned the origin of the measured multi-MeV ions. Some measurements indicate that the ions originate from the rear surface of the target [12, 72, 106], while others show that they are generated at the front of the target [11, 13, 107]. Allen *et al.* [108] experimentally demonstrated that the ions actually originate from both the front and the rear surface of the target by cleaning each surface separately using an ion gun. This was later confirmed by Fuchs *et al.* [76, 109], and both experiments showed that the rear surface emission dominates over the front surface.

As reported by Snavely *et al.* [12], protons are the dominant species constituting the TNSA accelerated ion beams. This is due to their high charge-to-mass ratio and the low ionisation potential of hydrogen, which means that they are created first and accelerated more efficiently by the quasi-electrostatic sheath field. Once protons are generated they screen the sheath field, thereby reducing the efficiency of the ionisation and acceleration of heavier ion species. Carbon has a low enough ionisation potential that carbon ions are observed consistently together with protons. Protons and carbon ions usually always form part of the ion beam even when the main target sample is not hydrogen or carbon. This is explained by the presence of hydrocarbon and H_2O contamination layers on the surfaces of the target [110]. Efficient acceleration of the heavy ions originating from the target bulk is achieved if the contamination layers are removed prior to the laser irradiation. This can be done by resistively heating the target to desorb the contaminant layers [110, 111], by using an ion gun [108] or by laser ablation [112].

Energy distribution

TNSA ion beams have a distinct Maxwellian energy distribution as shown in Fig. 3.6 (a). The spectrum typically has a sharp maximum energy cut off. It is possible to obtain the average temperature of the beam by fitting the following formula:

$$N_i(\mathcal{E}) = N_{i0} \exp\left(-\frac{\mathcal{E}}{k_B T_i}\right) \tag{3.25}$$

where N_{i0} is a fitting parameter and $\mathcal{E}$ is the ion energy. As shown in Fig. 3.6 (a) the ion beam is usually best fitted by using multiple temperatures. The temperatures used to fit the spectra usually increase with the ion energy as seen in Fig. 3.6 (a).

As shown in Fig. 3.6 (b) the maximum ion energy is strongly linked to the laser intensity as well as the pulse duration. A review by Borghesi *et al.* [101] gives scaling laws for the maximum ion energy as a function of the laser intensity obtained by sampling data from many laser systems:

- $\propto I\lambda^2$ for laser pulse duration < 150 fs

- $\propto \sqrt{I\lambda^2}$ for laser pulse duration between 300 fs and 1 ps

A comparison of the scaling laws proposed by Borghesi *et al.* [101] with experimental data from various laser facilities, as detailed in Section 3.2.2, is presented in Fig. 3.6 (b), and good agreement is found between the scaling laws and the experimental data.

Beam divergence

The accelerating sheath field strength at the rear surface of the target has a Gaussian distribution in the transverse direction as measured by Romagnani *et al.* [41]. The shape of the accelerating sheath was measured by using a laser driven proton beam to probe the electric field on the rear surface of a second laser irradiated target.

As the ions are produced in the rear surface sheath field they are pulled away from the surface along the target normal direction. Due to the Gaussian

Figure 3.6: (a) Example of TNSA proton energy spectra from a 1 μm thick carbon target irradiated with the ASTRA-GEMINI laser, with Maxwellian fits. (b) Maximum proton energy as a function of laser intensity from the scaling laws proposed by Borghesi *et al.* [101] compared with previous experimental work, as described in Section 3.2.2.

transverse distribution of the accelerating field, the ions situated in the central region of the field are accelerated faster than those at larger radius. This results in a Gaussian shaped ion front as shown in Fig. 3.7 (a). The acceleration of the ions being directed along the normal of the ion front, i.e. along the transverse gradient of the electric field [113, 114], the ions in the central region of the sheath field are accelerated in a cone of smaller divergence half angle than those at larger radii, as illustrated in Fig. 3.7 (a). Due to the acceleration field spatial-intensity distribution, the highest energy ions originate at the central region of the field, while the lowest energy ions are produced in regions of larger radii. This results in beams of increasing divergence with decreasing energy as shown in Fig. 3.7 (b).

The circular ion beams usually observed in TNSA acceleration experiments are a direct result of the cylindrical symmetry of the sheath field. Roth *et al.* [115] demonstrated that the spatial distribution of the ion beam can be modified by changing the symmetry of the accelerating field by changing the shape of the laser focal spot. It is also possible to control the ion beam spatial distribution by using wire targets, resulting in a linear ion beam [40], or by changing the shape

of the target as described in chapter 6.

Figure 3.7: (a) Schematic illustrating the divergence of the TNSA accelerated ion beams for different ion energies: $E_1 > E_2 > E_3$. (b) An example measurement of the divergence of a TNSA proton beam as a function of energy produced using the VULCAN laser. (c) Measurements of the TNSA proton beam source size as a function of energy taken during an experiment using the VULCAN laser.

Ion source size

Cowan *et al.* [15] were the first to demonstrate the mapping of micron scale structures machined into the target rear surface into the proton beam spatial intensity distribution. This is the result of the electrostatic sheath field following the local contour of the target surface, and can be used to measure the size of the ion source. Cowan *et al.* [15] and Roth *et al.* [115] did so by using targets with equally spaced identical grooves on the back surface, and counting the number of grooves reproduced in the proton beam. They found that for laser intensities between 10^{18} Wcm^{-2} and 10^{20} Wcm^{-2} and pulse duration of ~1 ps, the size of the ion source is energy dependent [115] and is of the order of a few hundreds of microns for target thickness from 5 μm up to 100 μm. This is shown in Fig. 3.7

(c). Other techniques can be used to measure the ion source size such as placing a metallic mesh at a given distance between the target and the detector [116] or by using a knife edge ion projection [117].

Borghesi *et al.* [116] have carried out measurements of the magnification of a mesh by a TNSA proton beam. They found that the magnification expected for a point projection imaging system always over estimates the measured experimental magnification. These differences can be explained if magnification is calculated for protons originating from a virtual source situated at a distance in front of the target. The size of this virtual source can be estimated using numerical codes to simulate the propagation of the protons. Borghesi *et al.* [116] found for a picosecond laser pulse duration a source size of $\sim$10 μm situated a few hundreds microns in front of the target.

Beam laminarity and emittance

The possibility to reproduce micron scale structures imprinted on the back surface of the target within the TNSA ion beam distribution indicates that the ion beam is highly laminar. A flow can be defined as laminar if the streamlines are parallel, as opposed to a turbulent flow where the streamlines will cross many times. In the case of ion beams this translates into protons whose trajectories from source to detector do not cross or overlap.

The transverse emittance of a TNSA ion beam is defined using the source size and the angle of emission. The transverse emittance can then be used to estimate the degree of laminarity of the proton beam [116]. The smaller the emittance of the beam, the higher the laminarity is. For laser-driven ion beam the transverse emittance is $<4\times10^{-4}$ mm.mrad [15] which is about a 100 times smaller than typical RF accelerators. It is believed that the low emittance results from the fact that the ions are rapidly accelerated from a cold source and also because electrons co-propagate with the ion beam, preventing space charge spreading.

3.3 Radiation Pressure Acceleration

Recent theoretical work by Esirkepov *et al.* [118] and Robinson *et al.* [119] have shown that for high enough laser intensities the acceleration of ions is dominated by the laser radiation pressure [120]. The total radiation pressure on target can be estimated by [121]:

$$P_{rad} = \frac{2RI_L}{c} \tag{3.26}$$

where R is the reflectivity of the plasma, for solid density $R \simeq 1$. It has been shown that this acceleration mechanism could be achieved with laser intensities $\geq 10^{21}$ Wcm^{-2} for circularly polarised laser pulses [119], and $\geq 10^{23}$ Wcm^{-2} for linearly polarised laser pulse [118]. The difference in laser intensity is due to the fact that circular polarisation provides a constant ponderomotive expulsion of electrons making the RPA processes more efficient. Mono-energetic ion beams, with a maximum energy in the GeV range are expected for nanometre thick solid targets. For the RPA mechanism the scaling of $\mathcal{E}_{max}$ with I_L ($\propto I_L$) is much more favourable than for TNSA ($\propto I_L^{1/2}$).

3.3.1 The 'light sail' mode

The RPA mechanism can be divided into two separate modes. In the case of a sufficiently thin target (tens of nanometres) irradiated by a large focal spot beam, the 'light sail' mode dominates. In this mode the radiation pressure of the laser pushes forward all the electrons in the focal spot while the ions stay still due to their much higher mass. This results in the creation of a strong charge separation field that accelerates the ions, as illustrated in Fig. 3.8. The electrons and ions are co-moving and the electrons act as a relativistic mirror for the laser pulse. Due to the Doppler effect the frequency of the reflected light becomes $\omega_r \simeq \omega_L/4\gamma^2$ where γ is the relativistic factor of the accelerated foil. If $\gamma \gg 1$ almost all the laser pulse energy is transferred to the foil. This mode has been the focus of many theoretical studies [118, 122–124], resulting in the following scaling law for the

maximum achievable ion energy:

$$\mathcal{E}_{max} = \frac{2\mathcal{E}_L^2}{N_i\left(2\mathcal{E}_L + N_i m_i c^2\right)} \tag{3.27}$$

where N_i represents the number of ions accelerated. It can be seen from Eq. (3.27) that if the energy contained in the laser pulse ($\mathcal{E}_L$) is much larger than the total rest energy of the ions ($N_i m_i c^2$) all the laser energy goes into the ions ($\mathcal{E}_{iMax} \simeq \mathcal{E}_L / N_i$).

In the light sail mode the foil can be subject to hydrodynamic instabilities of the Rayleigh-Taylor type [125]. Such instabilities have a growth rate depending on the target and laser parameters and can be estimated as follow:

$$\tau_{rel} = \frac{1}{6\omega_L \lambda_L^2}\sqrt{\frac{(2\pi)^3 R_0}{k^3}} \tag{3.28}$$

$$\tau_{non\ rel} = \frac{1}{\omega_L}\sqrt{\frac{2\pi}{k R_0}} \tag{3.29}$$

where k represents the laser wave vector and:

$$R_0 = \frac{E_{L0}^2}{m_i l \omega_L^2 n_e} \tag{3.30}$$

with l the target thickness and E_{L0} the laser electric field strength. τ_{rel} represents the instability growth rate in the relativistic regime, while $\tau_{non\ rel}$ refers to the same for the non relativistic case.

A number of conditions have to be fulfilled in order for the light sail mode to be reached:

- first, all the electrons contained in the laser focal spot have to be repelled;

- second, the focal spot size must be large so the acceleration can be considered quasi-one-dimensional, and

- third, the acceleration time of the ions must be short enough to prevent the apparition of hydrodynamic instabilities.

Figure 3.8: Schematic of the 'light sail' mode of the RPA ion acceleration.

3.3.2 The 'hole boring' mode

The other main mode of the RPA regime is the 'hole boring' mode [126–128]. In this mode the laser radiation pressure pushes the electrons forward creating a thin pile up in front of the laser pulse. This results in an electron density spike greater than the critical density of the laser. A region free of electrons behind the density spike is created, and the ions are accelerated via a strong charge separation field [129]. This double layer structure, illustrated in Fig. 3.9, forms an electrostatic shock propagating inside the plasma and therefore the 'hole boring' mode is also referred to as collisionless shock acceleration. Work by Zhang *et al.* [130] and Macchi *et al.* [127] have shown that the hole boring process is more efficient if a circularly polarised laser pulse is used as the heating of the plasma is greatly reduced.

1D models developed by Robinson *et al.* [131] and Schlegel *et al.* [129] predict quasi-mono energetic ion spectra with a maximum ion energy defined as:

$$\mathcal{E}_{iNR} = 2m_i c^2 \Xi \tag{3.31}$$

Figure 3.9: Schematic of the double layer structure in the RPA 'hole boring' mode. The dashed lines represent the ion (magenta) and electron (blue) density. The electric field resulting from the charge separation is also shown (green solid line).

$$\mathcal{E}_{iR} = 2m_i c^2 \frac{2\Xi}{1 + 2\sqrt{\Xi}} \tag{3.32}$$
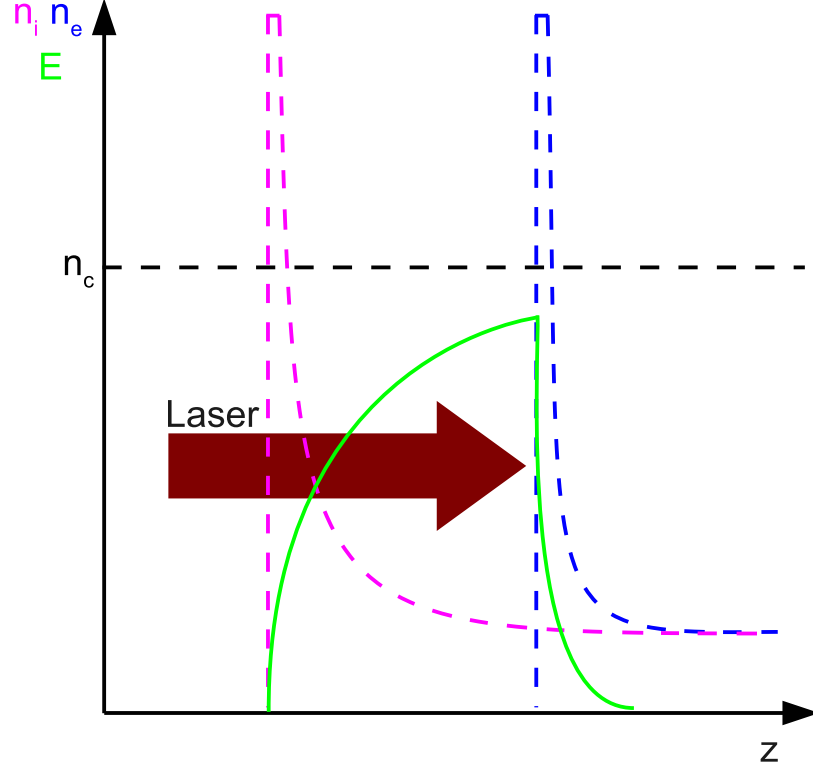
$\mathcal{E}_{iNR}$ and $\mathcal{E}_{iR}$ represent the non relativistic and relativistic case respectively with $\Xi = I_L / m_i n_i c^3$.

It is possible for the ions accelerated by the 'hole boring' process to gain an additional acceleration when they reach the target rear surface [103, 128]. This is only possible if the 'hole boring' ions arrive at the rear surface before the electrostatic sheath field generated by the TNSA mechanism is screened by the ions originating from the front surface.

Experimental measurements of hole boring accelerated protons have been reported by Palmer *et al.* [132]. They have used a CO_2 laser (λ_L=10 μm) focussed in an overdense hydrogen gas jet and measured protons with an energy spread of ∼4% and a peak energy of ∼1 MeV. Despite the low energy measured

they have observed proton spectra with no TNSA background. Henig *et al.* [133] have observed mono energetic features in ion beams accelerated using circularly and linearly polarised laser pulses focussed to an intensity of 7×10^{19} Wcm^{-2} on diamond-like carbon foil. They found that when changing to circularly polarised pulses the number of high energy C^{6+} ions increases, giving rise to a mono energetic feature. They attributed this feature to the hole boring mode of the RPA mechanism.

3.4   Conclusion

In the past decade the acceleration of ions to multi-MeV energies driven by high power lasers has been extensively studied experimentally and theoretically. To make these laser driven ion beams relevant for the envisaged applications it is necessary to optimise the acceleration process, a goal that the community is actively pursuing.

With the increase in the power of the large laser systems it is becoming possible to reach new more efficient acceleration mechanisms such as RPA driven processes. But the intensity of today's lasers is still at the lower limit of the RPA regime and the TNSA mechanism is still the dominant acceleration process. The work presented in this thesis is conducted in the TNSA regime and is aimed at optimising and controlling the properties of the ion beams.

Chapter 4

Methods

4.1 Introduction

The investigation of high power laser accelerated ion beams is a difficult process involving the use of state of the art technologies. The key component of any experimental study, as presented in this thesis, is the laser system used which defines, via its pulse parameters (duration, energy, wavelength etc), what objectives can be pursued during a given experimental campaign. The very nature of the work presented in this thesis requires the use of the most intense laser pulses available today (1×10^{19} - 1×10^{21} Wcm^{-2}). Such laser facilities cost several millions of pounds to build and run. Although increasingly high power lasers are being installed in universities, the most intense laser systems are usually part of large national research facilities such as the Central Laser Facility (CLF) at the Rutherford Appleton Laboratory (RAL) in the UK, the LULI facility at the Ecole Polytechnique in France or the PHELIX laser at GSI in Germany, as presented in Fig. 4.1. These facilities are open for access to national and international research groups who compete for the available beam time. Once or twice a year a call for experiments is made to the research community and any group interested in using the facility can submit a proposal for access. The proposals are then reviewed by a panel, who will allocate beam time based on the scientific merit and technical feasibility of the proposed experiment.

The typical duration of an experiment at a large scale facility is between 3 and

Figure 4.1: Location of the various high power laser facilities where the work presented in this thesis was carried out. 1 University of Strathclyde, Glasgow UK; 2 RAL (VULCAN and ASTRA-GEMINI lasers), Oxfordshire UK; 3 GSI (PHELIX laser), Darmstadt Germany.

6 weeks during which time the facility is responsible for the good delivery of the laser pulses. The research group is responsible for the design of the experiment, the set up of the beam lines, targets, diagnostics and the running of the experiment. The target chamber is a large vacuum vessel in which the target and diagnostics are positioned. The location of the target in the chamber is typically at, or close to the centre of the chamber and therefore its position is generally referred to as the Target Chamber Centre (TCC). Once the laser focus position is defined, the diagnostics are positioned in the chamber and aligned. The number of diagnostics that can be installed in the chamber depends on the space around the target. A wide variety of techniques are used to diagnose the interaction of the laser pulse with a solid target, as used in this thesis, and involve spatial, spectral and energy resolved measurements of ions, X-rays and transition radiation.

When the experiment is complete, the data must be analysed and numerical simulations are often required to understand and explain the experimental observations. These are usually performed using advanced simulation tools such as

Particle In Cell codes, run on multi-core super computer clusters. It is only once all this work is complete that the results can be written up and submitted for publication.

In this chapter the various diagnostics and simulation codes used to perform the work discussed in this thesis are presented. The operation of a high power laser system is also briefly described.

4.2   High power Laser systems

4.2.1   Introduction

In 1917, Einstein [134] effectively laid down the basis of laser physics when he postulated that an atom could decay from an excited state spontaneously or via stimulated emission. In the 1950's, the use of stimulated emission as a means to amplify electromagnetic waves was demonstrated using microwave radiation. In 1959 the term laser was proposed by Gordon as an acronym for Light Amplification by Stimulated Emission of Radiation and the first functioning optical laser was realised in 1960 by Maiman [135].

The amplification of light by stimulated emission relies on the creation of a population inversion in the gain medium. It is most efficiently realised using a 4 energy level configuration as illustrated in Fig 4.2. An external energy source, typically flash lamps, is used to 'pump' a sufficient number of atoms from the ground level E_1 to an excited level E_4. These atoms then rapidly decay to a metastable state E_3 without the emission of a photon. The transition from E_3 to E_2 is the lasing transition, and is chosen to have a long lifetime, of the order of 100s μs, so that population inversion can occur. The transition from the lower laser level E_2 to the ground level E_1 is also a short lifetime non radiative transition. Due to the physical processes involved, a laser is a device that produces highly coherent light, both spatially and temporally.

To reach the high energies necessary for high energy ion acceleration, the pulses have to be amplified by passing through multiple amplifiers. As the energy contained in the pulse increases the size of the beam has to be increased to prevent
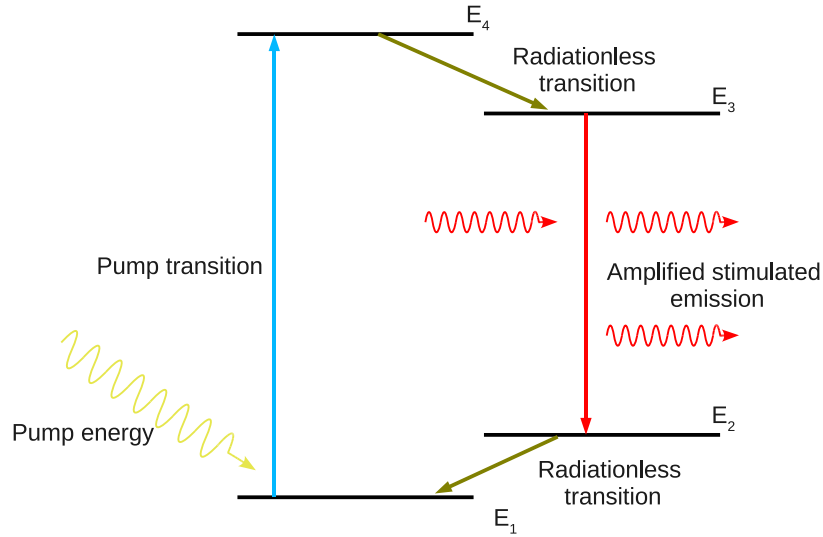
Figure 4.2: Schematic of a laser transition. Atoms in the gain medium are excited from the ground level E_1 to E_4 where the decay to a metastable state E_3 creates the population inversion. The transition from E_3 to E_2 is the laser transition. It can occur spontaneously or by stimulated emission. Both transitions E_4 to E_3 and E_2 to E_1 are radiationless.

damage to the different optical components of the amplification chain. This has limited the maximum achievable energy for many years as it is not possible to increase the size of the optics indefinitely. A breakthrough was made in 1985 when Strickland and Mourou [136] demonstrated the Chirped Pulse Amplification (CPA) method in which the laser pulse is stretched before amplification. Once the pulse has attained the desired energy it is temporally compressed to almost its original duration before being focussed on the target, see Fig. 4.3. The temporal stretching enables more energetic beams to travel through the optics of the chain which would be damaged by shorter pulses. The CPA technique has enabled the construction of lasers delivering power in excess of a PW.

One of the main issues when investigating the interaction of a laser pulse with a thin solid target is the intensity contrast of the beam. The contrast of the laser is defined as the ratio between the intensity of the main pulse and the pedestal of the pulse. As mentioned previously, the laser transition can occur spontaneously. This emission is not temporally synchronised with the main pulse, giving rise to a pedestal surrounding the main pulse as shown in Fig. 4.4 (a). It will also be amplified by the laser chain to energies that can be high enough
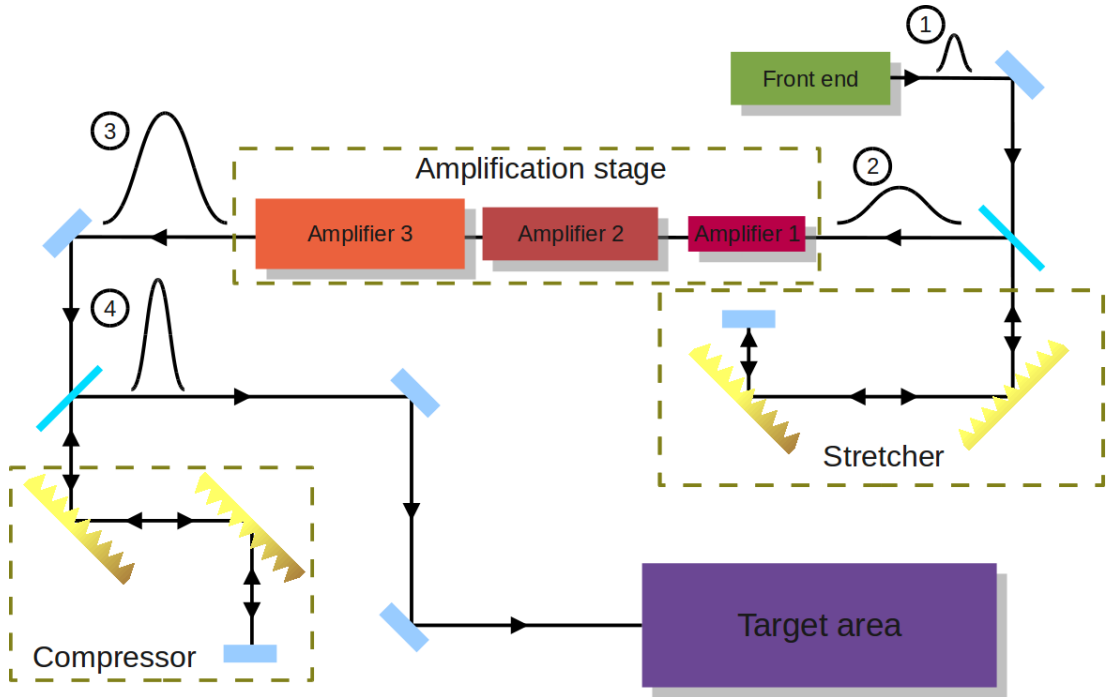
Figure 4.3: Schematic of a CPA laser chain. 1, an oscillator is used to produce a low energy (10^{-9} J) short duration pulse (10s fs); 2, the pulse is then stretched in time using gratings by a factor $\sim 10^4$; 3, the stretched pulse is amplified by a factor 10^6 - 10^{10}; 4, the pulse is recompressed to almost its original duration and delivered to the target area.

to ionise the target. Such an emission is referred to as Amplified Spontaneous Emission (ASE). In addition to the ASE, pre-pulses can be generated during the stretching/compressing and the amplification stage.

The contrast of the laser can be greatly improved by the use of a plasma mirror [137–140]. The principle of the plasma mirror hinges on the transition from a highly transmissive medium to a highly reflective one. Practically this is achieved with a simple slab of anti-reflection (AR) coated glass onto which the laser is incident at the Brewster angle to minimise reflections. The beam is loosely focussed on the plasma mirror so that the intensity of the ASE pedestal and the pre-pulses is not high enough to ionise the glass and are transmitted. When the rising edge of the main pulse reaches intensity $\sim 10^{14}$ Wcm^{-2} the glass is ionised, generating an over-dense plasma layer in front of the glass. The remaining part of the pulse is then reflected off the critical surface of the plasma, effectively improving the contrast by a factor $\sim 10^2$. If this occurs prior to significant expansion of the
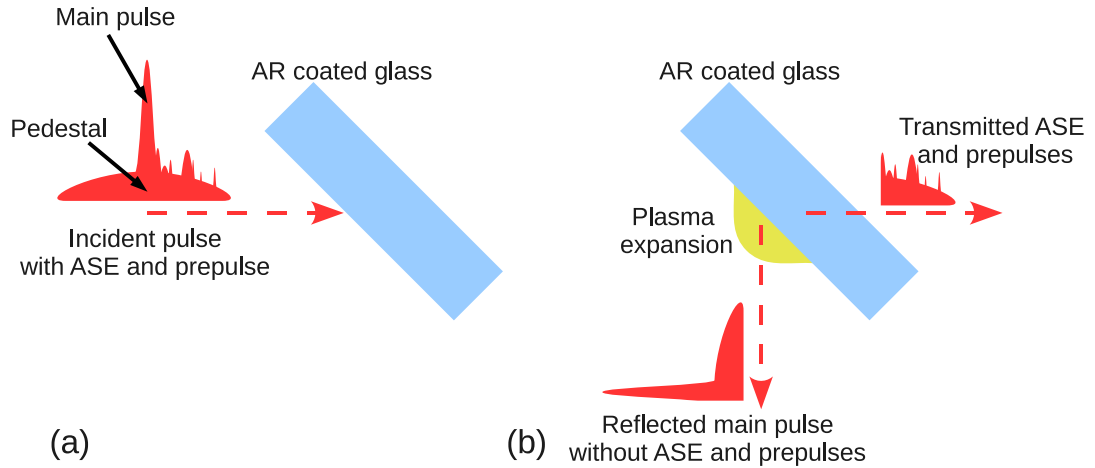
Figure 4.4: Schematic of a plasma mirror. (a) The incident laser pulse with ASE and pre-pulse is directed to the mirror. (b) The low intensity ASE pedestal and the pre-pulses are transmitted, while the main high intensity pulse is reflected as a plasma is generated on the surface of the mirror.

plasma, then the laser beam phase is retained. The improvement in the contrast is limited by the amount of light that will be transmitted through the glass prior to its ionisation, around 2% of the light is reflected in the case of AR coated glass. To improve the contrast further, multiple plasma mirrors can be used. One of the main drawback to the use of plasma mirrors is the loss of laser energy. As shown in Fig. 4.5, the reflectivity of the plasma depends on the laser intensity and pulse duration, and is found to peak between 3×10^{15} Wcm^{-2} and 3×10^{16} Wcm^{-2} at a value of 70-80% [137].

4.2.2   The VULCAN laser

The VULCAN laser is a petawatt-class laser facility at the CLF at the Rutherford Appleton Laboratory (RAL) in Oxfordshire, UK. It is capable of delivering $\sim$500 J of energy in $\sim$0.5 ps centred at a wavelength of 1.054 μm. In addition, a second beam can deliver nanosecond pulses of up to 300 J of energy in the Target Area Petawatt (TAP). A separate target station (Target Area West) is designed for experiments with dual high power picosecond CPA beams and up to 6 nanosecond 'long pulse' beams. For the TAP CPA beam, the seed of the short pulse is a Ti:sapphire oscillator capable of producing trains of 200 fs pulses with nJ energy.
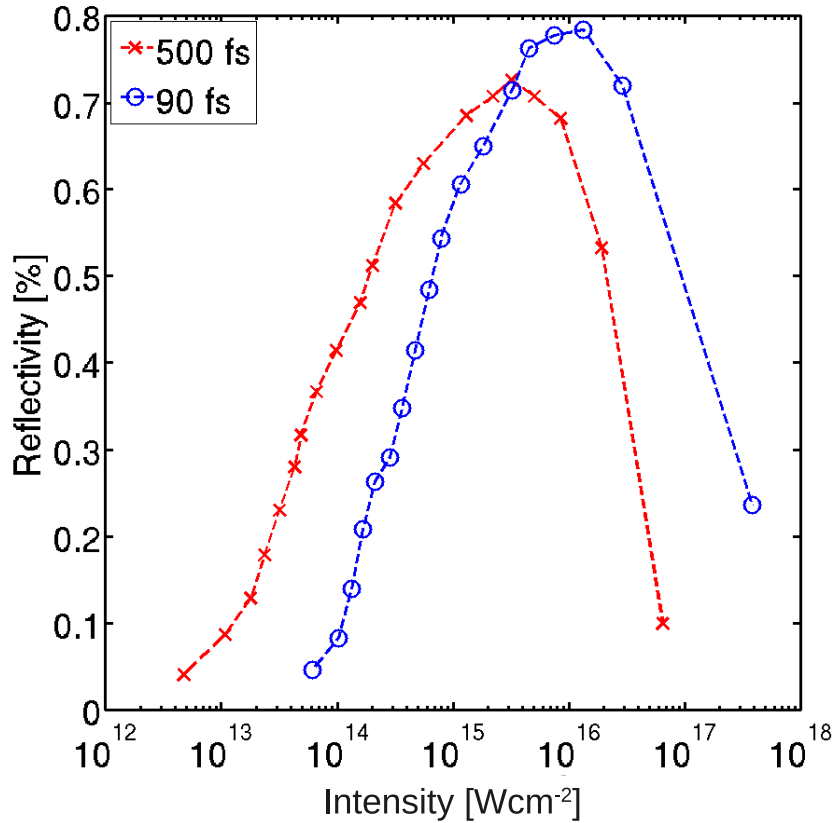
Figure 4.5: Plasma mirror reflectivity as a function of laser intensity for a 90 fs pulse (blue) and a 500 fs pulse (red) [137].

One of these pulses is selected and directed into the pre-amplification chain where the energy is increased to mJ. The pre-amplification is done by Optical Parametric Chirped Pulse Amplification (OPCPA) in which a pump pulse is used to amplify the seed pulse in a non-linear crystal. The duration of the pump pulse can be tuned to match the seed pulse thereby reducing the ASE and improving the laser contrast [141].

After pre-amplification the seed pulse is stretched and directed to the main amplification chain. It consists of neodymium doped glass (Nd:glass) rods and disks pumped using a large number of flash lamps. The rods are used as the first set of amplifiers as it is not possible to manufacture high quality rods of large dimensions. The pulse is then directed to the disk amplifiers, shown in Fig. 4.6 (a) which consists of a series of Nd:glass disks at Brewster angle to minimise reflections. During the amplification stage the diameter of the beam is expanded from a few mm to about 20 cm. Before recompression the beam passes through a

series of adaptive optics to correct the wavefront in order to improve the quality of the focussed beam.
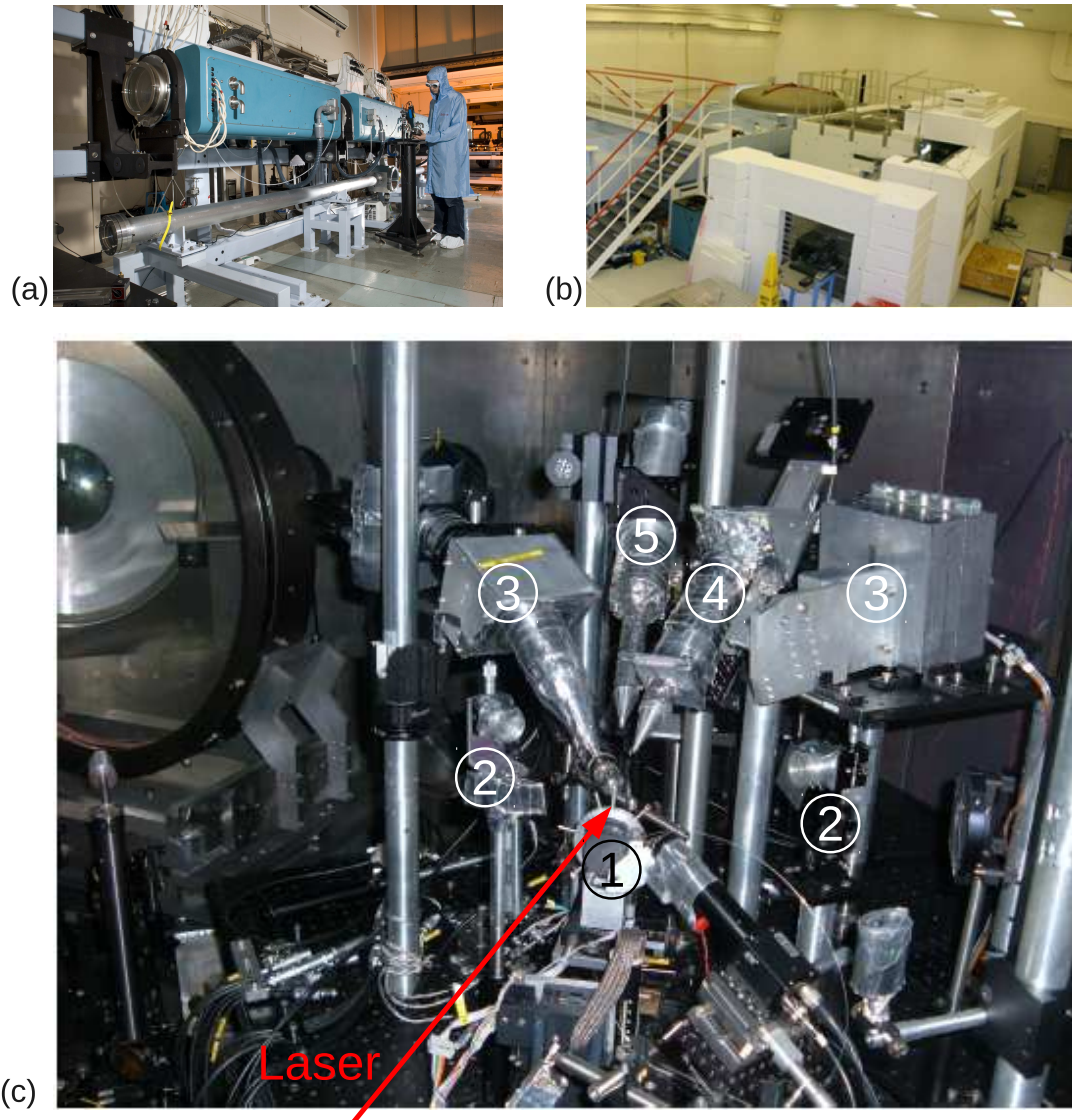
Figure 4.6: (a) One of the amplifiers of the VULCAN laser. (b) View of the Target Area Petawatt (TAP). The target chamber is enclosed in a concrete bunker. (c) Typical experimental set up; 1, target; 2, crystal for Kα imaging; 3, Kα spectrometer; 4, X-ray pinhole camera; 5, ion pinhole camera.

The beam is then brought into the target area where the pulses are recompressed and delivered into the target chamber. The compressor and target chambers are separated by a vacuum gate valve. A window is positioned on the valve to enable an alignment beam to be delivered into the chamber when it is at atmospheric pressure. The gate valve is open prior to full power shots when the

target chamber and the compressor are at similar pressure. The target chamber is approximately 2×3×5 m and contains an f/3 Off Axis Parabola (OAP) capable of focussing the beam to a spot of ∼5 μm diameter making intensities ∼1×10^{21} Wcm^{-2} achievable. The chamber is surrounded by a wall of concrete and lead, as shown in Fig. 4.6 (b) to shield the users from the radiation created by the interaction of the laser pulse with the target. Due to its dimension it is possible to enter the chamber to work on the set up. Special care must be taken to keep the chamber dust free. In addition, a number of window ports are placed on the chamber wall to enable external diagnostics to be installed. After each shot the amplifiers have to cool down for approximately 30 minutes before the laser can be fired again. It is typical to have 8-10 shots in one day. A typical experimental set up is shown in Fig. 4.6 (c).

4.2.3 The ASTRA-GEMINI laser

The ASTRA-GEMINI laser is an ultra-high intensity short pulse laser facility run by the CLF. The ASTRA laser uses multi-pass Ti:sapphire amplifiers to produce laser pulses of ∼1.5 J at a wavelength of 800 nm. The output of the ASTRA third amplifier is used as a seed pulse for the GEMINI laser. The GEMINI laser was finished in early 2008 and can deliver two beams of 15 J each with a pulse duration of 30 fs, equating to a total power of 1 PW (2×0.5 PW). The amplification in the GEMINI laser is achieved by using two multi-pass Ti:sapphire amplifiers, one for each beam. The amplification room of the GEMINI laser is shown in Fig. 4.7 (a). Each of the beams is then compressed separately and delivered to the target area.

The target area is located under the laser amplification room in a concrete bunker, as shown in Fig. 4.7 (b). The beams are delivered via apertures in the ceiling of the target area before being directed inside the target chamber via gate valves mounted on the roof of the chamber. This configuration permits access all around the target chamber giving better control of the experiment. In addition, the two-beam configuration enables to tailor the deposition of the full laser energy on the target. The contrast of one of the beams can be enhanced to ∼10^{10} by
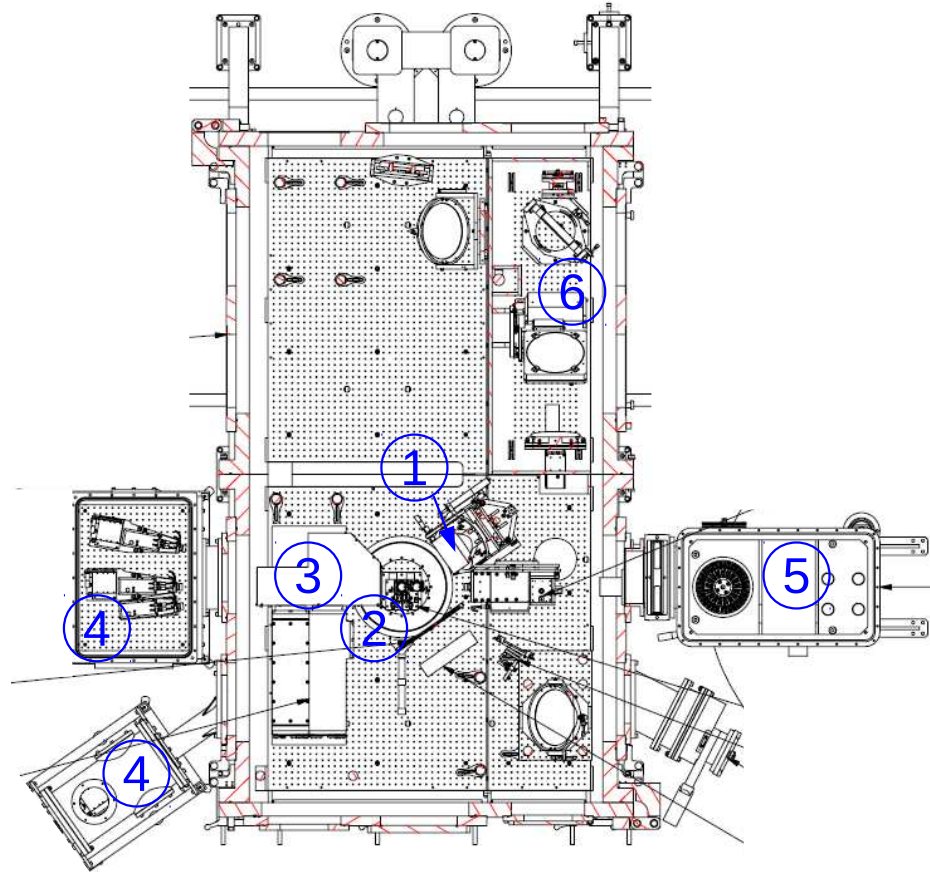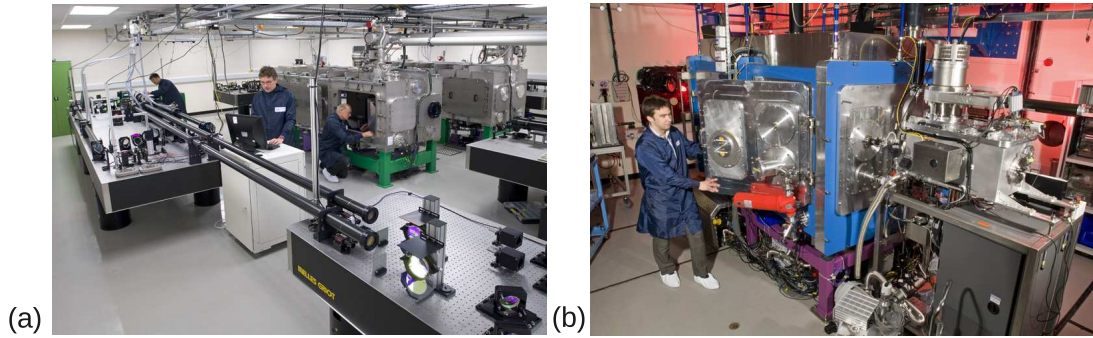
Figure 4.7: (a) The GEMINI laser amplification room. (b) The GEMINI target area. (c) Engineering drawing of a typical experimental set up; 1, focussing parabola; 2, target position; 3, proton beam spatial distribution diagnostic; 4, Thomson parabola spectrometer; 5, target inserter; 6, double plasma mirror assembly.

the use of a double plasma mirror set-up located inside the target chamber. The beam is focussed using an f/2 OAP to a 2.5 μm FWHM spot. Approximately 6 J of laser energy is deposited on the target, resulting in an intensity on target of

$\sim 10^{21}$ Wcm^{-2}.

The ASTRA-GEMINI laser is a high repetition rate laser which can be fired every 20 seconds. However, due to the procedure involved in focussing the beam, shots on solid targets are usually limited to one every few minutes. Such firing rate implies that a great number of shots can be taken during the experiments. As an indication ~ 400 shots were fired during the experiment that is reported on in chapter 5.

Using low repetition rate lasers, such as VULCAN, the targets are free standing foils mounted on stalks and placed on a wheel, which can accommodate typically 4-5 targets. To make optimal use of the high repetition rate available on GEMINI a novel target mount was manufactured. Targets mounts consist of 3×3 cm frame in which a 5×5 array of circular holes is drilled. The foil targets are then deposited on one of the surfaces of the frame. A limited number of frames can be mounted on a wheel similar to those used in VULCAN. Alternatively a target inserter can be used, which consist in a set of frames that are stored in a cartridge in a separate vacuum vessel. A robotic arm is then used to pick the frame containing the targets to shoot, and place it inside the chamber near the laser focus position on a holder. Adjustment in the position of the holder can be made from a control room adjacent to the target area to ensure an optimal focal spot on the target. A typical experimental set-up on the GEMINI laser is shown in Fig. 4.7 (c).

4.2.4   The PHELIX laser

The PHELIX laser facility is part of the GSI facility near Darmstadt, Germany. The laser system includes two separate front-ends for the generation of either long (ns) or short (ps) pulses. In the work presented in chapter 6, results obtained using the short pulses only are reported, therefore the long pulse configuration of PHELIX will not be discussed here.

The short pulse front-end generates pulses of 100 fs duration and 4 nJ energy. These pulses are then stretched and pre-amplified by a pair of Ti:sapphire amplifiers to energy ~ 30 mJ. A second pre-amplification stage occurs in three Nd:glass
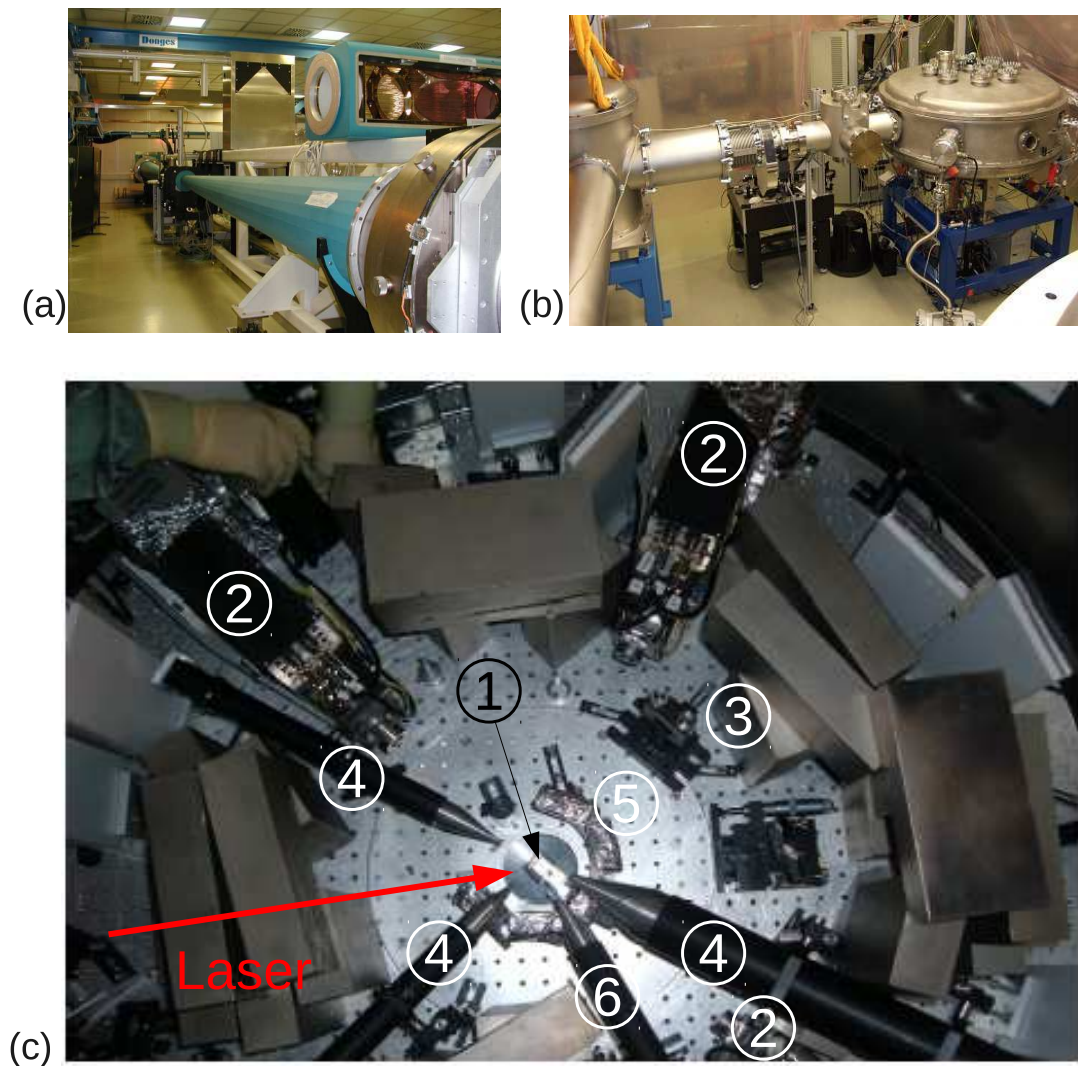
Figure 4.8: (a) The main amplification chain of the PHELIX laser. (b) View of the target chamber. (c) Typical experimental set up; 1, target; 2, Thomson parabola spectrometer; 3, crystal for Kα imaging; 4, X-ray pinhole camera; 5, RCF stacks; 6, ion pinhole camera.

amplifiers to bring the energy of the pulses to $\sim$5 J. Before entering the main amplification chain, shown in Fig. 4.8 (a), the beam is expanded to a diameter $\sim$70 mm, and is corrected for spatial aberrations using adaptive optics. The main amplification stage consists of Nd:glass amplifiers pumped with flash lamps. The amplification chain has the possibility to generate pulses with an energy of $\sim$250 J, but it is deliberately kept to $\sim$120 J to comply with restrictions on the radiation level permitted in the laser target laboratory. After amplification the pulses are recompressed to about 1 ps duration and delivered to the target chamber. It

is possible to bypass the recompression stage and send the beam in a separate target area where it can be coupled with the heavy ion linear accelerator present in the GSI facility.

The target chamber, shown in Fig. 4.8 (b), in the PHELIX facility is located in the same room as the laser amplifiers and consists of a 1.5 m radius cylindrical vessel. Due to its location in the laser amplifier room it is not possible to build the necessary radiation shielding outside of the chamber as in the other laser facilities and as a consequence all the shielding material has to be placed inside the chamber, reducing the space available for diagnostics. The beam is focussed to the center of the chamber using an f/6.7 OAP, situated outside of the chamber, to a spot of $\sim$15 μm diameter. Approximately 50 J of energy is delivered by the laser onto target, making intensities of $\sim$5$\times$10^{19} Wcm^{-2} accessible. A typical experimental set-up is shown in Fig. 4.8 (c).

4.3   Laser plasma interaction diagnostics

A wide variety of techniques are used to diagnose the interaction of the laser pulse with the target. In the following section the methods relevant to the work contained in this thesis are presented.

4.3.1   Thomson parabola ion spectrometer

Ion beams generated by the interaction of an intense laser pulse with a foil target can contain a large variety of ion species and charge states. It is necessary to be able to establish the composition of the ion beam in order to fully understand the mechanisms of ion acceleration. This can be achieved by using a simple charge-to-mass spectrometer called a Thomson parabola spectrometer. It was first used in 1913 by Thomson [142] to identify the isotopes of neon. This simple spectrometer relies on the combination of the deflections induced by parallel electric and magnetic fields on the trajectory of a charged particle. A schematic of a Thomson parabola ion spectrometer is presented in Fig. 4.9.

The deflections of the ions in the fields can be easily calculated using the
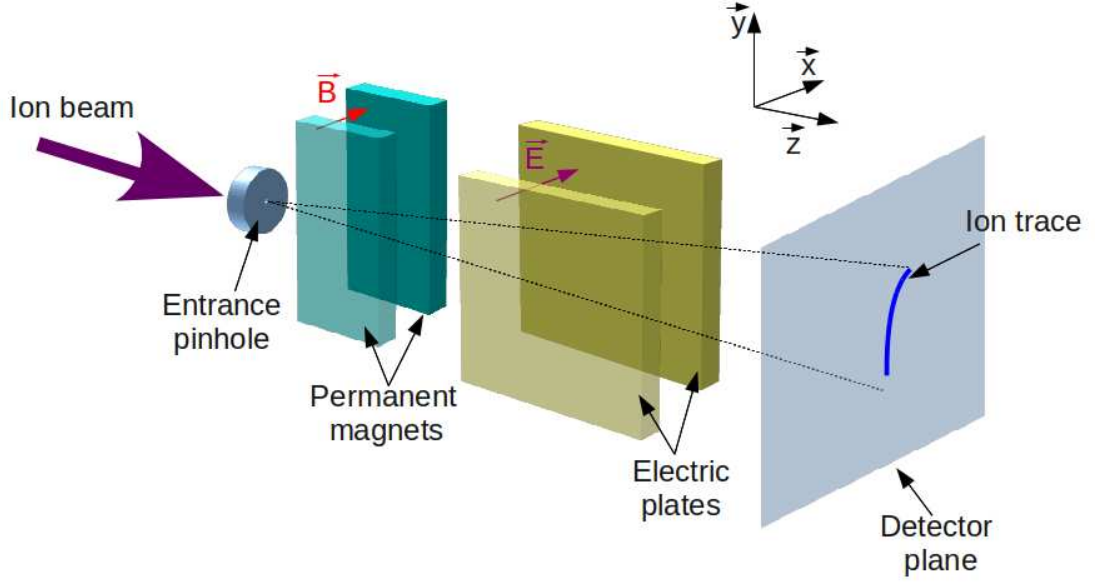
Figure 4.9: Schematic of a Thomson parabola spectrometer. A portion of the incident ion beam is selected by a pinhole and deflected in a succession of magnetic and electric fields. The ion species are separated according to their charge to mass ratio, and can be detected using various methods as described in the main text.

equation of motion of a charged particle in a combination of electric and magnetic fields. If we consider the fields to be constant along the directions $\vec{x}$ defined in Fig. 4.9 and the ions propagating in the $\vec{z}$ direction, the displacement caused by each field at the position of the detector is:

$$D_E = \frac{qEL_E}{mv_z^2} \left(\frac{1}{2} L_E + d_E \right) \tag{4.1}$$

$$D_B = \frac{qBL_B}{mv_z} \left(\frac{1}{2} L_B + d_B \right) \tag{4.2}$$

The different parameters of Eq. (4.1 & 4.2) are defined in Table 4.1.

Assuming that the electric deflection D_E and the magnetic deflection D_B are along the $\vec{x}$ and $\vec{y}$ axis, respectively, the equation of the trace recorded on the detector for a given ion species, obtained by combining Eq. (4.1 & 4.2), is:

$$y = \frac{EC_E m}{q \left(BC_B \right)^2} x^2 \tag{4.3}$$

with $C_E = L_E \left(L_E/2 + d_E \right)$ and $C_B = L_B \left(L_B/2 + d_B \right)$.

Variable	Description	Typical value
E	Electric field strength	$150\ \mathrm{Vm^{-1}}$
B	Magnetic field strength	0.5 T
L_E	Electric plate length	100 mm
L_B	Magnet length	50 mm
d_E	End of electrode to detector	50 mm
d_B	End of magnets to detector	200 mm

Table 4.1: Principal parameters of a Thomson parabola spectrometer with typical values use for the measurements presented in chapter 5.

As seen from Eq. (4.3) the trace recorded on the detector for a given species with a specific q/m ratio will be a parabola. From Eq. (4.1 & 4.2) it is also possible to see that the more energetic particle will be the less deflected. Example of recorded parabolas are shown in Fig. 4.10. An origin point is usually visible on the detector. It is the result of a combination of the X-ray emission coming from the target and of neutral particles (ion recombination resulting in fast neutrals) travelling through the spectrometer. It effectively represents the reference point of 'zero' deflection.

As shown in Fig. 4.10, multiple species of ions are accelerated. They are identified by finding the q/m ratio corresponding to the parabola that fits the experimental track for a given set of spectrometer parameters. The maximum energy of a given species is easily obtained by measuring the distance from the origin point to the bottom limit of the parabola. An energy spectrum can also be obtained by integrating the signal along the length of the track. The lowest energy measurable mainly depends on the separation of the electrodes, as the ions are deflected towards one of the electrodes, the further apart the electrodes are, the largest the energy range covered is. The energy range can be increase by angling one of the electrodes as described by Carroll *et al.* [143]. As can be seen in Fig. 4.10, the high energy part of the tracks tend to merge together when multiple ion species are detected, therefore reducing the energy resolution of the spectrometer. This can be avoided by increasing the electric or magnetic deflections or by placing the detector further away from the spectrometer to increase the dispersion of the ions.

It is important to identify the sources of systematic uncertainties and errors
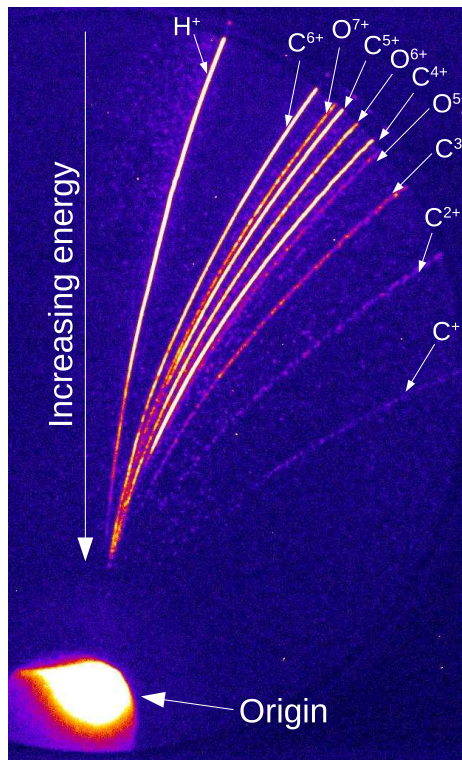
Figure 4.10: Example of parabolas obtained experimentally. Each track corresponds to a given q/m ion species.

made when using a Thomson parabola ion spectrometer. The primary source of errors comes from the presence of electric and magnetic fringe fields which affect the deflection of the ions. These errors can be minimised if the electric and magnetic field are accurately measured. A second source of errors results from the use of a pinhole at the entrance of the spectrometer. The distance from the ion source to the spectrometer entrance and the diameter of the pinhole defines the solid angle over which the ion emission is sampled. The larger the solid angle, the larger the width of the ion track on the detector. This contributes to the uncertainty in the measurements of the maximum ion energy by reducing the energy resolution of the spectrometer. These uncertainties can be reduced if the diameter of the pinhole is reduced, however, this can reduce the ion flux below the detector sensitivity. Therefore a compromise must be found between the ion flux and the spectrometer energy resolution, on a typical experiment using the VULCAN laser, pinholes of diameters between 50 μm and 100 μm are used.

4.3.2 Stacked dosimetry film detector

Valuable information on the interaction of the laser foil with the target can be obtained from the spatial intensity distribution of the proton beam. This is typically measured using stacked layers of dosimetry film. The dosimetry film usually used is RadioChromic Film (RCF), composed of an active layer (organic dye sensitive to dose) placed on a clear polyester substrate, the active layer is protected by a thin gelatin layer, as seen in Fig. 4.12 (c). The RCF is initially transparent and turns blue when exposed to dose, thus making it a self-developing film. The optical density of the exposed film depends on the dose deposited in the active layer. The higher the dose, the higher the optical density.

As the ions penetrate inside a material they will deposit most of their energy at a given depth, the Bragg peak,as shown in Fig. 4.11. Clever use of this property
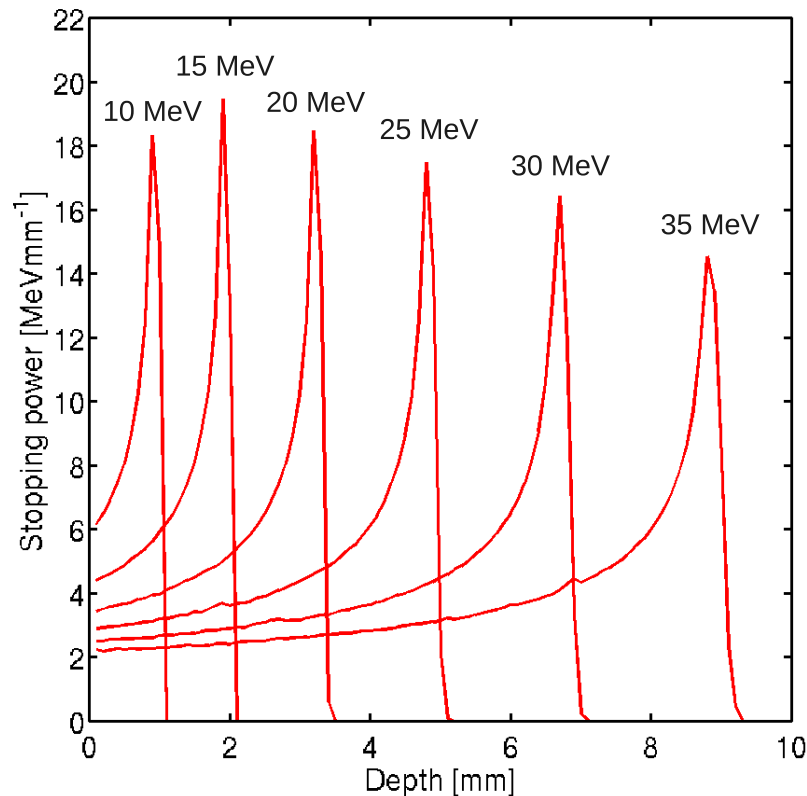
Figure 4.11: Stopping curves of protons of different energy in Mylar.

enables the energy spectrum of the proton beam to be measured using stacked layers of RCF. As the proton beam travels through the stack, protons deposit their

dose in a given layer corresponding to the maximum depth they can penetrate to. Therefore each RCF layer corresponds to a specific energy component of the whole beam. While it would give a better energy resolution, it is not typical to build a stack made solely of RCF layers for practical and financial reasons. A typical RCF stack, as shown in Fig. 4.12 (a), is made of a layers of RCF film alternating with low Z filters of varying thickness. The further the RCF film is placed in the stack the more energetic the protons detected are. A thin layer of Al is placed in front of the stack to stop low energy protons and heavy ions. It also shields the stack from the debris coming from the target. An example of exposed RCF film is shown in Fig. 4.12 (b).
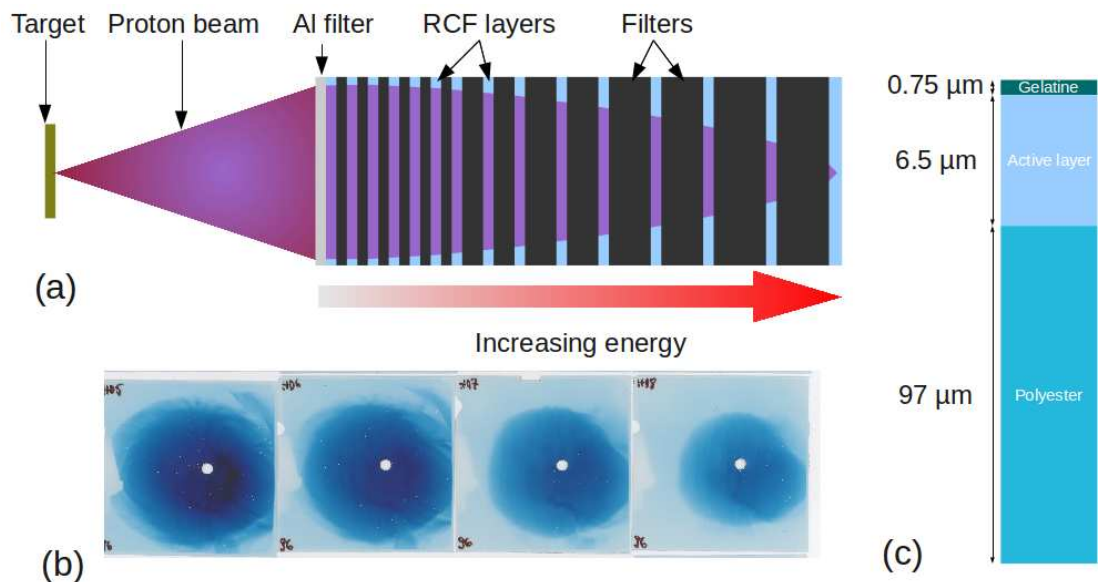
Figure 4.12: The stacked dosimetry film (RCF) detector. (a) Typical construction of a stack showing the different layers used. (b) Examples of RCF exposed to proton emission. (c) Composition of the RCF film (HD type).

To identify the energy corresponding to a specific layer of RCF it is necessary to model the propagation of the proton beam inside the stack using Monte-Carlo simulation of proton stopping. This can be done with the SRIM software package [144]. The energy spectrum of the proton beam can be reconstructed from the RCF data. This requires the determination of the number of protons stopped in each layer. As the optical density of an exposed RCF layer directly correlates with the deposited dose, it is possible to calibrate the film by exposing it to a known

dose. For example from a conventional accelerator delivering a well characterised beam. The films exposed to protons during the experiment are then scanned at high resolution, and the dose deposited on a given area is determined using the calibration. It is possible to calculate the total energy $\mathcal{E}_{tot}$ deposited in a given layer using the following formula:

$$\mathcal{E}_{tot} = d_L \rho_L \sum_{i=1}^{N} (D_i A_i) \tag{4.4}$$

where d_L is the sensitive layer thickness, ρ_L is the layer density and D_i and A_i is the dose and area of the pixel i respectively. The corresponding number of protons per MeV (N_{proton}) stopped in the layer can be estimated using Eq. (4.5) assuming that the protons stopped in the layer deposited all their energy in that layer and neglect the contribution from the higher energy protons passing through.

$$N_{proton} = \frac{\mathcal{E}_{tot}}{\mathcal{E}_{Bp}\delta\mathcal{E}} \tag{4.5}$$

where $\mathcal{E}_{Bp}$ is the Bragg peak energy at the centre of the considered RCF layer and $\delta\mathcal{E}$ is the energy width of the layer (the difference in energy between the proton stopped at the front of the active layer and the one stopped at the back).

The self-developing nature of RCF means it is possible to have almost instant information on the proton beam. On the other hand it is a low repetition rate diagnostic and is not suitable for experiments carried out on facilities like the ASTRA-GEMINI laser.

4.3.3 K shell emission

The Kα emission can provide important information on the interaction of laser pulses with matter. For atoms to produce Kα emission, an electron from the L shell has to transit to the K shell while radiating a photon. In the context of laser solid interaction this can occur when a hot electron collides with a K shell bound electron, leaving one orbital of the K shell unoccupied. This process emits an X-ray photon as shown schematically in Fig. 4.13.

Bound to free transition

Fast electron

L

K_α photon

K
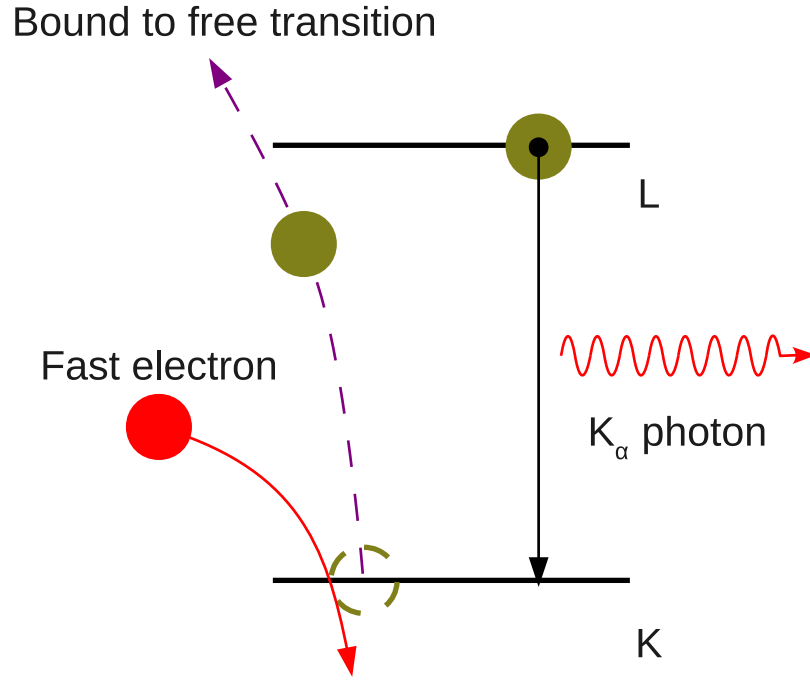
Figure 4.13: Summary of the Kα transition. An electron from the K shell is ejected from the atom by the collision with a fast electron. An electron from the L shell transits to the K shell emitting a Kα photon.

The Kα emission can be imaged using a spherically bent Bragg crystal, typically arranged to image the photon with energy corresponding to the Kα transition. To select the appropriate photons, the angle of incidence of the emission on the crystal must be set to satisfy the Bragg condition:

$$2d \sin\theta = n\lambda_{K\alpha} \tag{4.6}$$

where d is the distance between the planes of the crystal lattice, θ is the angle of incidence of the photon with the lattice plane, n is an integer representing the diffraction order and $\lambda_{K\alpha}$ is the wavelength of the Kα photon. Assuming that the crystal is aligned such that the Bragg condition is satisfied at its centre, the bandwidth of the crystal can be estimated by calculating the wavelength of the photon that will be diffracted at the edges of the crystal. In the measurements presented in chapter 6, the Kα emission of Cu ($\lambda_{K\alpha} = 1.541$ Å and $E_{K\alpha} = 8048$ eV) is measured with a bandwidth $\Delta E \approx 6$ eV.

Whereas a spherically bent crystal is used to make spatially resolved mea-

surements of the Kα emission [145–147], a flat crystal is used to disperse the X-ray signal in a spectrometer arrangement. The ratio of line intensity corresponding to different line transitions are used to estimate the bulk temperature of the target [148].

4.3.4   Detectors

The various detection techniques used to record the different particle and radiation emission characterise in sections 4.3.1 & 4.3.3 are discussed below.

Micro-channel plates

Micro-Channel Plates (MCP) are sensitive to all types of ionising particles and radiation. It consists of a dense hexagonal array of glass capillaries fused together and sliced to form a thin plate. The glass capillaries, or micro-channels, have a diameter of approximately 10 μm and are at an angle with the surface of the plate, $\sim 8°$. A strong potential difference, ~ 10 kV, is applied across the plate so each channel can act as a separate electron multiplier. The multiplication is triggered when a particle or photon hits the wall of the channel creating more than one electron. These secondary electrons are then accelerated down the channel before they hit the channel wall generating more electrons, thus resulting in an avalanche of electrons that amplifies the original signal by $\sim 10^4$. The amplified electron signal is then converted to photons using a phosphor screen, enabling an image of the signal to be recorded using a CCD camera. The channels are at an angle with the surface of the plate in order to maximise the number of particles or photons triggering an electron avalanche.

To increase the signal amplification it is possible to increase the voltage applied to the plate, but this is limited by saturation effects occurring in the channels. Another possibility is to use more than one MCP plate in a chevron configuration. This configuration consists of at least two MCPs placed one after the other and rotated such that the channels of each plates are at a 90° angle with respect to each other. In this configuration the electron avalanche in the second MCP is triggered by the electrons coming out of the first one. The spatial resolution of

the MCP is limited by the size of the channels and the distance between them
($\sim$10 μm). Fig. 4.14 shows a schematic of a micro-channel plate.
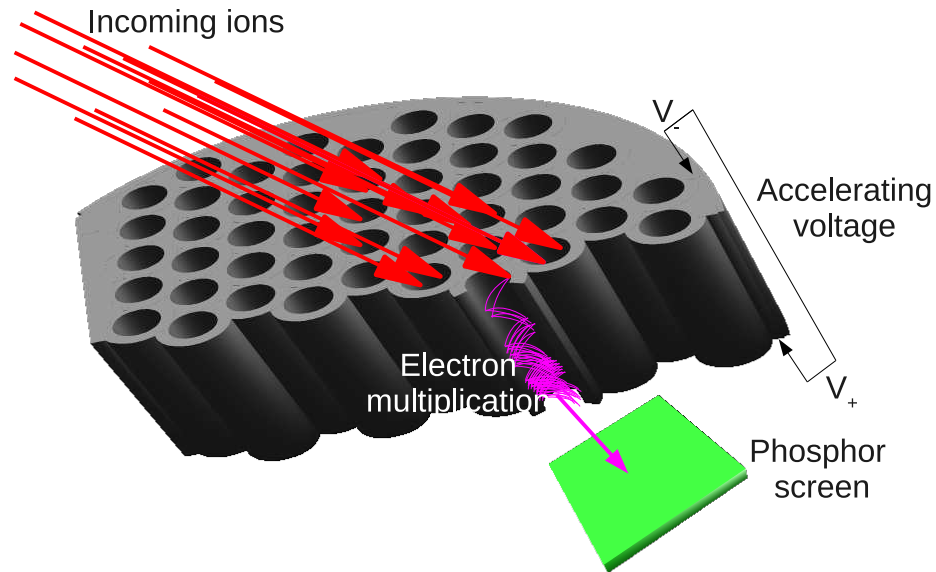
Figure 4.14: Schematic of a micro-channel plate.

MCPs were used in the work presented in chapter 5, to detect ion traces in the
dispersion plane of a Thomson parabola spectrometer. The combination of the
MCP and the CCD camera used to record the signal had to be calibrated to enable
measurements of the number of ions detected. To do this, slotted CR39 track
detectors were placed in front of the MCP to record the trace on both detectors
simultaneously. The CR39 being an absolutely calibrated detector, it is possible
to correlate the pixel count recorded by the CCD camera to the corresponding
number of ions at a given energy [149]. The use of MCP detectors in combination
with Thomson spectrometers is ideal for high repetition rate laser facilities.

Imaging plates

Fujifilm Imaging Plates (IPs) are a type of reusable film sensitive to X-ray pho-
tons and charged particles and were originally developed for medical purposes.
They consist of an active layer embedded in a plastic medium. Crystals of eu-

ropium dopped barium fluorohalide phosphor ($BaF(Br,I):Eu^{2+}$) make up the active layer. When a charged particle or an X-ray photon is absorbed by the active layer, electrons from the Eu^{2+} ions are transferred to a metastable state. The metastable states will decay spontaneously at a rate depending on the exact chemical composition of the IPs, or if the plate is illuminated by a laser at a visible wavelength. When the decay occurs the Eu^{2+} ions emits a photon at 400 nm via photo-stimulated luminescence (PSL). To retrieve the data stored in the IPs they are locally illuminated with the appropriate wavelength light and the PSL photons are detected by a photomultiplier. As the metastable states decays the signal is lost. Therefore it is possible to completely erase the IPs by scanning them multiple times or by exposing them to bright white light [150].

IPs are sensitive to a wide range of emission (X-ray, electrons, ions) and therefore they can be used in a number of diagnostics, such as a Kα imager or a Thomson parabola ion spectrometer. It can also be a disadvantage as they will record all these emissions simultaneously which can make the identification of a particular signal an arduous task. The spontaneous loss of signal inherent to the IP operation process means that they have to be scanned relatively soon after being exposed to the signal, typically within a few hours.

4.4   Simulation tools

Numerical simulations form an important part of the investigations into laser solid interactions, as they can provide useful insight into the physical processes investigated experimentally. The accuracy of such codes highly depends on the number of assumption made and on the computational resources available. The advent of parallel computing in the early 1990's has made numerical simulation much more reliable and accessible.

Many types of simulation codes are available with different methods of addressing the physics. There are three main categories:

- **Microscopic codes**: These track each particle (electron or ion) individually. These codes are the most detailed, but they are strongly limited in the

number of particles they can consider, ($\sim 10^6$). Therefore microscopic codes are not suitable for large collective effects such as ion acceleration which involve approximately 10^{14} particles.

- **Kinetic codes**: These consider the plasma as a collection of statistical particles interacting with the various different fields. They offer a good compromise between the level of detail and the calculation time required, but are also limited by the number of particles and the duration of the simulated interaction.

- **Fluid codes**: These assume that the different components of the plasma behave as fluids. Therefore they achieve a lower level of detail compared to the other types of code, but enable the interaction to be simulated over long distances and time.

In the following subsection, the types of codes that were used to support the experimental results presented in this thesis are discussed.

4.4.1 PIC codes

Particle In Cell (PIC) codes use the kinetic approach to simulate the interaction of the laser pulse with the target. They consider the plasma as a collection of macro-particles interacting with fields calculated on a spatial grid. The basic calculation routine of a PIC code is shown in Fig. 4.15.

The particle distribution is first defined by the user. The value of the current and charge density distribution is then calculated at every grid point using a weighted function. The electric and magnetic fields can then be calculated at each grid point by solving Maxwell's equations. The value of the fields at the particle position is calculated using the same weight function as previously, and the particle position and velocity are updated by solving Lorentz' equation. This procedure is repeated for each successive time step until the simulation is complete. Variables of interest, such as the particle position and velocity or the electric and magnetic fields, are saved in separate output files at each time step.
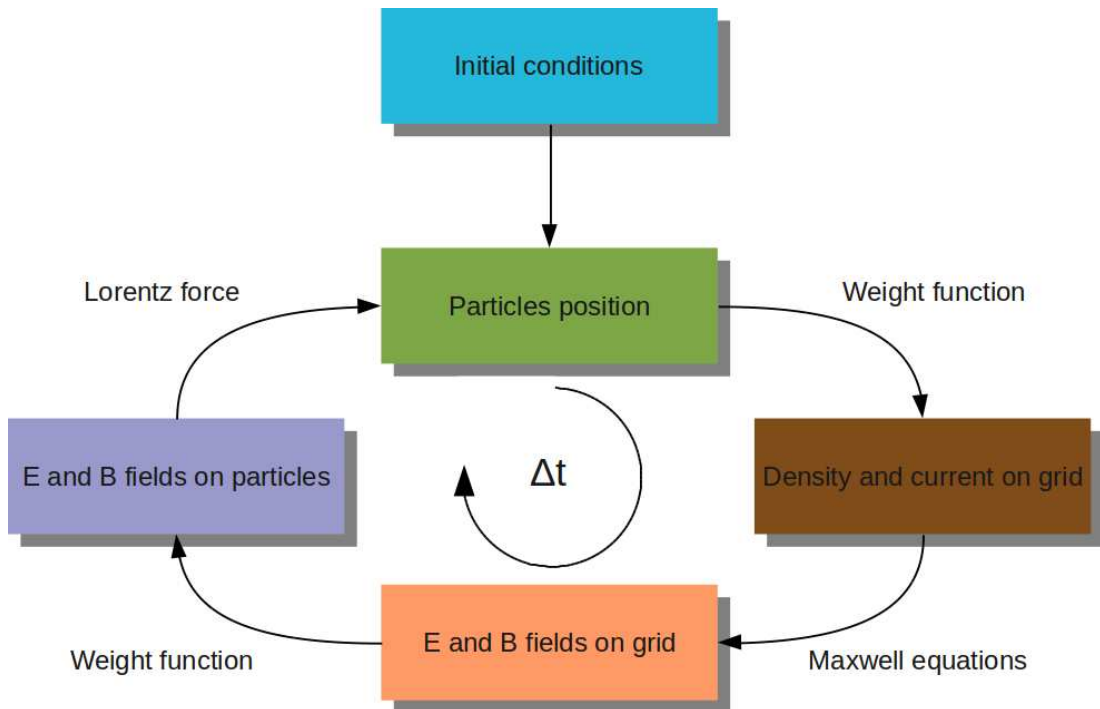
Figure 4.15: Schematic diagram showing the steps involved in a PIC simulation, as described in the main text.

The parameters of the simulations are usually provided as inputs to the main code via a separate input file containing:

- spatial parameters, such as the simulation box size and cell size;

- temporal parameters, such as the time step and the simulation duration;

- laser parameters, such as intensity and pulse duration;

- the initial plasma distribution, such as the number of particles, their charge and mass, their initial velocity and their spatial distribution.

PIC simulations model the physical processes closest to reality as they make fewer approximations than the other types of codes mentioned. As with any type of simulation it is of paramount importance to avoid numerical aberrations. This can be achieved by introducing implicit time steps. In addition, the time step has to resolve the plasma frequency and the cell size have to be smaller than the Debye length. The main drawbacks of the PIC approach is the difficulty to include collisions, ionisation or material properties. It is also not feasible to simulate solid

87

material in a reasonable calculation time as the number of particles required is too high. Constraints on the time step and the grid size limit the duration of the simulation and the simulation box size.

4.4.2   Hybrid-PIC codes

A clever combination of the kinetic and fluid approaches can be used as a good compromise between a full kinetic and a full fluid approach. In the hybrid-PIC approach the fast electron population is described by a kinetic model interacting with a background plasma considered as a fluid. The introduction of a fluid background plasma enables inclusion of material properties such as resistivity. The fast electron and the background plasma can interact with each other via the generation of fields. This makes the use of hybrid-PIC codes particularly relevant to the investigation of electron transport, as discussed in chapter 7.

Chapter 5

Ion acceleration by ultra-high intensity, ultra-high contrast laser irradiation of thin foil targets

5.1 Introduction

In the last decade, laser driven acceleration of ions to multi-MeV energies has been demonstrated. Despite their many advantages over conventional ion beams, these beams need further optimisation before the proposed applications can be fully developed. The maximum proton energy achieved to date is of the order of 70 MeV, while proton oncology requires energy of around 200 MeV. The ion beams produced today are mostly generated via the TNSA acceleration mechanism, described in chapter 3, which results in a broad energy spectrum, while many applications require mono- or quasi mono-energetic ion beams.

The need for improvement of laser-accelerated ion beams has driven a large research effort and recently great improvements in the laser pulse intensity contrast has enabled the use of ultra-thin target foils, in the tens of nanometre range. It has been shown that efficient ion acceleration can be achieved from nanome-

tre scale thickness targets irradiated by ultra-short ($\sim$40 fs) laser pulses with intensities $\simeq 1 \times 10^{19}$ Wcm^{-2} [65]. It has been reported that the maximum ion energy increases with decreasing target thickness [151]. The main issue when using ultra-thin targets is the laser intensity contrast. If the contrast is too low, then the laser pre-pulses and the laser pedestal can be intense enough to launch a shock wave into the target that will disrupt the ion acceleration at the rear surface in the best case or completely destroy the target before ion acceleration can occur in the worst. Ultra-thin targets also enable investigation of new ion acceleration regimes with higher laser-to-ion energy conversion efficiency or narrower energy spectrum. These new regimes include Radiation Pressure Acceleration (RPA) or the Coulomb explosion.

In this chapter an experimental investigation of TNSA accelerated carbon ions using ultra-high intensity contrast (10^{10}), ultra-short (50 fs) and ultra-intense (7×10^{20} Wcm^{-2}) laser pulses is reported. This is the first ion acceleration experiment with ultra-short pulses at an intensity comparable with large-scale picosecond laser systems such as the VULCAN laser. The study focusses on the acceleration of carbon ions. Target thickness and composition effects are investigated experimentally and analytically. Acceleration for normal and oblique laser incidence angles is discussed both experimentally and numerically with the help of 1D boosted PIC simulations. The work presented in this chapter has been published in Ref. [152].

5.2   Experiment

The experiment was carried out using the ASTRA-GEMINI laser at the CLF, described in chapter 4. The laser delivered p-polarised pulses of 50 fs duration with energy up to 12 J, at a wavelength of 800 nm. A double plasma mirror arrangement was used to enhance the laser intensity contrast from 10^7 to $\sim 10^{10}$. The energy loss due to the double plasma mirror was determined to be around 52%, giving an energy on target $\sim$5.8 J. The laser beam was re-collimated after the plasma mirrors and focused using an f/2 off axis parabola to a 2.5 μm FWHM

spot containing 35% of the laser energy, resulting in an intensity on target of 7×10^{20} Wcm^{-2}. Targets were irradiated at two different laser incident angles, 35° and 0° with respect to the target normal. Hereafter the 0° case is referred as the normal incidence and the 35° case is referred to as the oblique incidence case. To achieve this the targets were simply rotated in their mount and a Thomson parabola ion spectrometer set up a both angles, as shown in Fig. 5.1.
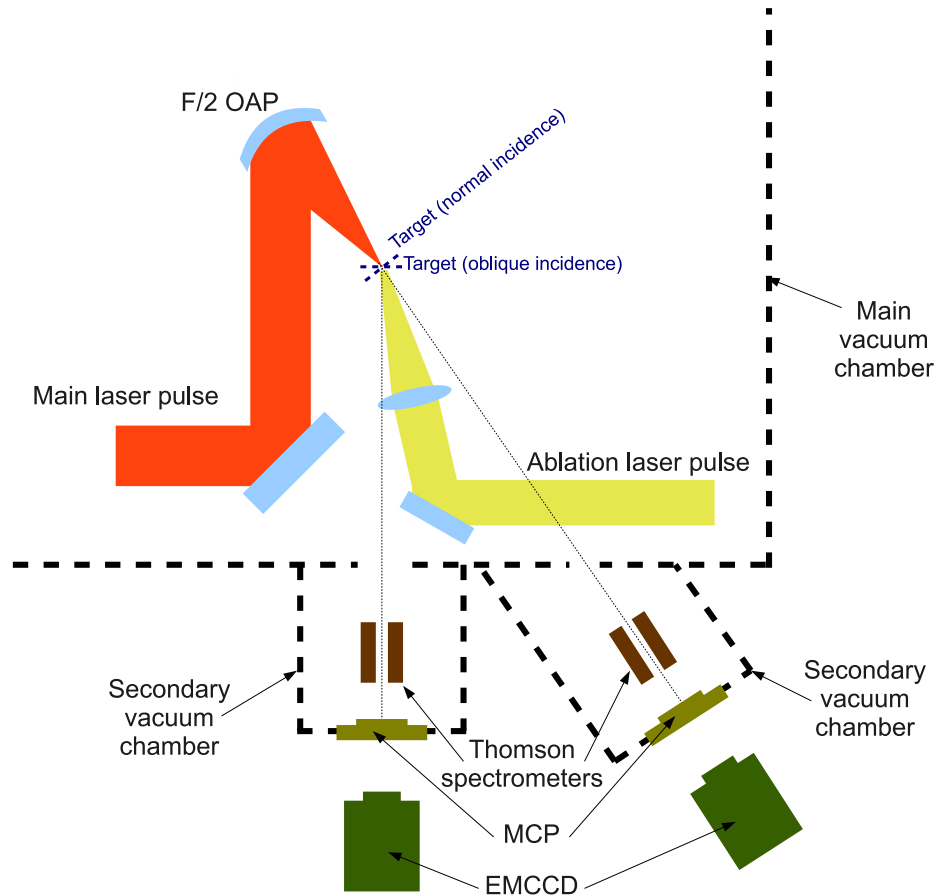
Figure 5.1: Schematic of the experimental setup.

In addition, a train of low intensity pulses were used for ablation to selectively clean the target rear surface. The pulses were delivered by a Minilite I laser manufactured by Continuum. The laser was placed on top of the main vacuum chamber and the beam was brought down inside the chamber through a silicate window. The Minilite I is a Nd:YAG Q-switched laser delivering pulses of approximately 5 ns duration at a wavelength of 532 nm (frequency doubled). The repetition rate of the laser can be varied between 1 and 10 Hz, with each pulse containing ∼7

mJ of energy. The beam was focussed onto the surface of the target to a spot of radius $\sim$320 μm, resulting in a fluence on target of $\sim$3 Jcm^{-2}. A repetition rate of 10 Hz was selected, and the laser was triggered 1 s prior to the main intensity laser pulse.

Targets of thickness ranging between 50 nm and 10 μm were irradiated during the experiment. The target material was varied to determine the optimum composition for carbon ion acceleration. These were C, polypropylene (C$_3$H$_6$, hereafter referred to as CH), mylar (C$_{10}$H$_{10}$O$_4$, hereafter referred to as CHO), Al, Au and layered Au+CH targets. In the case of the Al and Au targets the carbon ions originate from the contaminant layers on the target rear surface.

The ion emission was dispersed using two Thomson parabola ion spectrometers, as described in chapter 4, placed in separate vacuum chambers connected to the main chamber. Their position was fixed and each of them was placed in the normal direction for a given laser incidence angle as shown in Fig. 5.1. A microchannel plate (MCP) detector, described in chapter 4, was used to detect the ion emission tracks from both spectrometers. The signal of the MCP was captured using an intensified Andor Electron Multiplying CCD (EMCCD) camera. The MCP-EMCCD arrangement was absolutely calibrated using slotted CR-39 track detector placed in front of the MCP on selected shots [149].

5.3 Effects of varying the target thickness on ion acceleration

5.3.1 Experimental results

The scaling of the maximum energy for C^{6+} ions with target thickness was investigated. Al, Au and CHO targets with thickness ranging from 10 μm to 100 nm were used. The experimental findings are shown in Fig. 5.2 for both incidence angles. To reflect the large number of shots taken during the experiment, each point in Fig. 5.2 represents the average (over 3-4 shots) maximum ion energy observed for one target type at a given thickness. The standard deviation in energy

is indicated by the error bars.

It can be seen from Fig. 5.2 that, independently of target material, the maximum ion energy is increasing with decreasing target thickness. The measured scaling of the maximum ion energy is very similar to that reported previously by Neely *et al.* [151] with lower intensity laser pulses. They reported that as the target thickness is decreased from $\sim$10 μm down to 100 nm the maximum proton energy increases by a factor $\sim$2 (from 2 MeV to 4 MeV). In the present case it is observed that the maximum C^{6+} ion energy is increased by a factor 2 (from 40 MeV up to 80 MeV) for the same target thickness range. This enhancement in the maximum ion energy is explained by the refluxing, of the laser generated, hot electron population [81, 82]. For thin enough targets, $L \ll c\tau_L/2$, where L is the target thickness and τ_L is the laser pulse duration, the refluxing electrons will enhance the duration of the TNSA field developing at the rear of the target, and thereby increase the maximum ion energy. Here $c\tau_L/2$= 7.5 μm.

5.3.2 Analytical modelling

Next, two analytical models are applied and the predicted maximum ion energies are compared to the experimental data. The models used are described by Andreev *et al.* [153, 154] and Schreiber *et al.* [86]. The results obtained from the models are plotted alongside the experimental data in Fig. 5.2 as solid lines.

The model introduced by Andreev *et al.* [153, 154] predicts the maximum ion energy by solving the Poisson equation to determine the TNSA field and the equation of motion of the ion front. In the model, targets consists of two layers, the bulk and a thin contaminant layer. The overall density profile of the target is assumed to be rectangular, in agreement with the interaction of a ultra-high contrast laser pulse with a solid foil. The model has been validated for a laser incidence of 45° using experimental and numerical data. It should be noted that this model uses cgs units. The maximum ion energy is estimated as:

$$\mathcal{E}_{max} \approx \frac{2.4 q e E_{thin} \lambda_D}{\sqrt{1 + (L/\lambda_D)^2}} + \frac{2 q e E_{thick} \lambda_D}{\sqrt{1 + (\lambda_D/L)^2}} \qquad (5.1)$$
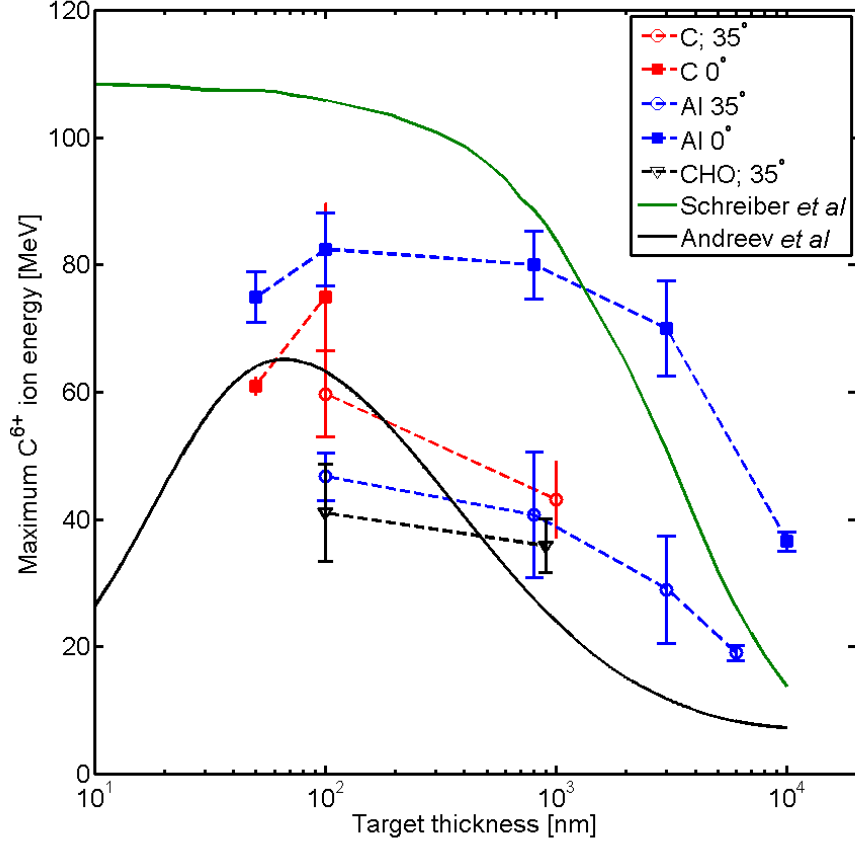
Figure 5.2: Variation of the average C^{6+} maximum energy as a function of target thickness for different target materials. For laser incidence of 0° and 35°. The solid lines correspond to predictions using the analytical models of Schreiber *et al.* [86] (green) and Andreev *et al.* [153] (black).

where L is the target thickness and λ_D is the electron Debye length. The fast electron temperature T_e is assumed to be a function of the target thickness and the laser absorption coefficient, and is obtained using:

$$T_e \approx \frac{\eta(L) I_L \tau_L}{q n_{ib} L} \qquad (5.2)$$

where $\eta(L)$ is the laser absorption coefficient depending on the target thickness, I_L is the laser intensity, and n_{ib} is the target bulk ion density. The laser absorption coefficient is given by:

$$\eta(L) \approx \frac{0.5 \ln(1 + L/l_s)}{1 + \ln(1 + L/l_s)} \qquad (5.3)$$

where l_s is the plasma skin depth. In Eq. 5.1, E_{thin} and E_{thick} are the electric field

at the ion front associated with very thin and thick targets respectively. They are given by:

$$E_{thin} = 2\pi e(q_b n_{ib} L_b + q_c n_{ic} L_c) \tag{5.4}$$

and

$$E_{thick} = \frac{q_b n_{ib}\sqrt{2}}{n_{e0}3^{3/4}}\sqrt{4\pi q_b n_{ib} T_{e0}} + 2\pi e q_c n_{ic} L_c \tag{5.5}$$

The subscripts b and c refers to the target bulk and contaminant layer respectively and n_i the solid ion density. In this work the calculations are made for a carbon target with a constant 5 nm thick hydrogen contaminant layer. The thickness of the bulk of the target is varied to reproduce the different target thickness investigated. The results are shown in Fig. 5.2 as a black solid line.

The second model used is the model by Schreiber *et al.* [86], presented in detail in chapter 2. It is based on a surface charge being set up by the fast electrons on the rear surface. The maximum ion energy $\mathcal{E}_{max}$ is then obtained using the following formula:

$$\frac{\tau_L}{\tau_0} = X\left[1 + \frac{1}{2(1-X^2)}\right] + \frac{1}{4}\ln\frac{1+X}{1-X} \tag{5.6}$$

$$\text{where } X = \sqrt{\frac{\mathcal{E}_{max}}{\mathcal{E}_{\infty}}} \tag{5.7}$$

The results are presented in Fig. 5.2 as solid green lines.

Both models predict a general increase in the maximum ion energy with decreasing target thickness in good qualitative agreement with the experimental findings. The model proposed by Schreiber *et al.* [86] predicts a saturation of the maximum ion energy for targets thinner than 100 nm. An optimum thickness around 80 nm is predicted by the model by Andreev *et al.* [153]. This is higher than the 20 nm previously predicted by Esirkepov *et al.* [155] for similar laser conditions. A slight decrease in C^{6+} ion maximum energy is observed experimentally for 50 nm thick targets. However, changes are observed in the ion energy spectrum from a typical TNSA spectra, such as the apparition of peaks. This prevents a conclusion on the existence of an optimum target thickness for the TNSA

acceleration of ions. The experimental results confirm that greater ion energy can be achieved when using targets in the 100s nm thickness range, providing that the laser intensity contrast is good enough to enable the use of such targets.

5.4   Target composition effects

A wide variety of target materials were used during the experiment to investigate the influence of the target composition on the acceleration of ions. This work was primarily focussed on carbons ions, and therefore targets containing carbon were used. The presence of carbon in the bulk of the target was studied using C, CHO and CH foils, and as a surface layer. The cases of an uncontrolled layer (contaminant on Au and Al targets) and a controlled layer (Au+CH targets) were separated. This study was conducted at a laser incidence of 35°, and the results are shown in Fig. 5.3 for protons and C^{6+} ions. The energies were averaged over 3 to 4 shots and targets of thickness L=0.1 μm and L$\simeq$1 μm were used.
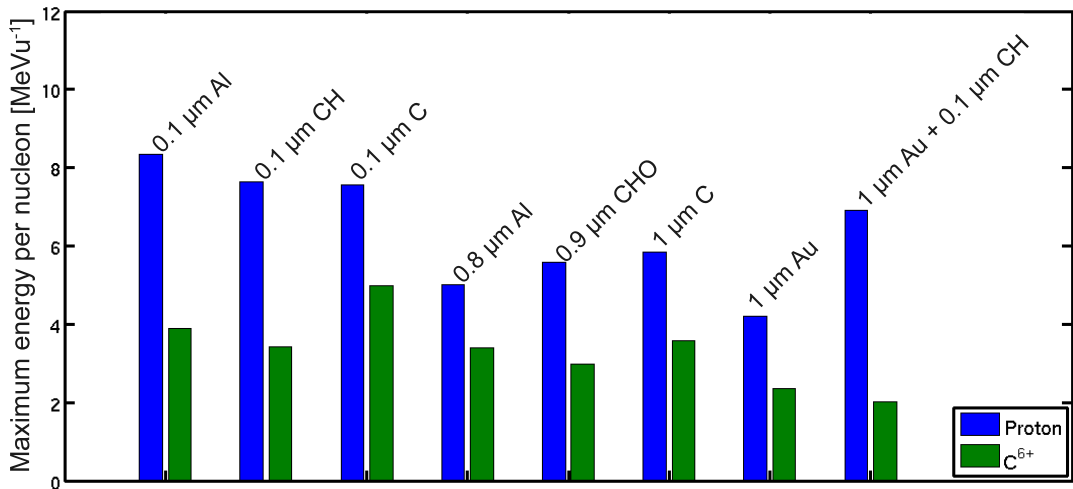
Figure 5.3: Comparison of the averaged maximum ion energy for protons and C^{6+} ions for different target composition and thickness.

First, the proton and C^{6+} ion maximum energies from the carbon-rich targets C, CH and CHO are compared. It is observed that, for a given thickness, the proton maximum energy does not change significantly. It is around 7.5 MeV for C and CH targets at 0.1 μm and around 5.5 MeV for 1 μm C and 0.9 μm CHO. On

the other hand, changes are observed for the C^{6+} energy from the thinnest targets. A significant increase in the energy, from $\sim$3.5 MeV to 5 MeV was measured when pure C targets are shot compared to CH targets. A similar increase, albeit slightly smaller, is observed for the micron-thick C and CHO. This can be explained by the presence of hydrogen in the target, in addition to the contamination layer, which will be preferentially ionised and accelerated creating a screening effect on the heavier C^{6+} ions [156].

For metallic targets such as Al and Au, the protons and carbon ions accelerated in the TNSA mechanism originate from a layer of contaminant on the rear surface, as explained in chapter 2. With the targets in the micron range thickness, a decrease in the maximum energy of both C^{6+} ions and protons is measured compared to the carbon-rich targets. This decrease is most evident for the Au target. This is likely due to the small number of ions available in the acceleration field region. The addition of a controlled source of carbon and hydrogen, in the form of a 0.1 μm CH layer, to a 1 μm Au foil, produces a clear increase in the observed maximum proton energy from $\sim$4 to $\sim$7 MeV. This is due to the higher number of hydrogen atoms in the sheath field at the target rear surface. However, a slight decrease in the carbon ion energy is observed. This confirms the screening effect on the heavier ions caused by the presence of a high number of protons.

5.4.1 Laser cleaning

It is possible to suppress the screening effect caused by the protons and enhance the heavier ion maximum energy [98, 110, 111, 157] by removing the proton source. Multiple techniques can be used to clean the target surface from its contaminant layers. This is most commonly achieved by applying a strong current on the target to resistively heat it to temperatures in excess of 1000° K for $\sim$30 min [98, 110, 111, 157, 158]. This technique is fairly simple to implement but it requires the use of target materials capable of withstanding high temperatures, such as Pd or W, therefore limiting the experimental investigation. In previous work Allen *et al.* [108] used ion sputtering to remove the contaminant layer from the target. This technique has the advantage of enabling the experimenter to

choose which surface of the target to clean, but the ion gun needed to perform the sputtering is bulky and can only be operated in ultra-high vacuum conditions.

Another method of removing the contaminant layers from the target is by laser ablation, or laser cleaning. In this technique a low intensity laser, pulsed or continuous, is focused onto the target surface to be cleaned [112]. As with ion sputtering, laser cleaning enables one specific surface to be cleaned. The vacuum must be high enough such that the rate of ablation is higher than the rate of contaminant recombination on the surface. The fluence on target of the cleaning pulse has to be high enough to ablate the contaminant from the surface but not enough to ionise the surface or melt the target. An off-line experiment at Strathclyde University has demonstrated an optimum laser fluence ~ 3 Jcm^{-2}. This method was used in this work to attempt to remove the contaminant from the target as described in section 5.2.
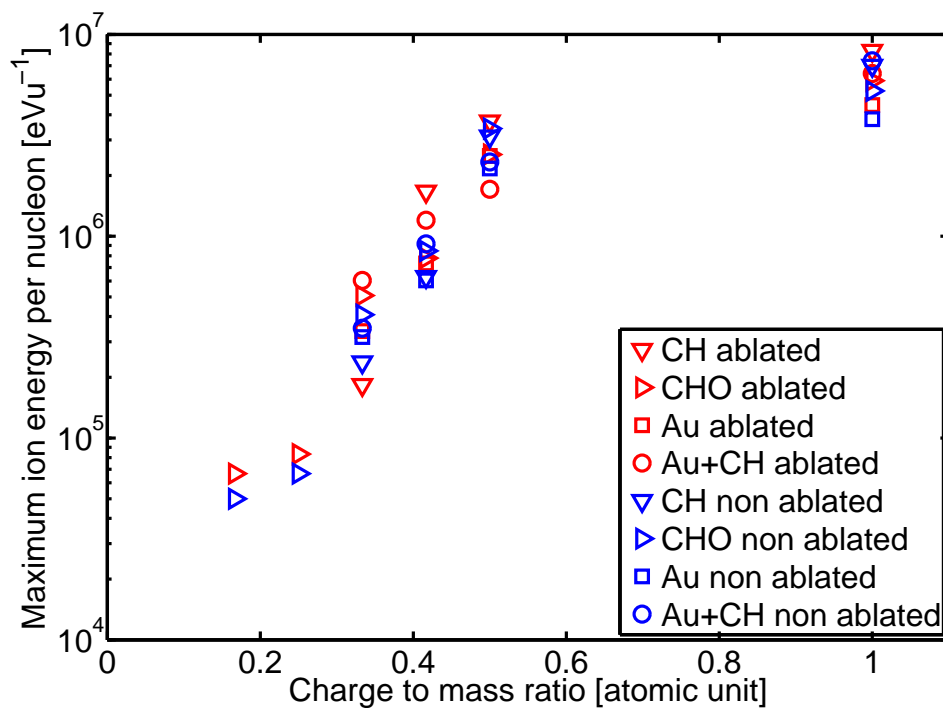
Figure 5.4: Variation of the averaged maximum energy with the charge to mass ratio for ablated (red symbols) and non ablated targets (blue symbols).

The maximum ion energy per nucleon as a function of the charge to mass ratio is plotted in fig 5.4 for different target materials many of which have had

the contaminant layer ablated from the rear surface. The results from cleaned targets are shown in red, and the non ablated targets are shown in blue. It can be seen in Fig 5.4 that removal of the rear surface contaminant layer has had little influence on the measured maximum ion energy, irrespective of the target material or the ion species considered. This appears to disagree with previous work in which a clear increase in the maximum energy of ions heavier than protons was observed [98, 110]. A strong reduction of the proton maximum energy is also expected [108].

The absence of a difference in the ion maximum energy observed in this work can be explained by the delay between the last ablation pulse and the main high intensity laser pulse being too long. As shown in Fig 5.5, the contaminant layer gradually builds up on the target surface at a rate depending on the chamber background pressure. The contaminant layer growth rate is defined by:

$$R_{growth} = \frac{R_{impact}}{\rho} \tag{5.8}$$

where ρ is the contaminant density and R_{impact} is the particle impact rate per surface area defined by [159]:

$$R_{impact} = \frac{P}{\sqrt{3m_c k_B T}} \tag{5.9}$$

where P is the chamber pressure, m_c is the mass of the contaminant and T is the temperature inside the interaction chamber.

During the experiment the pressure inside the vacuum chamber at the moment of the shot was $\sim 5 \times 10^{-6}$ mbar, which corresponds to a growth rate of $\sim 1 \times 10^{-12}$ μm ns^{-1}. The ablation laser used for this work was operated at a frequency of 10 Hz and triggered 1 s before the main CPA pulse, leaving 100 ms before the last ablation pulse and the main CPA pulse. This is the time required to build a 10 Å thick layer on the target. Allen *et al.* [108] measured the thickness of the contaminant layer and found it was ~ 12 Å. Therefore, in the conditions of this work, the contaminant layer had enough time to reappear on the rear surface of the target before the main pulse was triggered. Due to time limitations it was not
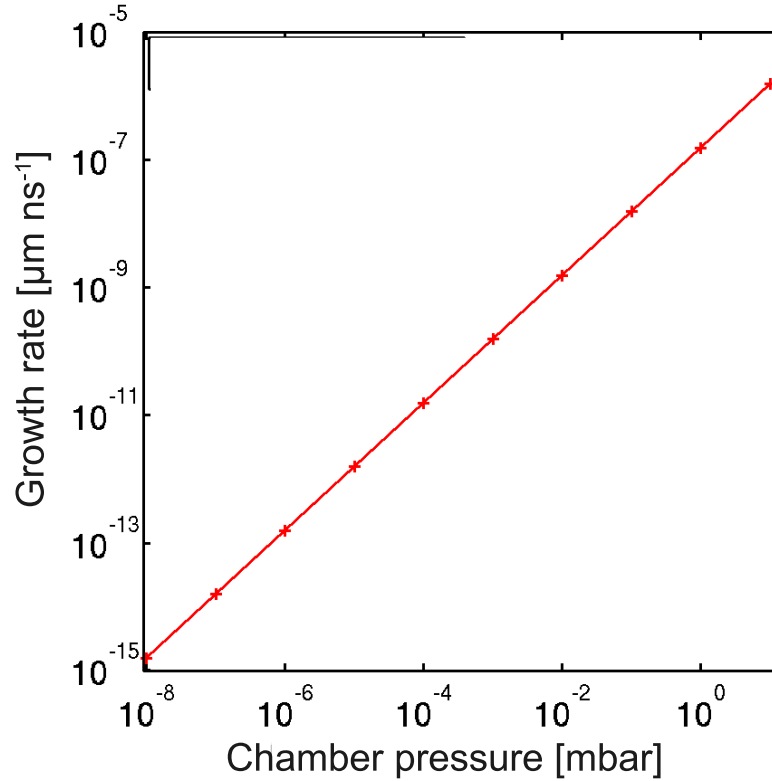
Figure 5.5: Growth rate of the contaminant layer on the target surface as a function of the interaction chamber pressure.

possible to test the effect of varying the timing of the cleaning pulses.

5.5   Ion charge state distribution

Next, variations of the maximum ion energy and total ion energy, averaged over several laser shots were measured as a function of the ion charge-to-mass ratio (q/m). The results are shown in Fig. 5.6. Clear trends are observed despite the large variety of target thickness, material and composition used. A clear increase, of about two orders of magnitudes, is observed for the maximum ion energy over q/m=0.1 to 0.5.

Fig. 5.6 (a) shows, alongside the experimental data, predictions from analytical models of the maximum ion energy from different carbon ion charge states and protons as a function of q/m. The models used are those of Schreiber *et al.* [86] (solid green line) and Andreev *et al.* [153] (solid black line) and are described
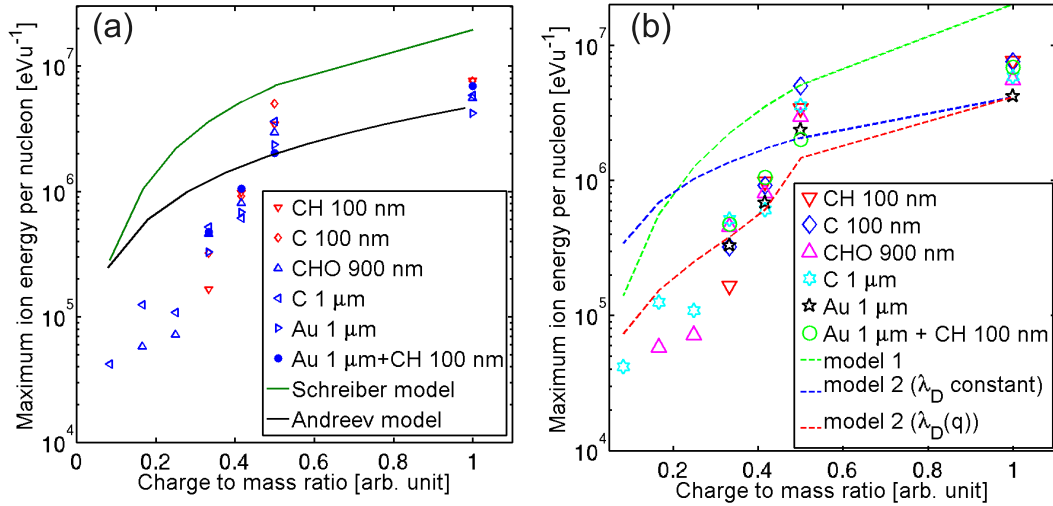
Figure 5.6: (a) Maximum ion energy as a function of the charge-to-mass ratio. The solid lines correspond to estimate from the model proposed by Schreiber *et al.* [86] (green) and Andreev *et al.* [153] (black) as described in the main text. (b) Same experimental data as in (a) compared with simple models of ion acceleration described in the main text.

in section 5.3.2. The models do not take into account the initial charge state population at the target rear surface which has been shown to affect the energy scaling with the charge-to-mass ratio [156]. Despite this limitation, the model introduced by Schreiber *et al.* [86] is in good agreement with the experimental scaling, but over-estimates the maximum ion energy. The model introduced by Andreev *et al.* [153] predicts maximum ion energies that are closer to those measured experimentally. However, both models fail to reproduce the energy observed for the lowest charge state of carbons. This is likely due to screening or other effects by the higher q/m carbons and protons, that are not accounted for in the calculations.

For comparison purposes, the results of a simple calculation of ion acceleration is included in Fig 5.6 (b). In this calculation it is assumed that all the ion species are accelerated by an electrostatic field E_{field}=10 TVm^{-1} for 80 fs. The result is plotted as a green dashed line labelled 'model 1' in Fig. 5.6 (b). The duration of the acceleration is assumed to be 1.3 τ_L and the magnitude of the field is a free parameter chosen to best fit the measurements. Considering that the dominant ionisation mechanism is field ionisation [110, 160], the threshold

field E_q^{thres} required to produce ions of charge q is:

$$E_q^{thres} = \frac{U_{q-1}^2 \varepsilon_0 \pi}{qe} \tag{5.10}$$

where U_q is the ionisation potential in eV for the ion charge q. Using Eq. (5.10) for C^{6+}, $E_q^{thres}=7$ TVm^{-1}. Therefore a magnitude of 10 TVm^{-1} is consistent with the experimental measurements. Despite the simple assumptions of the model it reproduces quite well the maximum energy scaling with q/m. However, the decrease in maximum energy for the low q/m ions is not reproduced because no screening effects are considered.

A second model was developed in which the ions are assumed to gain their energy in a field of constant magnitude extending over the Debye length. The maximum ion energy, $\mathcal{E}_{max}$, is obtained using:

$$\mathcal{E}_{max} = qe\lambda_D E_{field} \tag{5.11}$$

where E_{field} is the magnitude of the accelerating field. The calculation was first made assuming constant λ_D. The results are plotted as a cyan dashed line in Fig. 5.6 (b) and is labelled 'model 2'. The general trend of the calculation is in good agreement with the experimental data. The measured energy for q/m between 0.5 and 1 are well reproduced, but for lower q/m the model over estimates the ion energy.

In a plasma where the ion temperature T_i is not zero, the ion population also contribute to the Debye length. Therefore λ_D becomes a function of q defined as[58]:

$$\lambda_D(q) = \sqrt{\frac{\varepsilon_0 k_B}{e^2 \left(\frac{n_e}{T_e} + \sum_{iq} q^2 \frac{n_{iq}}{T_i}\right)}} \tag{5.12}$$

where n_{iq} is the density of the ion species i. Quasi neutrality of the plasma is

assumed and $T_e = T_i$ therefore Eq. (5.12) becomes:

$$\lambda_D(q) = \sqrt{\frac{\varepsilon_0 k_B T_e}{e^2 n_e \left(1 + \sum\limits_q q^2\right)}} \qquad (5.13)$$

Eq. (5.13) is then used for the calculation of the maximum energy in Eq. (5.11) for E_{field}=10 TVm^{-1}. The results are plotted in Fig. 5.6 (b) as a dashed magenta line. It can be seen that the calculation is in good agreement with the data, and reproduces the drop in maximum energy measured for the lower q/m. This confirms that there is a dynamic evolution of the acceleration field due to ionisation of high q/m ions which plays an important role in the maximum achievable energy for ions with a low q/m ratio.

It should be noted that charge transfer occurring during ion propagation to the detector can influence the measurements. This would result in ions with different charge states having the same maximum energy. Since this is not measured, charge transfer is not expected to play any significant role in the experiment.

5.6 Laser incidence angle effects

Next the effects of the laser incident angle on the acceleration of carbon ions are considered. As shown in Fig. 5.7 (a), a significant enhancement in the ion maximum energy and flux are measured when the laser incident angle is changed from 35° to 0°. The enhancement in $\mathcal{E}_{max}$ is consistent throughout the whole of the target thickness scan as shown in Fig. 5.7 (b). It must be noted that the spatial intensity distribution of the proton beam measured during the experiment does not show evidence of changes in the uniformity or pointing of the beam for the different laser incidence angles. Furthermore, this increase in energy is too large to be solely due to the increase in laser intensity when the target is irradiated in normal incidence compare to oblique incidence.

The result is in stark contrast with previous measurements reported by Ceccotti *et al.* [65] and Ping *et al.* [67] at lower laser intensity. Ceccotti *et al.* [65]
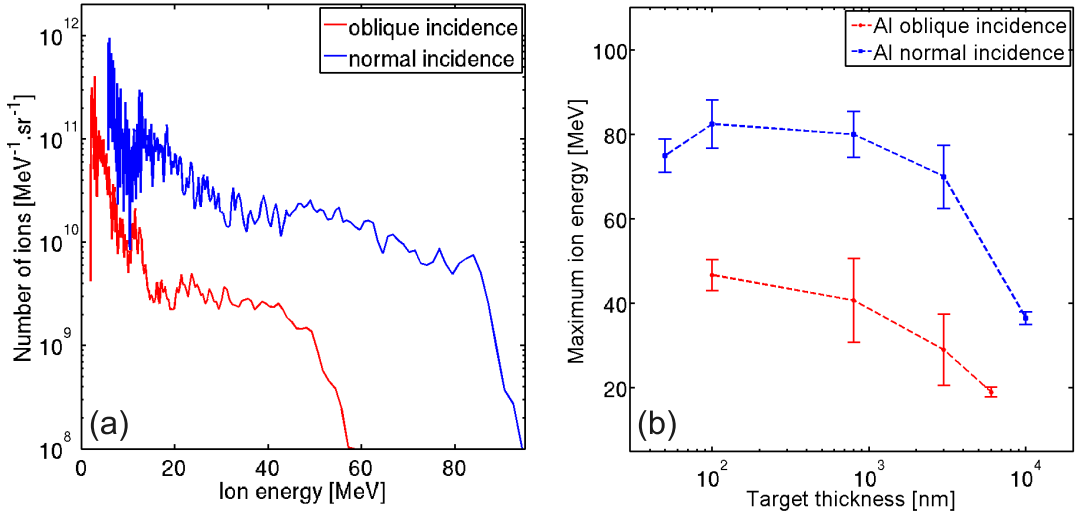
Figure 5.7: (a) Example C^{6+} ion energy spectra from 100 nm thick Al targets irradiated at 0° (normal) and 35° (oblique). (b) Average of the maximum C^{6+} ion energy for Al targets with decreasing thickness for both incident angles.

investigated the effects of laser polarisation on proton acceleration for ultra-high contrast (10^{10}), ultra-short (65 fs) laser pulses focussed to 5×10^{18} Wcm^{-2}. In their work they have kept the laser incident constant at 45° and changed the polarisation of the laser pulse from p-polarised to s-polarised. They observed higher energy protons using p-polarised laser pulses. This can be explained by an increase in laser energy absorption due to the vacuum heating absorption mechanism [63, 161]. As described in chapter 2, this mechanism is more efficient for p-polarised pulses at oblique incident angles.

In this work the laser was kept p-polarised for the whole time, but the switch between normal and oblique incidence is equivalent to a switch between and s and p polarisation. This makes this work comparable to the one presented by Ceccotti *et al.* [65] albeit for higher intensity laser pulses.

The fact that a much more efficient absorption of the laser energy for normal incidence compared to oblique incidence is measured indicates that a novel absorption mechanism, which is a function of the laser incident angle may be accessible at the higher laser intensities used in this work.

To investigate this, a series of 1D-boosted PIC simulations were conducted using a modified version of the code described in [119, 131]. In 1D-boosted simu-
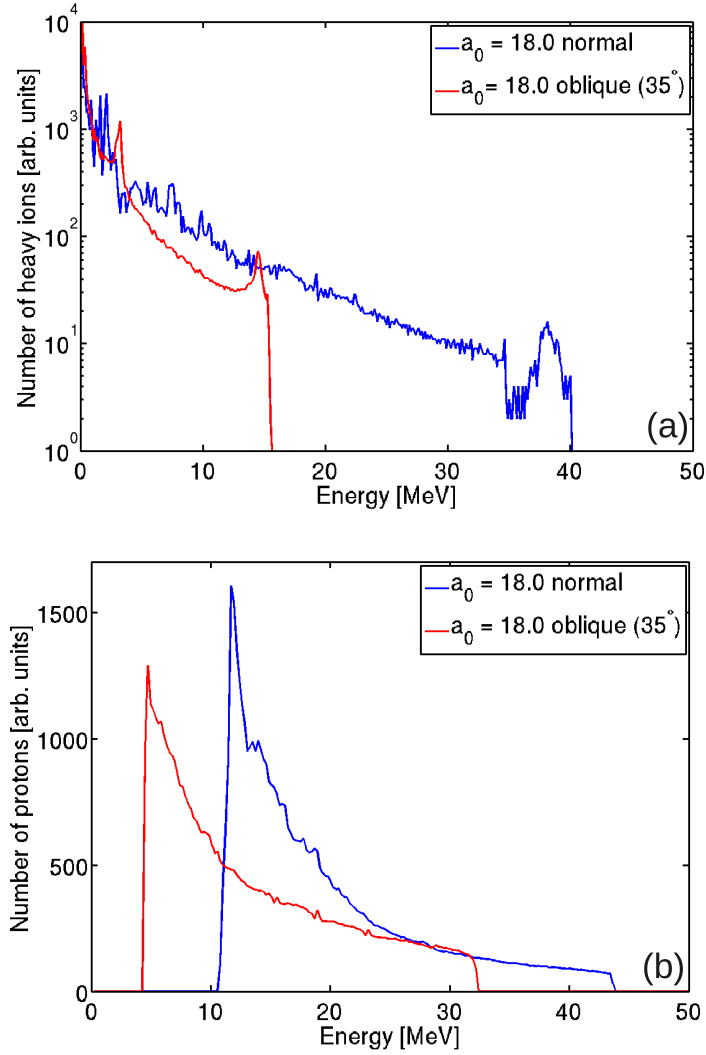
Figure 5.8: 1D-boosted PIC simulation results for protons (a) and 'heavy' ions (b). Both incident angles are investigated, oblique 35° (red) and normal (blue).

lations the calculations are made using one spatial dimension and three velocity dimensions enabling the study of laser plasma interaction at oblique incidence. These simulations were performed by Dr. A. P. L. Robinson at the Central Laser Facility. A 'sin^2' laser profile was chosen with a pulse duration of 50 fs, a wavelength of 800 μm and a dimensionless amplitude a_0 of 18 equivalent to an intensity of 7×10^{20} Wcm^{-2}. The simulation box contains 25 000 cells of individual size of 2 nm, each cell containing 200 particles. The target was composed of a 'heavy' ion bulk (q=1 and mass=$3m_p$) at a number density of $90n_c$. A 20 nm proton layer at the same number density is added at the rear surface of the target. Simulations results from both species at the two incident angles investigated experimentally

are shown in Fig. 5.8 (a-b).

The simulation results clearly show an enhancement in the maximum ion energy in the normal incidence case compared to the oblique incidence. An increase of a factor $\sim$2 is observed experimentally, and this is well reproduced in the simulations. This energy increase is constant for both ion species, suggesting that the ion acceleration mechanism is not modified. This suggests that a more efficient absorption of the laser energy into the hot electrons is responsible for the higher ion energy observed at normal incidence.

5.6.1   The Zero Vector Potential (ZVP) mechanism

Laser parameter study

Baeva *et al.* [162] have recently introduced a new energy absorption mechanism called the Zero Vector Potential (ZVP) mechanism, and this new model is consistent with the experimental results of Fig. 5.7. The proposed mechanism is predicted to occur for ultra short laser pulses interacting with a sharp density gradient target. In the ZVP scheme the presence of moving zeros in the vector potential of the laser enables the production of bunches of fast electrons via a non ponderomotive process.

If the laser pulse is interacting with a plasma density well above the critical density, the ponderomotive force is compensated by an electrostatic field building up in the plasma. The plasma is consequently adiabatically compressed and the electrostatic field building up can be regarded as a 'plasma capacitor'. Electrons can be trapped in the 'plasma capacitor' and are only allowed to escape if the adiabatic state of the system can be broken. This happens in the relativistic case, where moving zeros are present in the vector potential of the laser. In this situation the ponderomotive force vanishes allowing the trapped electrons to co-move with the travelling vector potential zeroes thus moving across the 'plasma capacitor' and gaining energy. The average fast electron energy can be obtained

from a simple estimate of the field of the 'plasma capacitor':

$$k_B T_{eZVP} = \frac{a_0^2 n_c}{n_e} \cos^2(\theta_L)\, k_B T_{eP} \tag{5.14}$$

where n_e is the electron density, n_c is the plasma critical density and θ_L is the laser incidence angle. $K_B T_{eP} = U_p$ is the average energy gained by hot electrons in the ponderomotive potential for a linearly polarised pulse as defined in chapter 2, thereafter referred to as the ponderomotive scaling.

Fig. 5.9 (a) shows $k_B T_{eP}$(blue) and $k_B T_{eZVP}$ (red) as a function of laser intensity for $n_e = 90 n_c$ and $\theta_L = 45°$. It is clear that the ZVP mechanism starts to dominate the fast electron acceleration for laser intensities greater than $\sim 1\times 10^{20}$ Wcm^{-2}. It should also be noted that the hot electron acceleration is more efficient when the ZVP mechanism dominates. This should results in an increase in laser energy absorption for laser intensities $\geq 1\times 10^{20}$ Wcm^{-2}.

As seen from Eq. (5.14) the density of the target plays a major role in the ZVP acceleration of fast electrons. As shown in Fig. 5.9 (b) the laser intensity at which the ZVP mechanism dominates over the ponderomotive mechanism depends on the density of the target and the laser incidence angle. For targets of density close to n_c, the intensity limit is of a few 10^{18} Wcm^{-2} at 45° incidence while it is of a few 10^{20} Wcm^{-2} for a realistic target density ($90 n_c$). Fig. 5.9 (c-d) shows the variation of the hot electron energy as a function of the laser incidence angle for the ponderomotive (blue) and the ZVP mechanism (red) for two laser intensities 5×10^{19} Wcm^{-2} (c) and 5×10^{20} Wcm^{-2} (d). As seen in Fig. 5.9 (d) the increase in average hot electron energy when the laser incidence angle is reduced is faster in the ZVP case than in the ponderomotive case. From an incidence angle of 45° down to 0° $k_B T_{eZVP}$ increases by a factor ~ 1.9 while $k_B T_{eP}$ increase by a factor ~ 1.3.

The total laser energy absorption in laser solid interactions at different laser intensities has previously been measured by Ping *et al.* [67]. A summary of their results at two different laser incidence angles is shown in Fig. 5.10. At 45° incidence the total laser energy absorption remains relatively constant for laser
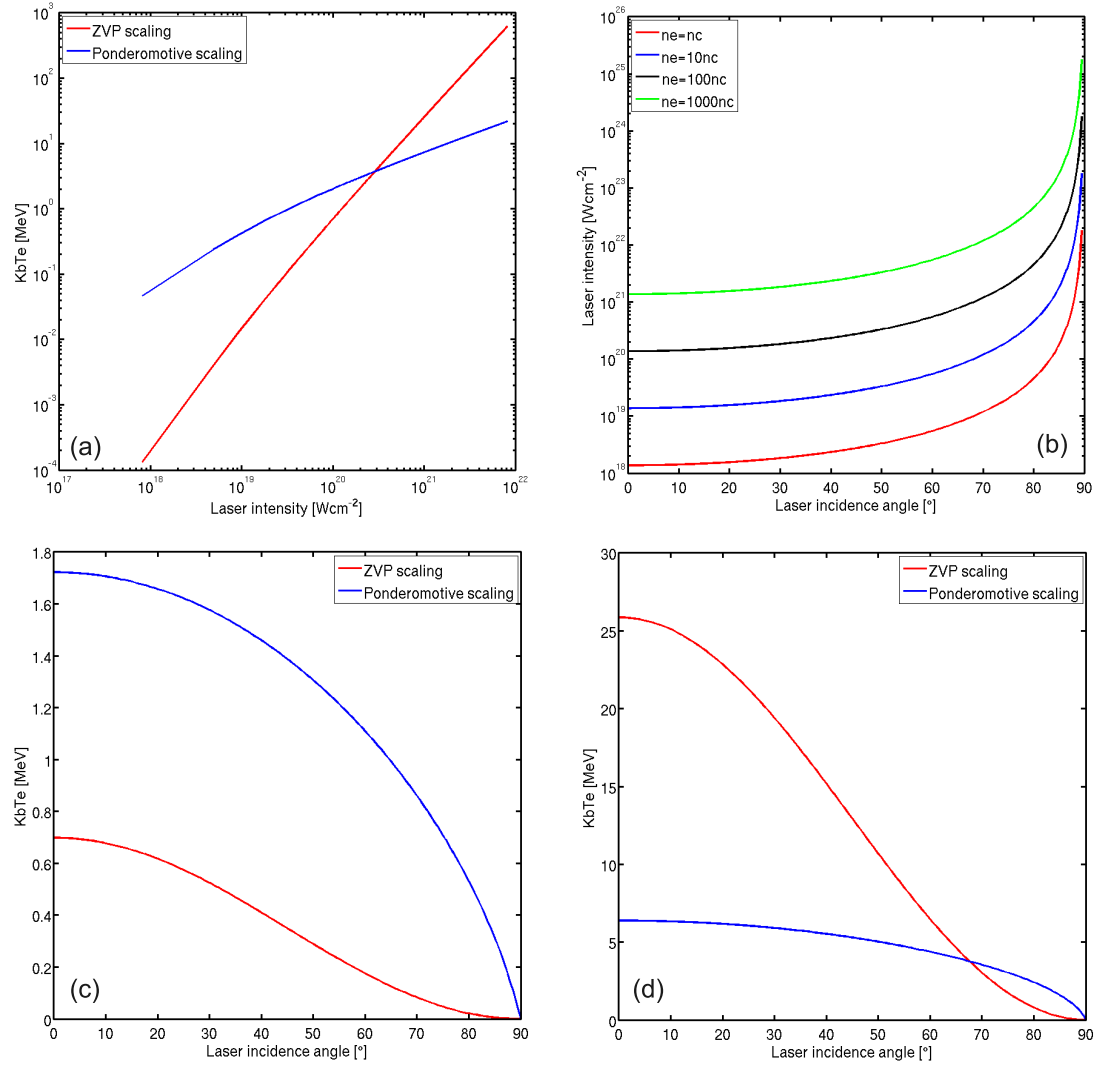
Figure 5.9: (a) Comparison of the hot electron energy as a function of the laser intensity from the ZVP model (red) and the ponderomotive scaling (blue) at a laser incidence angle of 45°. (b) Lower ZVP model laser intensity limit as a function of laser incidence angle for different target density. (c) Comparison of the hot electron energy as a function of the laser incidence angle from the ZVP model (red) and the ponderomotive scaling (blue) for a laser intensity of 5×10^{19} Wcm^{-2}. (d) The same comparison for a laser intensity of 5×10^{20} Wcm^{-2}.

intensities below $\sim5\times10^{19}$ Wcm^{-2}, and sharply increases at higher intensities. A similar trend is observed at near-normal incidence (6°). This result is consistent with the predictions of the ZVP model. In near-normal incidence the total laser energy absorption fraction for laser intensities of $\sim1\times10^{20}$ Wcm^{-2} is found to be of the same order as that measured in the oblique case. The trends, represented as dashed lines in Fig. 5.10, indicate that for laser intensities greater than $\sim1\times10^{20}$

Wcm^{-2}, the total laser energy absorption becomes similar at both laser incidence angle.
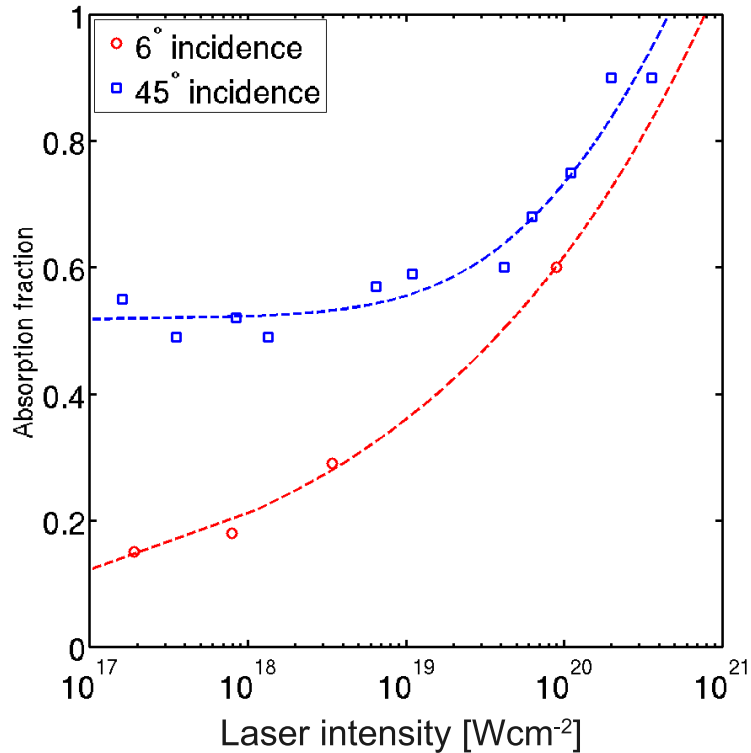
Figure 5.10: Variation of the fraction of laser energy absorbed by the target as a function of laser intensity for 45° and 6° incidence. The data is taken from Ping *et al.* [67]. The dashed lines are guides to the eye.

Comparison with experimental measurements

Fig. 5.11 shows the measured variation of maximum ion energy with the laser incidence angle for two laser intensities 7×10^{20} Wcm^{-2} and 1×10^{19} Wcm^{-2}. In the 7×10^{20} Wcm^{-2} case, the energy is measured for C^{6+} ions from a 100 nm thick Al target irradiated with the GEMINI laser. For the lower laser intensity the energies are measured for protons from 20 μm thick Cu foils irradiated with 1 ps laser pulses from the PHELIX laser presented in chapter 4. The experimental conditions for these data are described in detail in chapter 6.

The data presented in Fig. 5.11 are compared with results from the model introduced by Mora [83] presented in chapter 3, for C^{6+} for the high laser intensity (solid line) and protons for the low laser intensity (dashed line). The hot elec-

tron temperature is calculated using the ZVP model (Eq. (5.14)) (red) and the ponderomotive scaling (blue). As shown in Fig. 5.11, the Mora models predicts a higher maximum ion energy for the ponderomotive scaling compared to the ZVP scaling in the low laser intensity case and the opposite in the high intensity case. This is consistent with the comparison of average hot electron energy shown in Fig. 5.9 (a, c-d). The measured variation of maximum proton energy at the lower laser intensity with laser incidence angle is found to be well reproduced by the Mora model when the ponderomotive scaling is used. In the high laser intensity case the variations of C^{6+} ion energy with laser incidence angle is best reproduced with the ZVP scaling of electron temperature.

The dependence of the laser incidence angle is introduced in the ponderomotive scaling by reducing the laser intensity with increasing incidence angle. This indicates that the decrease in proton energy measured at lower intensity is mainly due to the reduction of the laser intensity caused by the greater incidence angles. For the higher laser intensity, the results cannot be reproduced by the ponderomotive scaling, indicating that the hot electron acceleration is dominated by a new mechanism. The above analysis of the ZVP mechanism, suggests that this is a candidate for the new absorption process at high intensity as proposed by Baeva *et al.* [162].

The Mora model is also used to estimate the variation of maximum ion energy with decreasing target thickness for laser intensities of 6 to $7{\times}10^{20}$ Wcm^{-2}. As shown in Fig. 5.12, the increasing trend of maximum ion energy with decreasing target thickness is predicted by the Mora model using both the ponderomotive and the ZVP hot electron average energy scaling. However, the maximum ion energy is consistently under-estimated when the ponderomotive scaling is used, while the results obtained with the ZVP scaling are in good agreement with the experimental data. This further suggests that the hot electron acceleration is dominated by the ZVP mechanism for laser intensities above $1{\times}10^{20}$ Wcm^{-2}. It also indicates that the ZVP absorption mechanism is independent of target thickness.
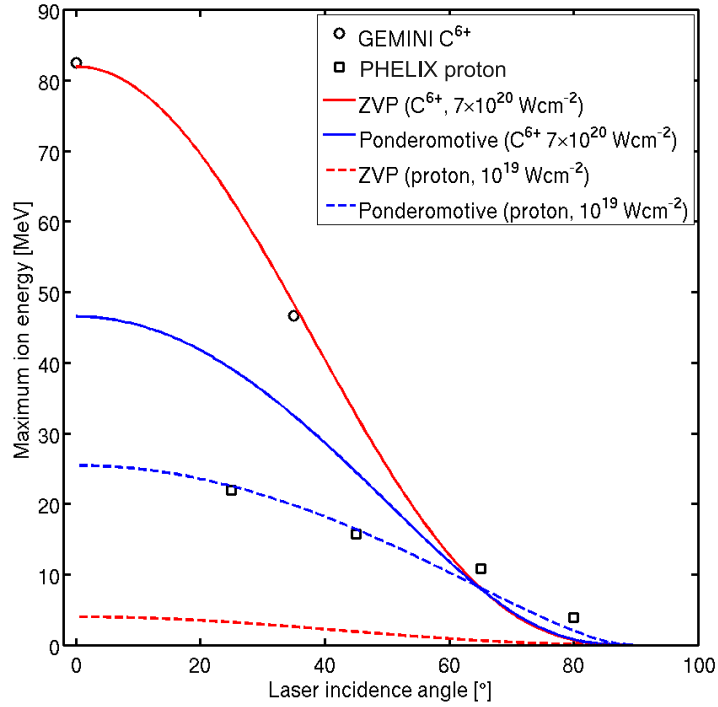
Figure 5.11: Measured maximum C^{6+} ion and proton energy at a laser intensity of $7{\times}10^{20}$ Wcm^{-2} (circle) and $1{\times}10^{19}$ Wcm^{-2} (square). Results from the Mora model using the ZVP scaling (red) and the ponderomotive scaling (blue) are also shown for C^{6+} ion in the GEMINI conditions (solid lines) and proton in the PHELIX conditions (dashed lines).

5.7   Conclusions

In this chapter a study of ion acceleration using thin foils irradiated by ultra-high contrast 10^{10}, ultra-short 50 fs, ultra-high intensity $7{\times}10^{20}$Wcm^{-2} laser pulses is reported. The objective was to find the target and laser pulse parameters for which the carbon ion acceleration is optimised using the new laser parameter regime enabled by the new ASTRA-GEMINI laser facility.

The maximum C^{6+} ion energy was measured to increase with decreasing target thickness down to 100 nm. This is found to be largely independent of target material. A slight decrease in the maximum ion energy was measured for targets with a thickness of 50 nm. However, changes in the energy spectrum at 50 nm thickness (apparition of mono-energetic-like peaks) point to the onset of an acceleration mechanism other than TNSA, possibly radiation pressure acceleration.

The highest C^{6+} ion energy was measured with a pure C target. The presence
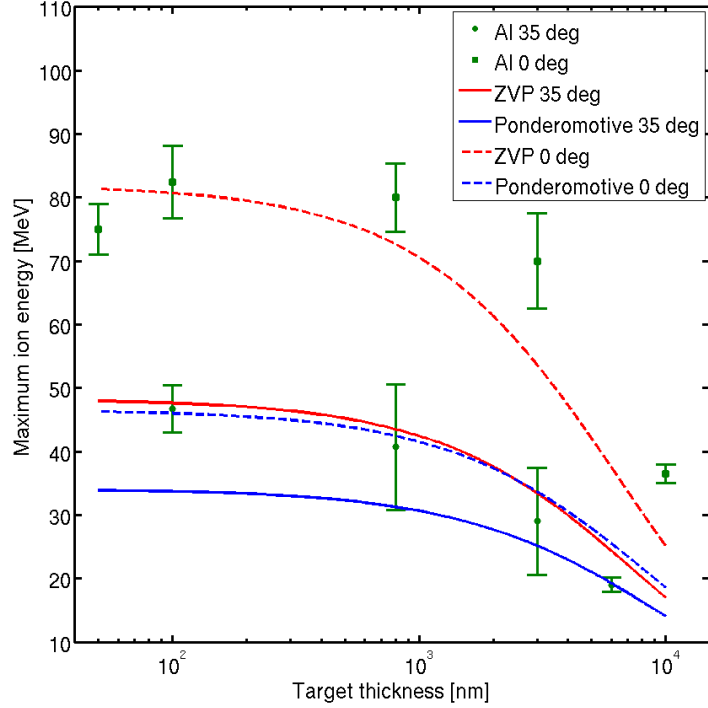
Figure 5.12: Measured maximum C^{6+} ion energy as a function of target thickness for the 0° laser incidence (square) and 35° laser incidence (circle). The lines represent the results from the Mora model calculations using the ZVP scaling (red) and the ponderomotive scaling (blue) to estimate the electron temperature at the two laser incidence angles (0° dashed, 35° solid).

of hydrogen, either in the bulk of the target or as a controlled contamination layer is found to notably reduce the C^{6+} maximum energy via screening of the acceleration field. On the other hand, targets made of high-Z material such as Au, with a hydrogen source layer at the rear give the best results for the acceleration of protons.

A clear increase in the ion maximum energy as a function of the charge-to-mass ratio is measured. This is best reproduced analytically by assuming that all the ions are subject to a uniform acceleration in a constant electric field over the Debye length of the plasma forming at the rear of the target. This simple calculation is in good agreement with the experimental trend. However, the energy measured for low q/m is reproduced only if dynamic effects are taken into account by considering the ion contribution to the Debye length.

Arguably, the most interesting result of this study is the first experimental

observation of a significantly higher (a factor of ∼2) ion maximum energy for targets irradiated at normal compared to oblique incidence. This contrasts sharply with previous work [65, 67] at lower intensity. This enhancement is supported by 1D-boosted PIC simulations reproducing the increase factor. The measured increase in energy cannot be explained by the increase in laser intensity alone (when the laser irradiate the target normally compared to the oblique incidence), which suggests that a new absorption mechanism may be accessible with the laser parameters used in this work. Recent theoretical work by Baeva *et al.* [162] introducing a new laser to hot electron absorption mechanism, called Zero Vector Potential absorption, predicted to be dominant in the interaction of ultra-short ultra-intense laser pulses with a steep density gradient, may explain the experimental results. Detailed numerical and experimental work will be carried in the future to fully investigate this new absorption regime.

Chapter 6

Controlling the properties of laser accelerated proton beam using mass limited targets

6.1 Introduction

As described in chapter 3, at laser intensities $\simeq 1 \times 10^{19}$ Wcm^{-2} ions are mainly accelerated by the TNSA mechanism. Although significant progress has been made towards enhancing the ion energies obtained via the TNSA mechanism, further development is needed to increase the ion energies to the level required for some of the applications envisaged. One way of enhancing the maximum ion energy is to increase the energy of the laser pulse drive. While more powerful lasers could give access to more efficient acceleration mechanism, such as RPA, there are strong financial and technical limitations to the maximum achievable laser pulse energies at present. The use of multiple laser pulses has been experimentally investigated [163, 164] and show promising results. Another possibility is to engineer the target to enhance the TNSA mechanism. This has been investigated experimentally by using targets of decreasing thickness [81]. In addition to the maximum ion energy, control of the divergence of the beam is also highly desirable. This can be done by using secondary electric fields from complex target geometries [165, 166], RF cavities [167] or multiple laser pulses [168].

Hot electrons have previously been observed to spread on the target surface by McKenna *et al.* [160] and Quinn *et al.* [169]. McKenna *et al.* [160] show that, in thin foil targets, secondary ion sources can be observed at the target edges. This is attributed to the hot electron population spreading on the target surface and piling up at the edges, giving rise to an electric field capable of ionising and accelerating ions to MeV energies. Quinn *et al.* [169] report on the propagation of hot electrons along a wire target and measure their velocity using proton radiography. They report that the speed of the hot electrons on the target surface is $\sim c$. Furthermore, 2D Hybrid-PIC simulations reported by McKenna *et al.* [160] show that upon reaching the target edges the hot electrons are reflected back towards the centre of the target giving rise to lateral refluxing of the hot electrons.

Laterally refluxing electrons can potentially be used to enhance the TNSA proton energy. Burza *et al.* [170] introduced the concept of using hollow micro sphere targets to create a staged acceleration of protons. They irradiated one pole of the sphere to generate TNSA protons directed towards the opposite pole, where a hole is drilled. The radius of the sphere is chosen to enable the laterally refluxing electrons to reach the edges of the hole and induce a transient secondary electric field as the protons approach. The secondary field will boost the proton bunch energy as it passes through the hole, thus creating a staged acceleration. This method effectively reuses fast electrons which normally escape from the laser focal region and is a promising approach to boosting the proton energy.

Another method that has been investigated is the use of planar foil targets of limited lateral extent (in the 100s of nm range), the so called 'mass limited targets'. In these targets, the laterally refluxing electrons return to the TNSA region of the target enhancing the duration of the accelerating field. This scheme has been the subject of several numerical [171, 172] and experimental studies [145, 146, 172]. Buffechoux *et al.* [172] were the first to experimentally measure the enhancement of the maximum TNSA proton energy using square foil targets of lateral size ranging from 3 mm down to 30 μm, irradiated with a 400 fs duration pulse at an intensity of 2×10^{19} Wcm^{-2}. They reported that the maximum proton energy is relatively constant for targets with transverse size between 3 mm and

300 μm and increases for targets smaller than 300μm.

In this chapter results of a numerical and experimental investigation of the transverse spreading of hot electrons in mass limited targets are presented. It is shown that laterally refluxing hot electrons can be used to enhance the TNSA acceleration of protons for larger targets and longer pulse durations than these reported in [172]. The first measurements of an increase in the maximum energy of protons originating from the edges of the target is also presented. In addition, by developing a simple model, supported by experimental evidence, it is shown that engineering the geometry of the mass limited target can be used to control the spatial distribution of the TNSA proton beam. The work presented in this chapter was published in Ref. [173].

6.2 Experiment

The experiment was carried out using the PHELIX laser at GSI in Darmstadt, as described in chapter 4. The laser delivered pulses of 1 ps duration, at a wavelength of 1.054 μm, with $\simeq$90 J of energy on target. The pulses were s-polarised and irradiated thin foil targets at an incidence of 45°. An f/6 off-axis parabolic mirror was used to focused the laser to a 30$\times$13 μm (FWHM) spot, containing $\sim$40% of the laser energy, resulting in a peak intensity of $1\times10^{19}\,\mathrm{Wcm}^{-2}$. The contrast measured 3 ns prior to the main pulse was 10^7.

The targets were 20 μm-thick Cu foils with varying lateral dimension (5 mm$\times$5 mm, 2 mm$\times$2 mm, 400 μm$\times$400 μm and 100 μm$\times$100 μm). 20 μm thick Cu isosceles triangular (base: 400 μm, length: 400 μm) and 400 μm diameter circular targets were also used. Schematics of the targets are shown in Fig. 6.1

An array of stacked RCF films, as described in chapter 4, were used to detect the multi-MeV protons originating from the target. The stacks were placed around the target normal axis to cover an arc of 230° in the horizontal plane as shown in Fig 6.2. Only the lower half of the proton beam was sampled by the RCF to permit the use of other diagnostics. In addition to the RCF stacks, the Kα emission was recorded using a reflective Bragg crystal, as described in chapter
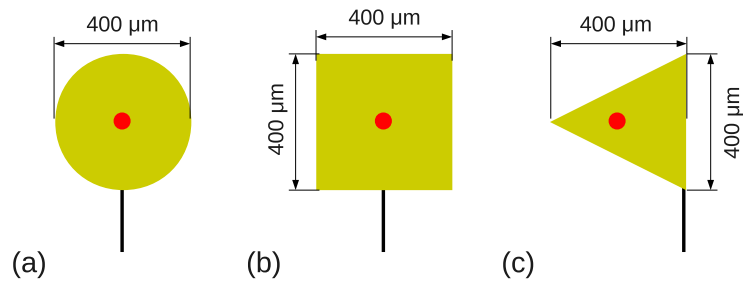
Figure 6.1: Schematic of the targets (a) circular, (b) square and (c) triangular. The red dot indicates the approximate position of the laser spot.

4. The broad-band X-ray emission was imaged using a pinhole camera. Both the $K\alpha$ and the X-ray emission were measured using Fujifilm image plates (chapter 4). A transverse frequency-doubled optical probe was used to monitor the plasma expansion. A schematic of the experimental set-up is shown in Fig. 6.2.
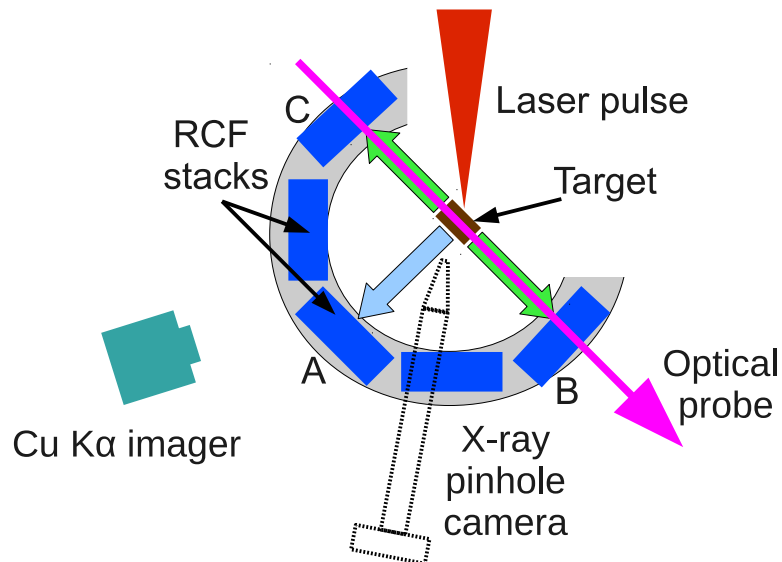
Figure 6.2: Schematic of the experiment setup. Five stacks of RCF dosimetry film were positioned in a 230° arc centred on the target normal direction ('A'). Proton emission from the target edge is recorded in position 'B' and 'C'. The pinhole camera and the $K\alpha$ imaging crystal were placed out of plane to record the X-ray emission from the target.

6.3   Enhancing the maximum proton energy

6.3.1   Experimental results

Measurements of the TNSA-proton maximum energy (recorded in position 'A' in Fig. 6.2) obtained with the various different targets are shown in Fig. 6.4 (a). For targets of dimensions greater than 100 μm×100 μm a clear increase in maximum proton energy is observed with decreasing target surface area. The low energy observed for the smallest target is due to the plasma generated by the laser pre-pulse at the front of the target leaking to the back surface and disrupting the TNSA mechanism. This is confirmed by the transverse optical probing of the target as shown in Fig. 6.3 (a-b).
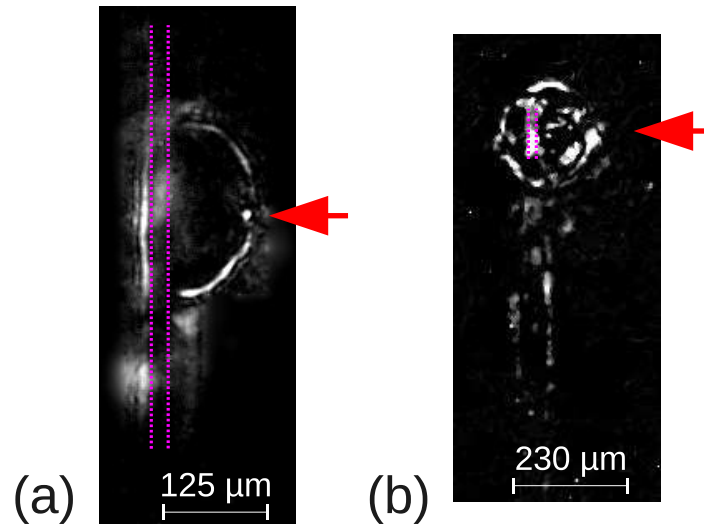
Figure 6.3: Images of the plasma expansion taken using the optical probe for (a) 5 mm×5 mm and (b) 100 μm×100 μm targets. The arrows corresponds to the direction of the laser and the dashed line to the target front and rear surfaces. In (a) the target rear surface remains largely undisturbed. In (b) spherical expansion of the target is observed.

The laser intensity contrast is the limiting factor for the minimum usable target size. The laser-to-proton energy conversion efficiency, $\eta_{L \to p}$, is also shown in Fig. 6.4 (a), and is also found to increase with decreasing target surface area. Fig. 6.4 (b) shows the maximum proton energy from the target edge as a function of surface area (recorded in position 'B' in Fig. 6.2). It shows a similar enhancement of the maximum proton energy with decreasing target surface area.

A comparison of the proton beam obtained from opposite edges (position 'B' and 'C' in Fig. 6.2) shows that the emission is identical.
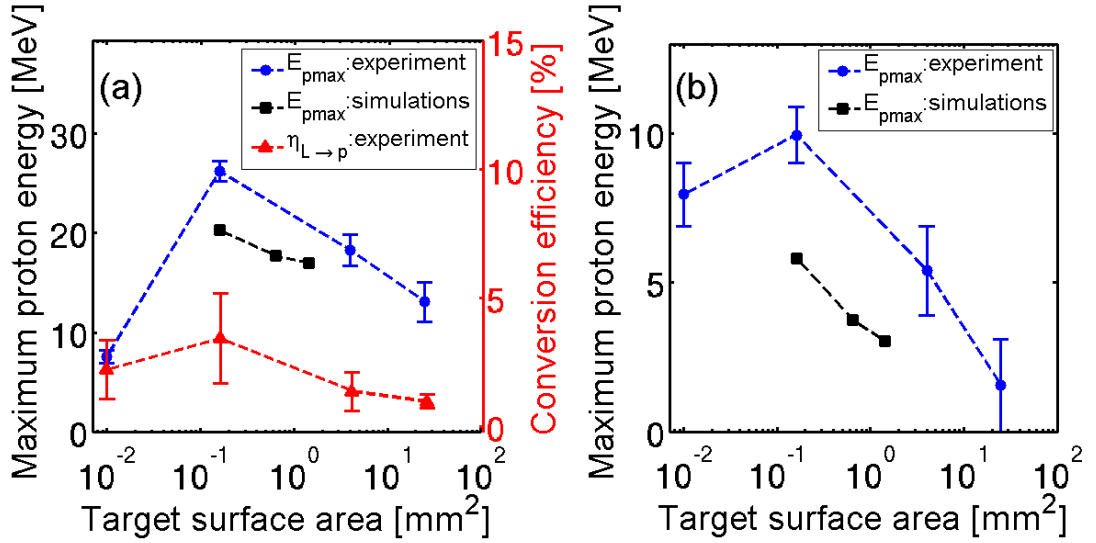
Figure 6.4: Experimental measurements of the maximum proton energy as a function of target surface area. (a) Maximum energy measured in the normal direction (TNSA) (position 'A') as well as the corresponding laser to proton conversion efficiency $\eta_{L \to p}$. (b) Maximum proton energy from the target edge as a function of surface area (position 'B').

The increase in the maximum TNSA-proton energy is explained by the lateral refluxing of hot electrons. When the hot electron population reaches the target rear surface the electrons spread radially until they reach the edges, where they are reflected. If the target lateral dimensions are small enough that the reflected hot electrons can reach the central region while the ion acceleration is still occurring the ion acceleration time is extended, enhancing the ion maximum energy [171]. This has been previously observed by Buffechoux *et al.* [172] with smaller targets (3 mm down to 30 μm). The fact that here this enhancement is measured for larger targets is explained by the differences in the laser pulse parameters. The work by Buffechoux *et al.* [172] involves a smaller focal spot (6 μm), higher intensity contrast and shorter pulse duration (400 fs). The shorter pulse duration is likely to be the main reason for the maximum energy increase observed with smaller targets. In the case of a 400 μm×400 μm target the laterally refluxing electrons, travelling at $\sim c$, would perform one reflux (from the target centre to

the edge and back) in 600 fs. Therefore, for a 400 fs pulse duration the electrons do not have time to reflux during the ion acceleration time t_a (assuming that $t_a \simeq 1.3\tau_L$ with τ_L the laser pulse duration [91]). By contrast, in the case of a 1 ps laser pulse duration, the electrons have enough time to reflux twice during the ion acceleration time. As demonstrated by Kluge *et al.* [171], the laterally refluxing electrons can only contribute to the acceleration if they return within the ion acceleration time. The higher density of the hot electron population at the edges of the smaller targets explains the enhancement in the maximum energy of protons accelerated from these parts of the target.

A summary of the laterally refluxing electron dynamics is presented in Fig. 6.5. As discussed in chapter 3, the laser generated hot electron population can only propagate if a return current can be established. As the laterally refluxing hot electrons reach the target edges, no further background electrons are available to establish a return current. The hot electrons therefore cannot expand further than the Debye length and are reflected back into the target, enhancing the TNSA field if they arrive back to the target centre whilst the ion acceleration field is still present.
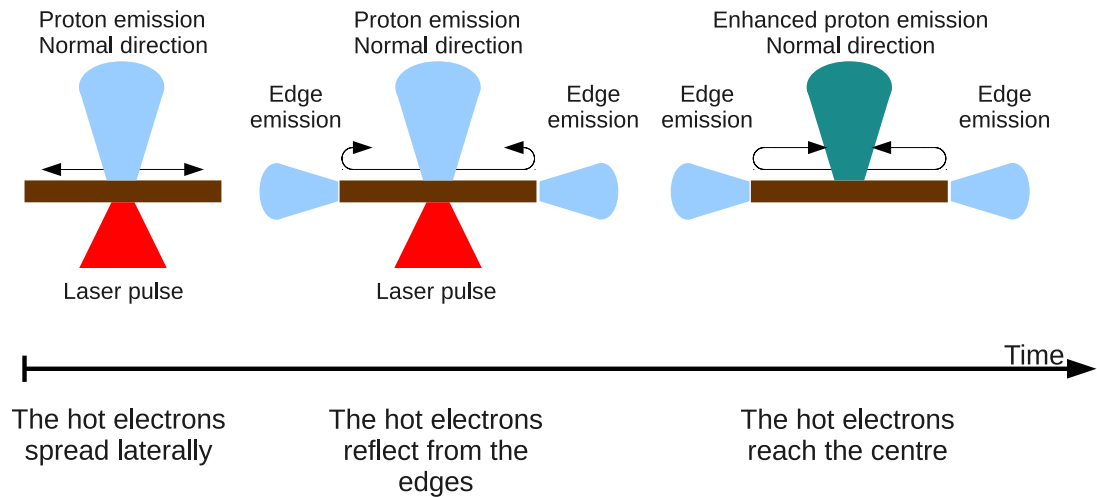
Figure 6.5: Schematic summarising the lateral refluxing of hot electrons and the enhancement of the maximum energy of TNSA protons.

6.3.2   2D PIC-Hybrid simulations

To further investigate the effects of the laterally refluxing hot electrons, 2D hybrid PIC simulations were conducted using the LSP code. The interaction of a 1 ps laser pulse at an intensity of $1 \times 10^{19}\,\mathrm{Wcm}^{-2}$ with a 20 μm thick Cu target of varying size was simulated. The targets were disks, the radius of which was varied between 200 μm and 600 μm. The maximum target radius was defined by the limitations in computing resources. The simulation grid size was 900 μm×900 μm with 3600×3600 cells. The temporal evolution of the electric field was determined at selected positions on the target back surface, and this was used to calculate the resulting maximum proton energy, using:

$$\mathcal{E}_{max} = qe\lambda_D E_{sheath} \tag{6.1}$$

where λ_D is the Debye length, q is the ion charge and E_{sheath} is the electric field strength.

A previous investigation of the lateral refluxing of the hot electron population was previously reported by McKenna *et al.* [160], and used the same 2D hybrid PIC code as in this work. A simulation box of 600 μm×600 μm with 2400×2400 cells was used, with a laser intensity of 1×10^{19} Wcm^{-2}. The size of the target and the pulse duration were scaled down due to the limitations of the computing resources. A target of 400 μm radius was used (compared to 2 mm in the experiment) and the pulse duration was set to 200 fs compared to 1 ps used in the experiment. The temporal evolution of the electron density and potential drop at given positions along the target surface is presented in Fig. 6.6.

A charge wave propagating along the surface can be clearly seen in Fig. 6.6. At 300 μm from the target centre in Fig. 6.6 (c), the potential drop rises around 1.0 ps and drops around 1.5 ps (corresponding to a wave propagating at $0.75c$), the potential then increases again around 2.0 ps corresponding to the reflection of the charge wave from the target edge. This evolution is observed for different positions along the target. An increase in the field in the central region is not observed as the simulation time is too short. It should be noted that a temporal broadening of
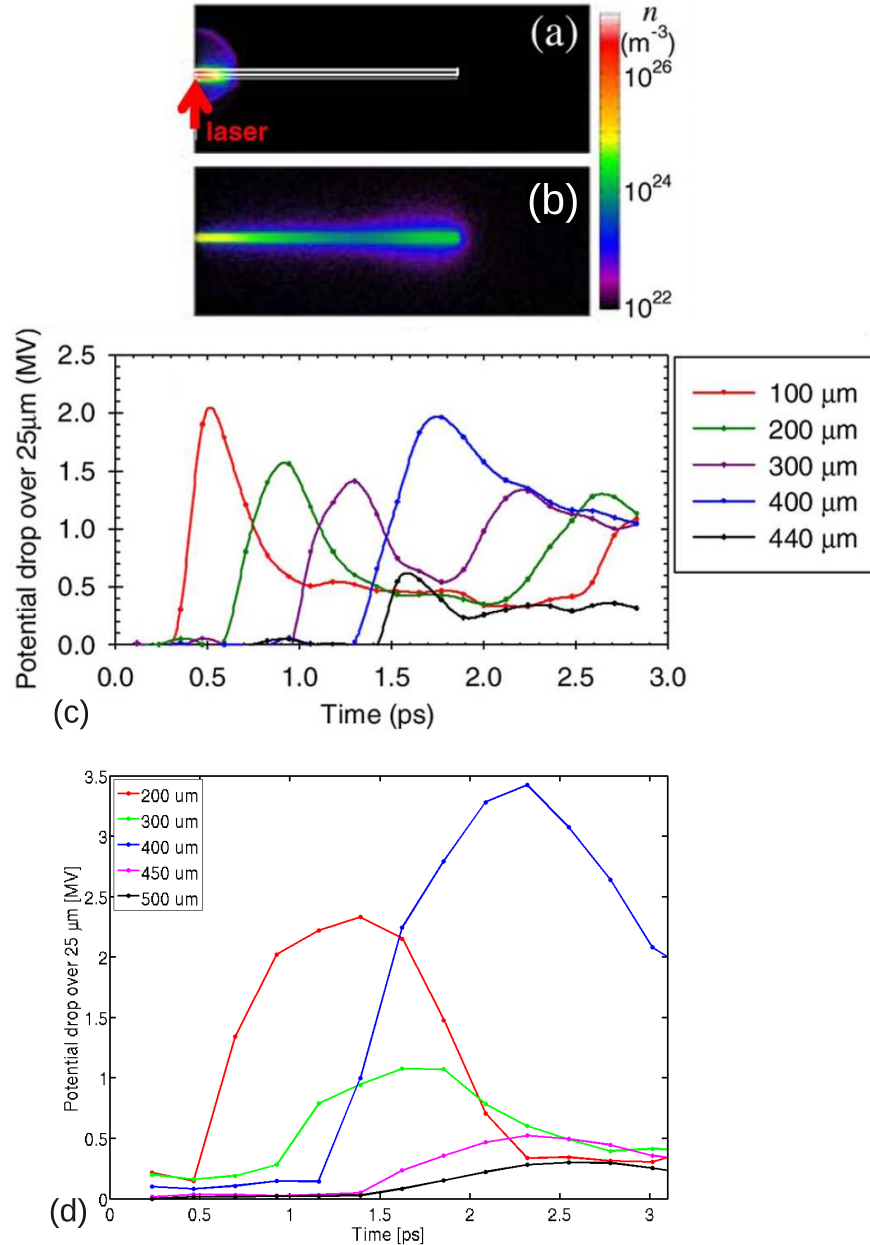
Figure 6.6: (a-b) Electron density at 0.25 ps and 2.5 ps respectively as presented in Ref. [160]. (c) Temporal evolution of the simulated potential drop at given radii as reported in Ref. [160]. (d) The same for the longer pulse duration used for the results presented in this chapter.

the charge wave occurs as the wave travels along the target surface resulting in a decreasing potential drop as it propagates. The increase in the peak potential drop observed at the target edge is explained by the electrons being reflected there. Fig. 6.6 (d) presents the same simulation results for a laser pulse duration of 1 ps. The longer pulse duration explains why the charge wave observed in Fig. 6.6

(d) is much broader than in Fig. 6.6 (c). The velocity of the charge is similar in both simulation results. In case (d) the reflected wave cannot be distinguished from the outward wave due to the electron pulse duration. However, a similar increase of the electric field at the target edge is observed in Fig. 6.6 (c) and (d), confirming the presence of the refluxing electron population.

6.4 Measurements of the relative temperature variation

During the same laser shots the Kα emission from the target was recorded using an imaging crystal to determine the effects of the laterally refluxing electrons on the target temperature. Fig. 6.7 shows the intensity of the Kα line emission integrated over the image. The data is normalised to the 5 mm × 5 mm target case. It is observed that the Kα line emission decreases with decreasing target surface area which results from an increase in the target temperature. As discussed by Baton *et al.* [146] this is due to the confinement of the electrons to a smaller volume. The increase in temperature of the target induces a reduction of the Kα line intensity and a shift in the wavelength which can be sufficient to bring the emission out of the imaging crystal bandwidth. Therefore, the intensity of the signal measured with the imager is reduced. As described by Akli *et al.* [145] the variation of the intensity of the signal recorded with a Kα imager can be used to estimate the temperature variation of the target.

The crystal used in this work is spherically bent quartz. The incidence angle of the X-ray emission on the crystal was chosen so that the Cu Kα photons, of energy 8046 eV, were reflected towards the detector. The crystal bandwidth was ΔE=6 eV. Based on the work by Akli *et al.* [145] at similar laser intensities targets temperature of approximately 20 eV are expected for target volumes of 5×10^8 μm^3 and 90 eV for a target volume of 3×10^6 μm^3, corresponding to the range of targets used in this work. This results is used to put the present relative measurements on an absolute scale.

Using FLYCHK, the variation of the Kα line emission intensity with increas-
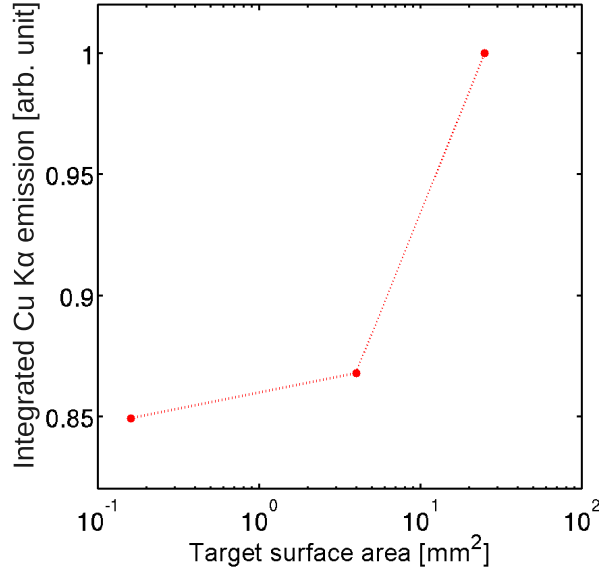
Figure 6.7: Measured variation of the integrated Cu Kα intensity with target surface area.

ing target temperature was modelled. The temperature of the target was varied between 20 and 60 eV. The electron density was estimated using the solid ion density $\simeq 1\times10^{24}$ m^{-3}. A second hot electron population was included in the simulations. It has a temperature of 1 MeV and represents 1% of the total electron population. The spectra obtained are presented in Fig. 6.8 (a) and clearly shows the reduction in the signal intensity as well as the wavelength shift as the target is heated. The bandwidth, ΔE, of the imaging crystal is represented by the dashed lines. For each target temperature the Kα emission is integrated over the bandwidth, the results are shown in Fig. 6.8 (b).

It is possible to estimate the temperature of the smaller size targets by comparing the variation in the measured Kα emission for the different target sizes to the modelled Kα emission. Using this approach it is found that the temperature increases by ~4 eV for the 2 mm×2 mm target, and ~4.5 eV for the 400 μm×400 μm target, as shown in Fig. 6.9. Baton *et al.* [146] reports temperatures of 10 eV for 20 μm thick 300 μm×400 μm targets irradiated with lower laser intensity, 5×10^{17} Wcm^{-2}.

From the work by Akli *et al.* [145] an increase of approximately 70 eV is expected over the target volume range explore in this work, however an increase
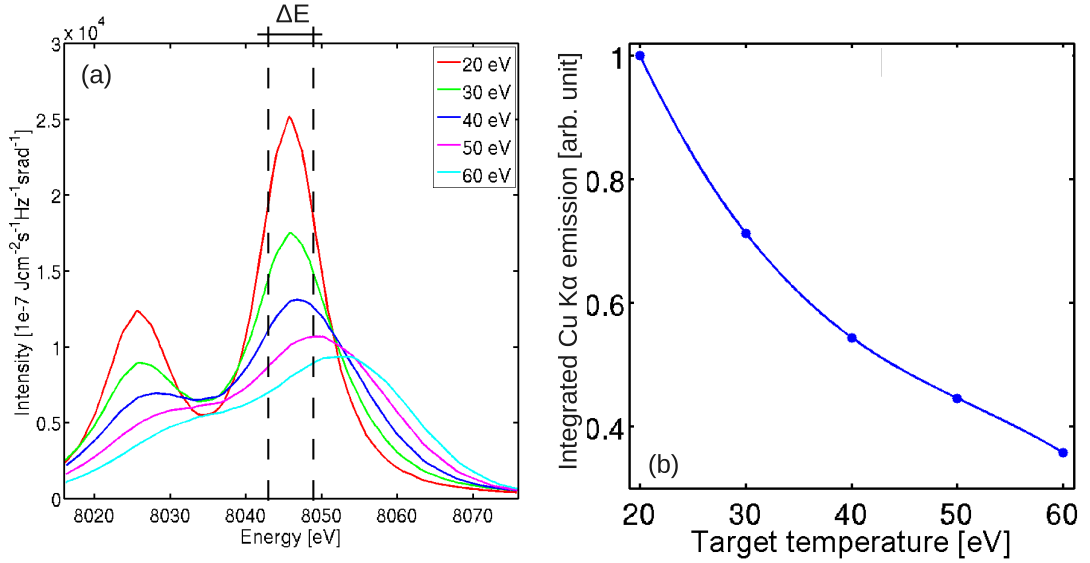
Figure 6.8: (a) X-ray emission spectrum obtained with FLYCHK for different target temperatures. The bandwidth, ΔE, of the crystal is represented by the dashed lines. (b) The normalised emission integrated over ΔE as function of the target temperature.

of only 4.5 eV is measured. In the work of Akli *et al.* [145] the lateral dimensions of the targets are 100 μm×100 μm and 500 μm×500 μm and the thickness is also varied (30 μm, 20 μm, 5 μm and 1 μm). The higher temperature measured in their work can be explained by the use of thinner targets. As demonstrated by Quinn *et al.* [147] the refluxing electron population increases the bulk target temperature. This temperature increase is dependent on the number of longitudinal refluxes occurring in the target. Therefore for a fixed target volume, the thinnest target is expected to have the highest temperature. Thus this confirms that the laterally refluxing electrons are responsible for the increase in target temperature measured via the Kα emission.

6.5 Controlling the spatial distribution of the proton beam

The lateral refluxing of fast electrons offers the possibility to control the spatial distribution of the proton beam. This technique hinges on the TNSA accelerating field distribution being controlled by the target geometry. For a disk target the
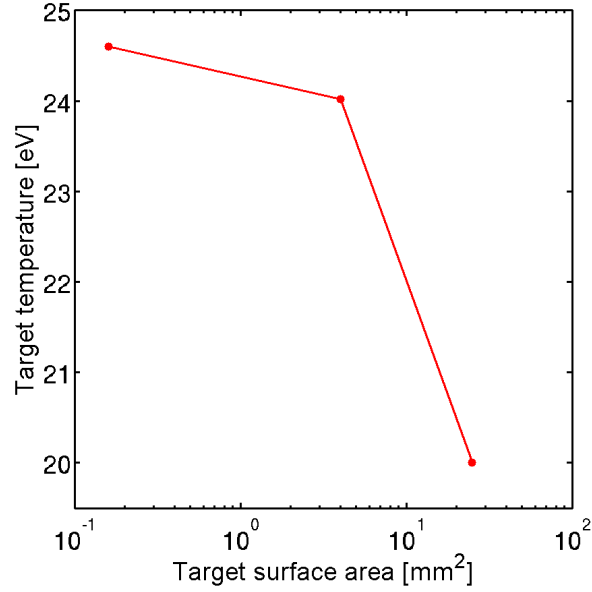
Figure 6.9: Inferred target temperature as a function of surface area obtained by comparing the Fig. 6.7 and Fig. 6.8 (b).

refluxing electrons reaching the target edge are radially reflected, i.e. there is no change in the direction of the velocity vector. However, if the target has linear edges then the electrons change direction upon reflection. This results in a non symmetrical distribution of the electron over the target surface creating regions of higher TNSA accelerating field. The expansion of the ion front is greater in these regions. As ions are accelerated along the local normal direction to the ion front, regions of large field gradient give rise to larger ion beam divergence and vice versa. The resulting ion beam spatial distribution can therefore in principal be controlled by engineering the target geometry. For this to occur the target lateral dimensions must be small enough such that the refluxing electrons can 'shape' the accelerating field while the acceleration is still occurring. This technique is demonstrated for the first time here using different target geometries (disk, square and triangle) as shown in Fig. 6.1 (a-c).

6.5.1   Experimental results

Examples of the measured lower half of the proton beam are shown in Fig. 6.10 (a-c). A direct correlation between the shape of the target, represented in the insets, and the 'shape' of the experimental proton beam is observed. A circular beam is

produced by the circular target in Fig. 6.10 (a). The square target, Fig. 6.10 (b), produces a square beam rotated by 45° with respect to the target orientation. The isosceles triangle target, Fig. 6.10 (c), produces an asymmetrical triangular beam with the apex pointing in the opposite direction of the apex of the target.
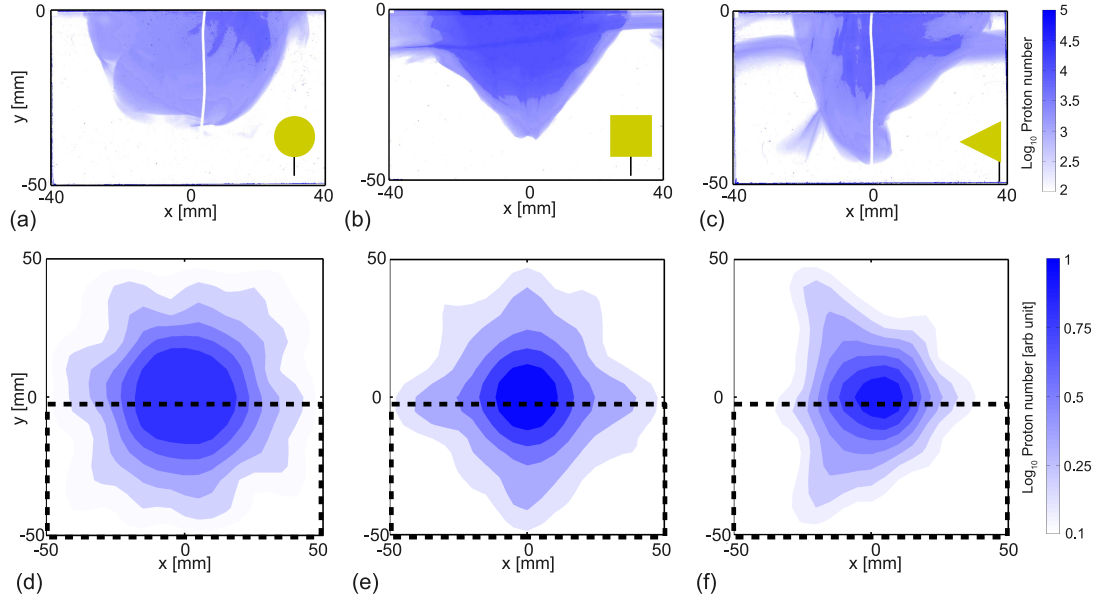
Figure 6.10: (a-c) Measured proton beam spatial intensity distribution (lower half) for different target geometries (shown in the inset) at $\simeq 6$ MeV. (d-f) Proton beam spatial intensity distribution obtained from the model discussed in the main text for corresponding target shapes. The dotted box represents the portion of the beam detected by the RCF stacks in the experiment.

6.5.2 Modelling the electron motion

To determine if the proton beam 'shape' can be explained by the transverse refluxing, the dynamics of the hot electrons was modelled. A 2D model was developed to calculate the dynamics of the hot electrons on the target surface and infer the proton beam 'shape' via calculation of the temporal evolution of the electrostatic field spatial distribution. To perform this the hot electron motion on the target rear surface is tracked. The electrons emerge from a region on the rear surface of radius equal to the laser spot radius and are given a random propagation direction. The electrons then travel radially along the surface at a constant velocity of $0.75c$ until they reach the target edges, where they undergo a simple specular

reflection. The number of electrons generated increases with the rising edge of the Gaussian laser pulse and decreases exponentially after the peak of the pulse [174]. The total number of electrons (at the end of the laser pulse) is given by:

$$N_e = \frac{\eta_{L \to e} \mathcal{E}_L}{k_B T_e} \tag{6.2}$$

where $\eta_{L \to e}$ is the laser to hot electrons conversion efficiency and $\mathcal{E}_L$ is the laser energy. Ponderomotive scaling [62] is used to determined the value of $k_B T_e$. The total number of electrons $\sim 10^{14}$ for $\mathcal{E}_L = 140$ J and $k_B T_e = 1$ MeV. It is impossible to trace the trajectories of such a large number of particles using a computational software package such as Matlab. Therefore, macro particles, each of which consists of 10^{10} electrons were introduced. Interactions between the particles were not included in the model. A typical trajectory of one of the macro particles is shown in Fig. 6.11.
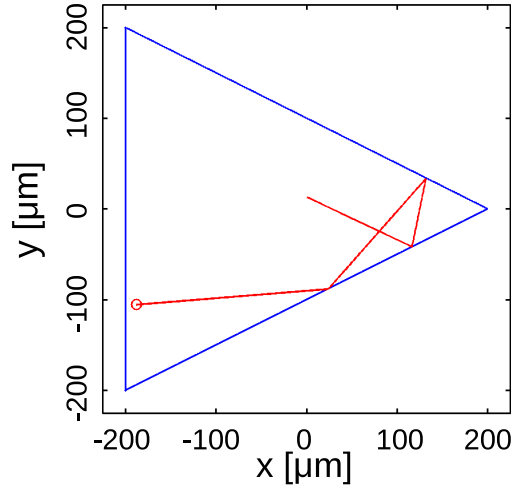
Figure 6.11: Example of the typical trajectory of a macro particle on the surface of an isosceles triangular target. The electron starts around (0,0) and the circle represents the position of the particle at the end of the calculation.

The positions of the particles are updated at each time step and used to generate the spatial distribution of the hot electron density. The total calculation time is 2.6 ps with time steps of 260 fs. The density is calculated on a grid with cell size 1 μm$\times$1 μm. Gauss' law is used to obtain the value of the component of the electric field directed along the target normal direction at different positions

along the target surface. The model is run repeatedly for the three different target shapes used and the results are shown in Fig. 6.12.

For all the target shapes investigated the electric field distribution is the same at early times. It is only modified after the hot electrons have reached the target edges and are reflected. In the case of the square (Fig. 6.12 (b)) and triangular (Fig. 6.12 (c)) targets, the presence of corners on the target introduces region of higher electric field. This is due to the longer time that the hot electrons spend at the corners due to the multiple reflections they undergo. This creates regions of sharp electric field gradient. This is not observed in the case of the circular target where the absence of corners make the reflections of the hot electrons symmetrical.

Evidence of the enhanced electron density at the corners of the target can be seen in the images obtained using the broadband X-ray pinhole imaging camera. An example of the time integrated X-ray emission is shown in Fig. 6.13 (b) where regions of bright emission can clearly be distinguished at the edges of the target and at the corners in particular. The Kα emission from a triangular target shown in Fig. 6.13 (c) clearly reproduces the geometry of the target. This is in good qualitative agreement with the results presented in Fig. 6.12 (b-c) and supports the model discussed in this section.

Using the time evolution of the electric field on the target surface, the resulting proton beam 'shape' can be modelled. It is assumed that the dominant ionisation mechanism is field ionisation [110, 160]. The 3D profile of the proton front is calculated assuming that the expansion of the front only occurs along the target normal direction. When the calculation has finished, the protons are assumed to propagate along the local normal direction to the final proton front. The final position of the protons is recorded when they have reached the detector plane. This procedure enables spatial intensity distribution maps of the beams to be generated as shown in Fig. 6.4 (d-f). The modelled proton beam 'shapes' are in good agreement with the experimental results, as shown in Fig. 6.4 (a-b). Specific features of the experimental proton beam are well reproduced. The 45° rotation of the proton emission in the case of the square target is reproduced. The
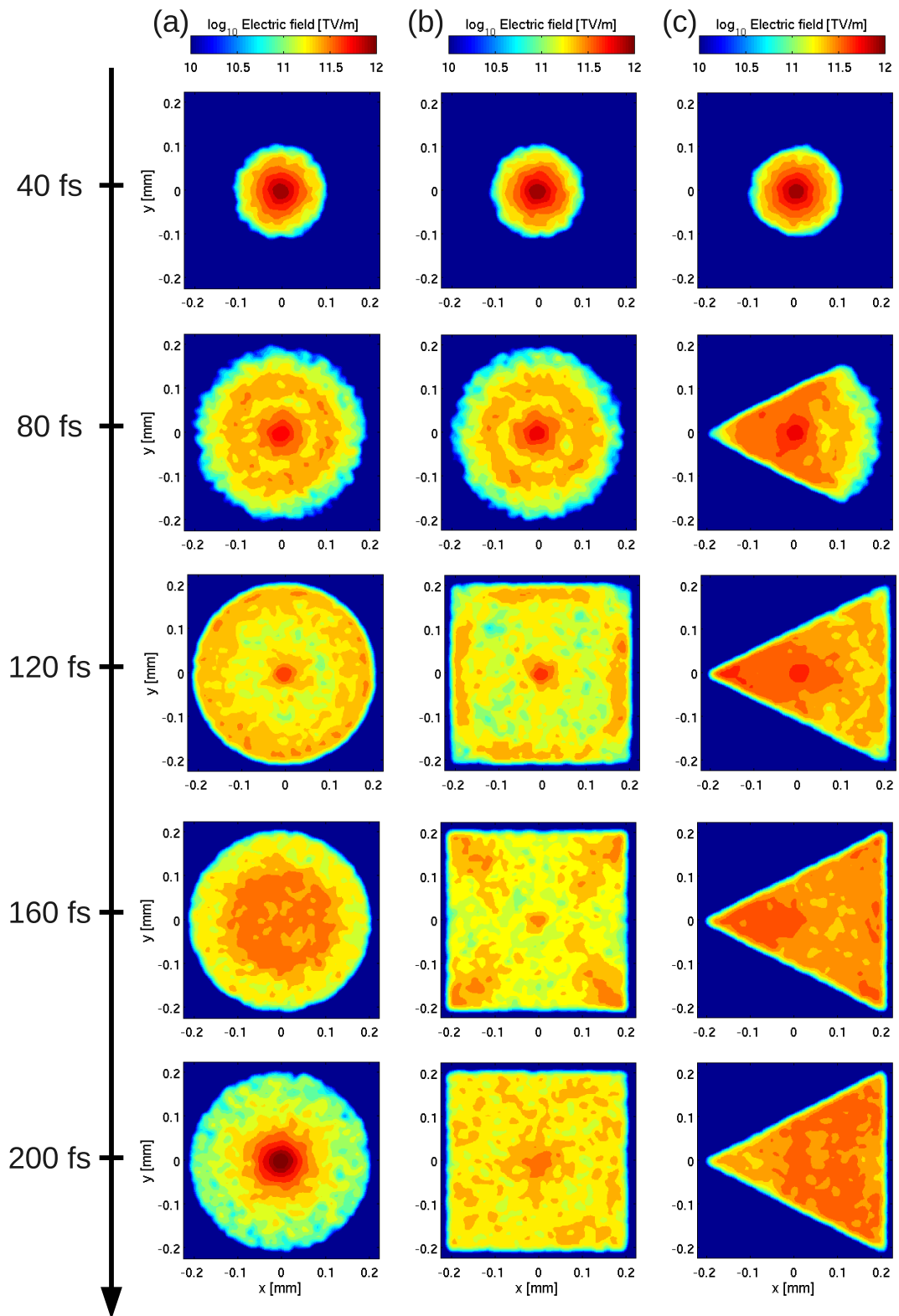
Figure 6.12: Modelled 2-D spatial distribution of the electric fields at given times for (a) a circle, (b) a square and (c) a triangular target geometry.
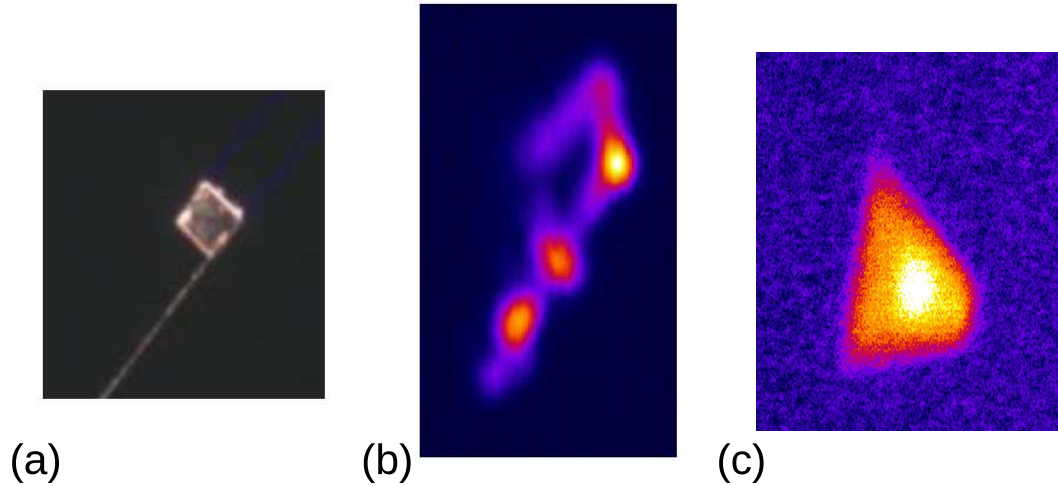
Figure 6.13: (a) Photograph of a square target (100 μm$\times$100 μm) before laser irradiation. (b) Time integrated X-ray emission from the same target recorded using a pinhole camera (viewed from a slightly different angle). (c) Example of the Kα emission from a triangular target recorded with the Cu Kα imager.

change in orientation of the apex of the triangular proton distribution compared to the target orientation is also clearly reproduced. These unusual beam 'shapes' are explained by the irregular electric field gradient [113] caused by transverse refluxing from shaped targets. For these proton beam 'shapes' to be observed experimentally the target must be of a small enough size such that the transverse refluxing occurs while ions are still being accelerated.

6.6 Conclusions

In this chapter new experimental and numerical results on the influence of the laterally refluxing hot electrons on the properties of TNSA-accelerated protons are presented. Confirmation of the important role played by these electrons in ultra intense laser foil target interactions is provided. Results confirming the role of the laterally refluxing hot electron in the enhancement of the maximum energy of TNSA-proton with decreasing target surface area, as inferred in earlier work, are discussed. Novel measurements of the proton emission from the target edges have been made, confirming the existence of a laterally spreading electron population.

A method of inferring the variation of target temperature from the change

in intensity of a Kα imager is presented and it is found that, in agreement with previous work, the temperature increases with decreasing target surface area. Differences in the estimated temperatures between this work and previous results can be explained by the different targets and laser parameters used.

Furthermore, it has been demonstrated for the first time, both experimentally and analytically, that the laterally refluxing hot electrons can be constructively used to tailor the 'shape' of the TNSA-proton beam by engineering the geometry of the target. This approach is particularly interesting for the many envisaged applications where the 2D profile of the proton beams has to be controlled.

Chapter 7

Characterisation of debris generated in high power laser-solid interaction

7.1 Introduction

As discussed in chapter 2 the interaction of a high power laser pulse with a solid target results in ablation and launches a shock wave into the material which emerges at the rear surface. The vaporisation, ionisation and decompression of the target results in significant debris generation. The deformation of the target rear surface induced by the shock wave is responsible for part of the debris emission. The debris generated is typically liquid or gaseous, depending on the laser and target parameters. Solid shrapnel is also present in the ejecta plume.

Understanding shrapnel and debris production in the interaction of ultra-intense laser pulses with solid targets is essential to prevent damage to expensive optics and components positioned close to the target region. Fig. 7.1 for example shows damage caused by debris to an expensive focussing parabola on an experiment using the VULCAN laser.

In recent years experimental studies of debris generation have been performed at laser intensities in the range 10^{12}-10^{14} Wcm^{-2} with metallic targets by Lescoute *et al.* [175–177]. They irradiated the targets with a large laser focal spot ($\sim$100

133
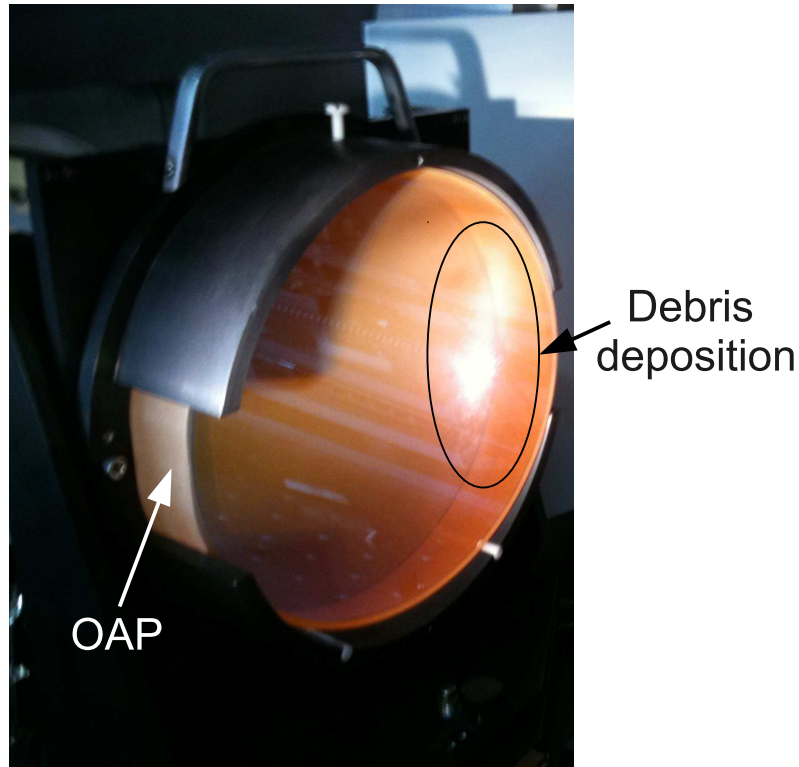
Figure 7.1: Example of debris deposition on an off axis parabola (OAP) resulting from a single high power laser solid interaction.

μm to 1 mm radius) to produce a homogeneous 1D shock wave inside the target [178]. The shrapnel emission was recorded using gel cells and particulate with size ranging from hundreds of microns to a few millimetres were measured. Similar investigations have been carried out at higher laser intensities ($\sim 10^{20}$ Wcm^{-2}) by Andrew *et al.* [179–182]. In addition to shrapnel Andrew *et al.* observed, gaseous, liquid and particulate debris, with sizes ranging from a few tens of nanometres to hundreds of microns.

Shrapnel constitutes the main danger to the focussing optics and other sensitive components placed near the interaction region as the particle impact has the ability to irreversibly damage optics by creating cracks and craters [179–182]. Relatively small optics can be protected by the use of debris shields or sacrificial mirrors. The debris shield usually consists of a 2-3 mm-thick glass plate, placed in front of the focussing optic in order to collect the debris emitted from the target [179]. Debris shields can be used more than once, but as the debris accumulates on the glass the transmission of laser energy and quality of the laser

focal spot are reduced. Thinner (tens of microns) polymer films can also be used to protect the focussing optics, but only from the smaller debris particulates. These techniques generally don't work with large optics such as the 1 m diameter optics used in the VULCAN TAP, due to the difficulty in producing debris shield with the required uniformity not to distort the laser beam. The use of sacrificial mirrors, such as plasma mirrors, enables the focussing optics to be placed outside of the debris emission cone, thereby reducing their exposure to shrapnel.

In this chapter, a characterisation of the debris emitted from the front and rear surfaces of solid target foils irradiated with pulses from the VULCAN laser is discussed. The chapter begins with the characterisation of the debris emission direction for ultra-thin (100 nm) targets. In the second part, the influence of the target thickness on the rear surface emission is investigated both experimentally and analytically. Finally a qualitative discussion on debris emission from layered targets and secondary sources is given.

7.2   Experimental measurements

The debris characterisation results presented in this chapter were obtained in situ as a secondary diagnostic as part of an experimental campaign using the VULCAN laser investigating fast electron transport and proton acceleration from solid targets. The VULCAN laser, described in chapter 4, generates pulses of light at a wavelength of 1.054 μm with a duration of 0.7 ps. For the results presented in this chapter the pulse energy on target was 130 J, in a 3.8 μm radius spot (FWHM), giving an intensity of 4×10^{20} Wcm^{-2}. The laser incident angle was varied between 0° and 15° by rotating the target. A plasma mirror was positioned 3 cm from the target front surface to enhance the intensity contrast of the laser pulses, as described in chapter 4. Debris emission from different target materials was investigated, including plain 100 nm-thick Cu foils and layered targets of Al-Cu-CH with thicknesses varying from 527 μm up to 1007 μm.

As shown in Fig 7.2 (a), the debris emitted from the front surface was collected using the plasma mirrors, position 'A' in Fig 7.2 (a), and the debris emitted
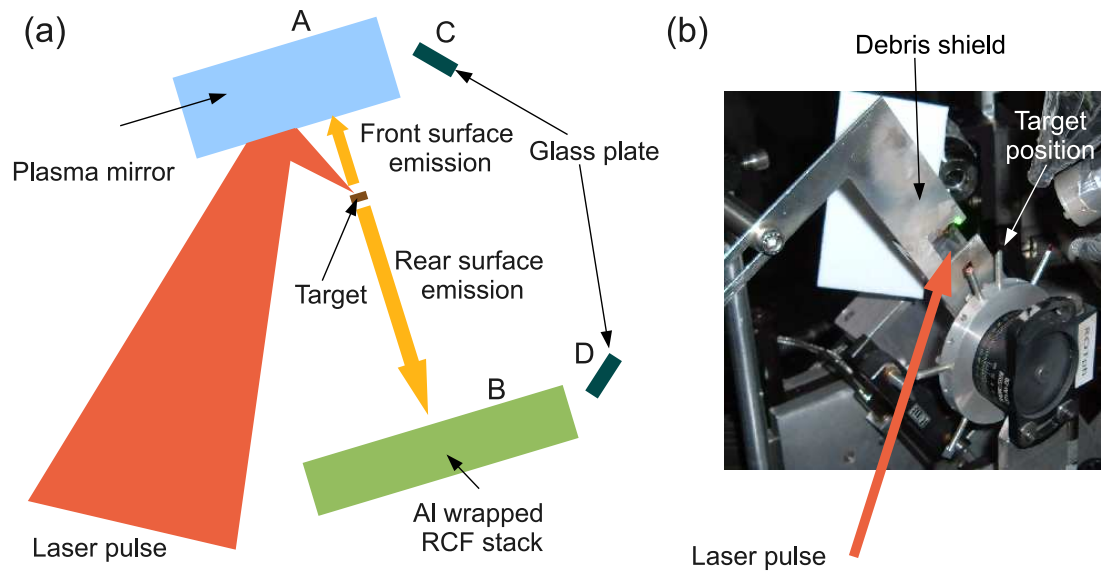
Figure 7.2: (a) Schema of the experimental setup. (b) Photograph of the setup showing the debris shield placed in front of the plasma mirror.

from the rear was collected using the aluminium foil used to protect the RCF (dosimetry film) stacks, position 'B' in Fig 7.2 (a). The plasma mirrors are AR-coated glass slabs of 2 cm by 10 cm, positioned 3 cm from the front of the target. A shield was placed in front of the plasma mirror to protect the unused surface from the debris emitted from the target as shown in Fig 7.2 (b). The aluminium shield positioned in front of the RCF stack is a 13 μm thick foil. It is positioned 5.3 cm from the target rear and the exposed area is 2.5 cm×5 cm. In addition, glass witness plates were positioned 5 cm from the target to capture debris emitted in the laser specular direction, 'C' in Fig 7.2 (a), and in the laser forward direction, 'D' in Fig 7.2 (a). The distribution of debris on the Al foil, plasma mirror and witness plates was characterised using a flat-bed optical scanner operated in reflection mode.

7.3 Front surface debris emission

Debris is consistently observed in positions 'A' and 'B', but no significant debris emission was recorded in directions 'C' and 'D' for any of the laser shot taken, indicating that the main debris emission occurs along the target normal direction

both at the front and at the rear surface.
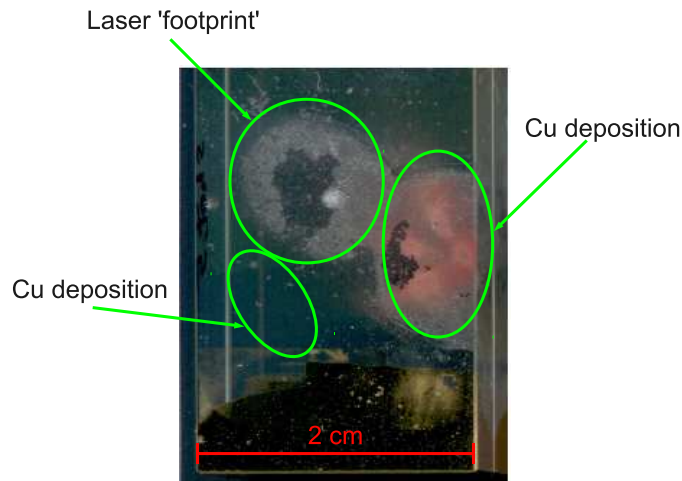
Figure 7.3: Debris deposition on the plasma mirror from 100 nm thick Cu foils. The debris deposition and the laser imprint are highlighted.

To confirm this, the incidence angle of the laser on the target was varied between 0° and 15°. The targets (plain 100 nm Cu foils) were simply rotated and the position of the debris deposition measured with respect to the normal incidence case. The resulting debris deposition consisted of Cu coating an area of diameter ∼1 cm as shown in Fig 7.3. The expected position of the debris deposition on the plasma mirror is also calculated assuming that the debris is emitted along the target normal direction, with the position of the debris distribution on the plasma mirror in the normal incidence case used as a reference. As can be seen in Fig. 7.4 (a), the debris emission is predominantly along the target normal direction.

Similar emission patterns have previously been observed experimentally using low intensity (10^7-10^8 Wcm^{-2}) long (tens of ns) laser pulses [183–185] and is typical of an isentropic adiabatic expansion of a plasma plume in vacuum. The expansion of the plume is driven by the plasma density gradient at the target front surface [185]. The largest gradient is in the direction normal to the target and therefore the expansion of the plasma plume is fastest in this direction, resulting in debris emission directed along the target normal, in agreement with results shown in Fig. 7.4 (a).

Fig. 7.4 (b) shows the divergence half angle of the debris particulate emission along the vertical and horizontal axis. The debris particulate emission half angle
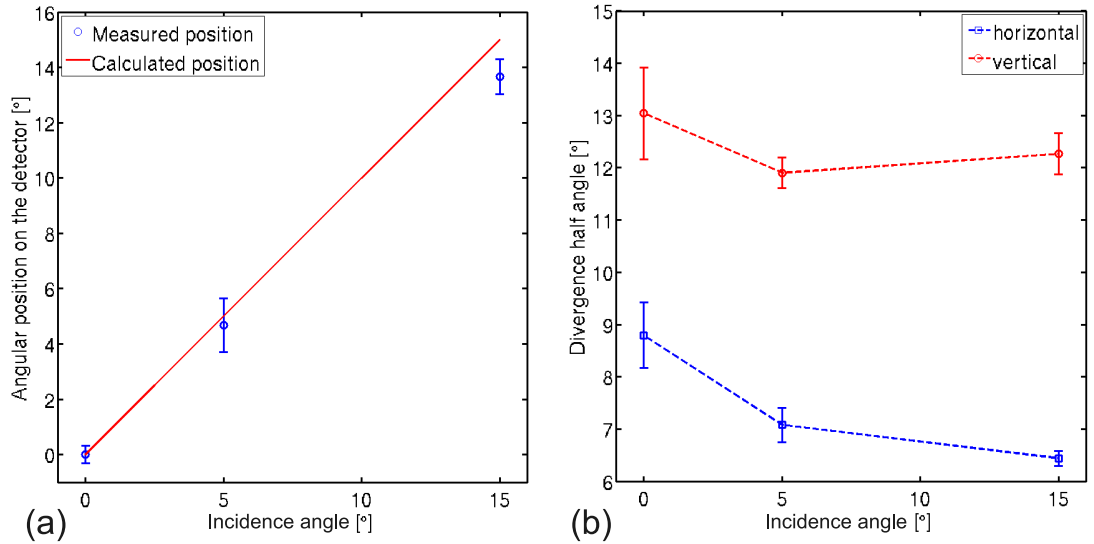
Figure 7.4: (a) Comparison of the measured position of the debris deposition on the plasma mirror (blue) with the calculated position assuming the emission is along the target normal direction (red). The positions are calculated with respect to the normal incidence case. (b) Measured divergence half angle of the debris emission in the vertical direction (red) and horizontal direction (blue) for varying laser incidence angle. In both (a) and (b) the errorbars represents the standard deviation over a number (10) of measurements of the debris particulate deposition.

in the horizontal axis is found to decrease when the laser incidence angle increases, while the half angle in the vertical axis does not vary significantly. The broadening of the debris particulate deposition in the horizontal axis may be explained by the increase of the laser focal spot at larger incidence angle. For oblique incidence the laser focal spot is stretched in the horizontal direction, resulting in a lower density gradient and therefore a smaller divergence angle.

7.3.1 Numerical modelling of the front surface plasma expansion

Anisimov *et al.* [186] have developed an analytical model of the expansion of a neutral gas cloud into vacuum. Dogget *et al.* [185] have shown that this model can also be used for laser generated plasma, if the influence of the charge separation on the expansion dynamic can be ignored.

The Anisimov model assumes an isentropic and adiabatic expansion of a single species vapour cloud into vacuum. The solutions of the gas dynamic equations are

found in the case of a self-similar flow. The formation time of the vapour cloud is assumed to be much smaller than its expansion time. This is the case in laser solid interactions as the ionisation occurs over a femtosecond to picosecond time scale, whereas the expansion occurs over a nanosecond time scale. The initial transverse size of the cloud is considered equal to the laser focal spot, which is assumed to have an elliptical shape with semiaxes X_0 and Y_0. The initial expansion of the vapour cloud in the Z-axis is $Z_0 \approx c_s \tau_L$, where c_s is the sound speed in the vaporised material and τ_L is the pulse duration.

The equations governing the gas expansion dynamics are [186]:

$$\frac{\partial \rho}{\partial t} + \nabla \cdot (\rho v) = 0,$$
$$\frac{\partial v}{\partial t} + (v\nabla)v + \frac{1}{\rho}\nabla p = 0, \qquad (7.1)$$
$$\frac{\partial S}{\partial t} + v\nabla S = 0$$

where S, v, p and ρ are the entropy, velocity, pressure and density of the gas, respectively. The gas is assumed to expand in a 3D ellipsoid and the dynamic equations can be rewritten as a set of simple differential equations:

$$\frac{\partial^2 X}{\partial t^2} = -\frac{\partial U}{\partial X},$$
$$\frac{\partial^2 Y}{\partial t^2} = -\frac{\partial U}{\partial Y},$$
$$\frac{\partial^2 Z}{\partial t^2} = -\frac{\partial U}{\partial Z}, \qquad (7.2)$$
$$U = \frac{5\gamma - 3}{\gamma - 1}\frac{\mathcal{E}_p}{M_p}\left(\frac{X_0 Y_0 Z_0}{XYZ}\right)^{\gamma-1}$$

where γ is the ratio of specific heats, $\mathcal{E}_p$ is the plume thermal energy and M_p its mass. Using Eq. (7.1) the particle flux at a point (x_p, y_p, z_p) in the expansion direction (along the z) is given by:

$$F(z_p, t) = \rho(x_p, y_p, z_p, t)v_z(x_p, y_p, z_p, t) \qquad (7.3)$$

where $v_z(x_p, y_p, z_p, t) = (z_p/Z)\partial^2 Z/\partial t^2$, and Z and $\partial^2 Z/\partial t^2$ are found by solving

Eq. (7.2).

In the limit of a constant plume expansion velocity, the time t_f when the plume front reaches the detection plane at the distance R defined as:

$$t_f = \frac{R\sqrt{1 + k_x^2 \tan^2 \phi}}{(dZ/dt)\sqrt{1 + \tan^2 \phi}} \tag{7.4}$$

where k_x is the ratio of the semiaxes in the x-z plane ($k_x = Z/X$) and ϕ is the angular position in the x-z plane. The particle flux on the detection plane can then be expressed, in units of t/t_f, as [185]:

$$F\left(\phi, \frac{t}{t_f}\right)\frac{dt}{t_f} \propto \frac{M_p k_x^2}{R^2}\left(\frac{1 + \tan^2 \phi}{1 + k_x^2 \tan^2 \phi}\right)^{3/2}\left(\frac{t_f}{t}\right)^4\left[1 - \left(\frac{t_f}{t}\right)^2\right]^{1/(\gamma-1)}\frac{dt}{t_f} \tag{7.5}$$

A similar equation can be defined in the y-z plane simply by replacing k_x with $k_y = Z/Y$.

Integrating Eq. (7.5) from the time t_f to infinity gives the analytical expression of the normalised flow of particle per unit area as a function of ϕ [185]:

$$\frac{f(\phi)}{f(0)} = \left(\frac{1 + \tan^2 \phi}{1 + k_x^2 \tan^2 \phi}\right)^{3/2} \tag{7.6}$$

As stated previously, Dogget *et al.* [185] have shown that the Anisimov model can be used to describe the expansion of a partially ionised plasma plume created using a low intensity (6×10^7 Wcm^{-2}) laser pulse focused onto a thick (3 mm) silver target. In the work presented in this chapter the peak laser intensity is 4×10^{20} Wcm^{-2}. However, the laser intensity drops rapidly in the wings of the focal spot, and intensities $\sim6\times10^7$ Wcm^{-2} are found at approximately 10 times the focal spot radius, considering a Gaussian spatial profile. Therefore it implies that most of the debris particulate will result from the interaction of a low intensity laser with the target surface and the expansion model by Anisimov *et al.* [186] may be used to describe the debris expansion.

Fig. 7.5 shows a comparison of the measured debris deposition on the plasma mirror (dashed blue line) with results of the Anisimov model from Eq.(7.6) (solid

red line). A qualitative estimation of the debris deposition can be obtained by performing a spatially resolved measurement of light reflected off the debris deposition. Using a black background, higher density of Cu deposition are expected to reflect a larger amount of light giving rise to a higher pixel value. Therefore this gives an indication of the quantity of debris deposited on the plasma mirror. The Anisimov model result is normalised to the experimental data and is in good agreement with the experimental data.
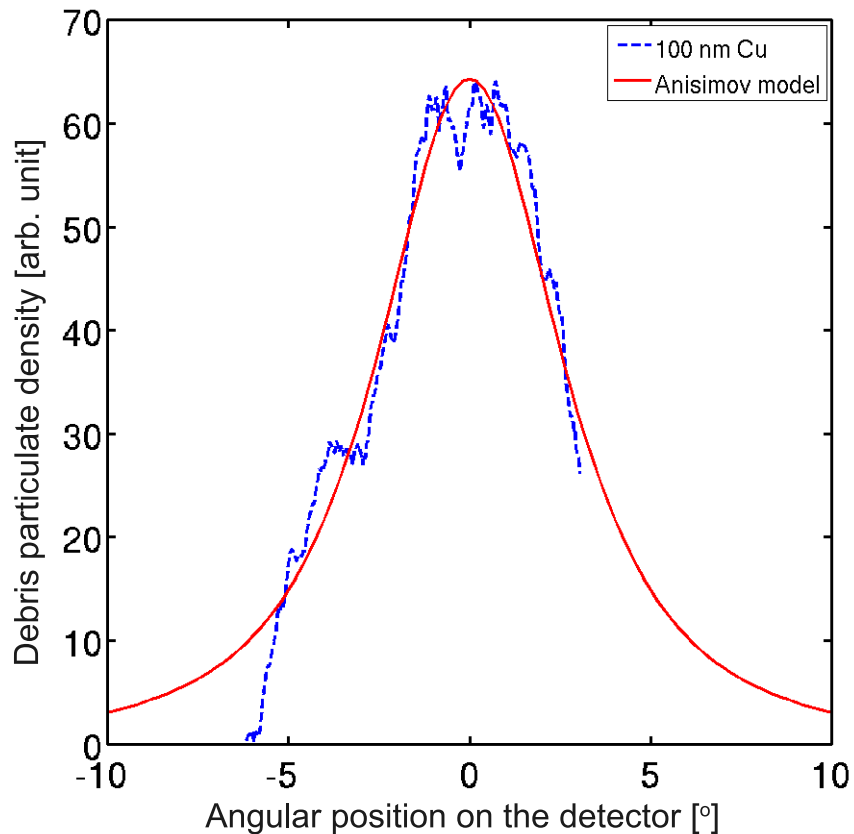
Figure 7.5: Debris particulate density as a function of angle with respect to the target normal axis. The normalised distribution calculated using the Anisimov model is also presented for comparison.

As seen in Fig. 7.4 the debris emission recorded on the front surface exhibits similar characteristics to a plasma plume expansion [185]:

- expansion peaked in the target normal direction;

- increase of the expansion divergence with decreasing laser spot size

- broader expansion in the direction of the smaller laser spot dimension

Furthermore, the gas plume expansion model developed by Anisimov *et al.* [186] gives results in good agreements with the experimental measurements as seen in Fig. 7.5. This indicates that the debris particulate emission from the target front surface, mostly due to the low intensity wings of the laser spot, is governed by the expansion of the laser generated plasma plume.

7.4 Influence of target thickness on the debris emission

Next the influence of the target thickness on the rear surface debris emission, direction 'B' in Fig. 7.2 (a), is investigated. The targets used consist of three layers of different material, Al, Cu and CH. The thickness of the front layer of Al is varied and is equal to 20, 100 or 500 μm. The Cu and CH layers have a constant thickness of 7 and 75 μm, respectively. This results in targets with total thicknesses of 527, 607 and 1007 μm. The target composition was determined by other scientific objectives (investigation of fast electron transport in solids), but enables the investigation of thickness and target layering effects on debris generation.

7.4.1 Spatial distribution of emitted debris

Fig. 7.6 (a-b) shows the position of the debris impact on the Al foil used to protect the RCF films, and clearly shows a hollow (ring-like) distribution. This debris particulate distribution is observed for all three target thicknesses used. Only half of the emission is recorded to allow a line of sight for other diagnostics. The central region, containing only a small number of impacts is extending over a radius of ∼1.5 cm and centred on the target normal direction. The debris is deposited over a width of ∼0.5 cm with most of the debris particulate found in the top region of the distribution.

As shown in Fig. 7.6 (b) the distribution of debris particulate impact can be fitted with a parabolic function. The red solid line represents the best fit to the
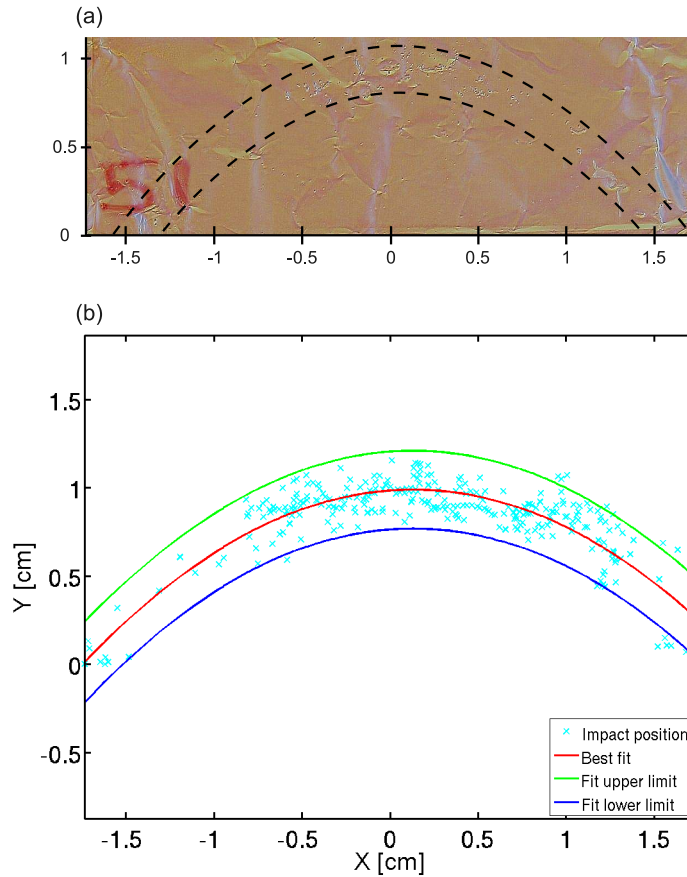
Figure 7.6: (a) Example of an Al foil exposed to debris emission from a 527 μm thick Al-Cu-CH target. (b) Parabolic fit applied to the debris particulate impact distribution (cyan symbols), the blue and green lines correspond to area containing 95 % of the impacts, while the red line represents the best fit. The position (0,0) corresponds to the target normal position.

data, while the green and blue lines represent the boundaries of the width of the distribution containing 95% of the debris impact. The debris particulate observed with this type of target seems to mainly result from liquid debris, as some of the craters formed are filled with solidified liquid droplets. The material embedded in the Al witness foil is most likely molten CH from the back surface of the target.

Experimentally it is found that the diameter of the debris deposition, d_d, increases with increasing target thickness, as seen in Fig. 7.7. The increase of d_d is explained by the spherical shock wave propagating inside the target material leading to an increase in d_s when the target thickness increases. θ_d is assumed to be independent of target thickness. An approximate fit to the experimental data is obtained using Eq. (7.7) $\theta_s=80°$ and a divergence of the debris cone $\theta_d=14.5°$

for the lower limit, 19.5° for the upper limit and 17° for the best fit. The angle needed to fit the whole distribution is 17° ± 1.3°.
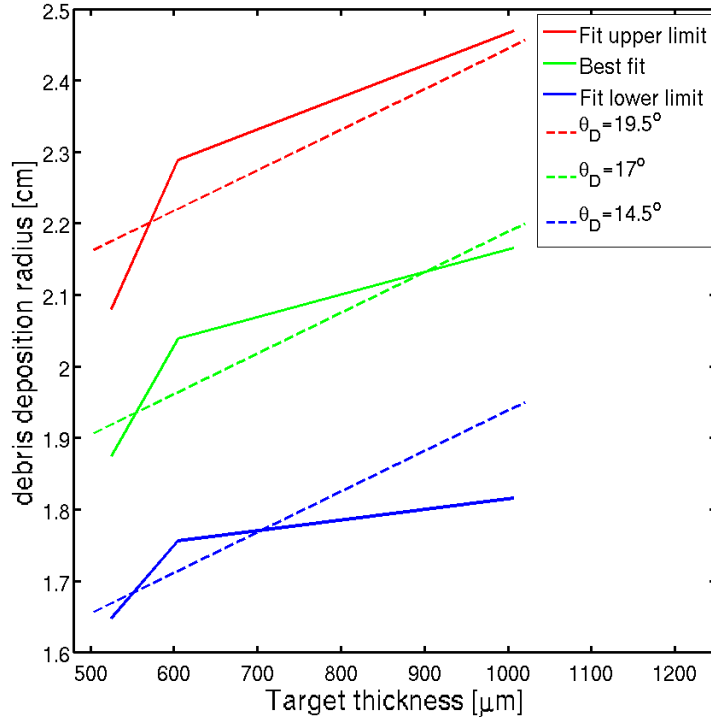
Figure 7.7: Variation of the debris deposition radius with varying target thickness for the best fit to the data (green) and the lower (blue) and upper (red) limit of the 95% fit. The dashed line represents the size obtained using Eq.(7.7).

The diameter of the debris distribution is given by:

$$d_d = d_f + 2L \tan(\theta_s) + 2D \tan(\theta_d) \tag{7.7}$$

where d_f is the diameter of the laser focal spot, L is the target thickness and D is the distance between the target rear surface and the detection plane, as shown in Fig. 7.8.

Modelling of the debris emission

Distributions such as the one shown in Fig. 7.6 (a-b) have not been observed in the previous debris characterisation studies carried at similar or lower laser intensities. In most of the debris studies conducted so far, the laser focal spot is chosen such that a planar shock wave propagates inside the target [178]. The small
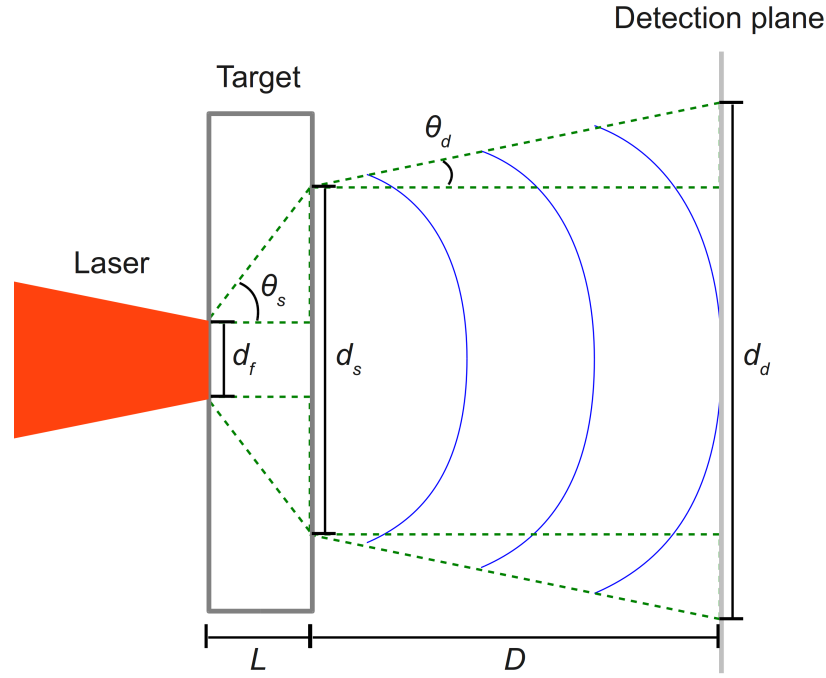
Figure 7.8: Schematic illustrating the propagation of the debris front (blue line) from the target rear surface to the detector plane.

size of the laser focal spot used in the present work drives a spherical shock wave inside the target. It is assumed that the deformation of the target rear surface follows the shape of the shock front emerging at the rear surface. Therefore, in the case of a planar shock front the debris is expected to expand normally to the target surface giving rise to a fairly homogeneous debris deposition on the detection plate. By contrast, for a spherical shock front the debris is expected to expand into a cone, giving rise to an inhomogeneous debris deposition. An analytical model of the resulting debris distribution pattern was developed and compared to the experimental measurements.

As discussed in chapter 2, the pressure applied on the target front surface by the laser pulse scales with the intensity of the pulse with a power exponent of $2/3$ ($P \propto I_L^{2/3}$), and the velocity of the shock front, v_s, and the particles, v_p, are functions of the pressure, as follows:

$$v_s = \frac{c_s}{2} \left(\sqrt{1 + \chi} + 1 \right) \tag{7.8}$$

$$v_p = \frac{c_s}{2\alpha} \left(\sqrt{1+\chi} - 1 \right) \tag{7.9}$$

where $\chi = (4\alpha P)/(\rho_0 c_s^2)$ and α is constant depending on the target material.

The spatial distribution of the laser intensity is considered to be Gaussian, with FWHM equal to the experimental focal spot diameter. The magnitude of v_s and v_p follows the same transverse profile as the laser intensity.

In the calculations, the target surface is modelled by 5 000 points with an initial total length of three times the laser focal spot diameter. The shock velocity on each point of the surface is calculated according to the laser intensity spatial distribution, with the laser centred on the (0,0) position. The shock front propagates spherically through the target to the rear surface which starts to expand into the vacuum at the velocity v_{fs} equal to:

$$v_{fs} = 2v_s \tag{7.10}$$

Fig. 7.9 shows the shock induced expansion of the target rear surface into vacuum at given times.

The fraction of the target rear surface that has expanded into vacuum is considered to be the initial debris front. Each point of the debris front then propagates towards the detector in a cone of fixed angle 17° defined using the experimental measurements at the free surface velocity v_{fs} (Eq. (7.10)) [58]. The deposition of debris is evaluated at a given distance from the target rear surface chosen to match the experimental conditions. The position of each point along the debris front is recorded, and plots of the debris particulate deposition profile generated as shown in Fig. 7.10.

For a rear surface expansion of 100 μm (Fig. 7.10 (a)) the debris deposition is peaked at the centre, it flattens when the target rear surface is allowed to expand up to 1000 μm (Fig. 7.10 (b)). For larger rear surface expansion of 2500 μm and 5000 μm (Fig. 7.10 (c) and (d) respectively) the debris deposition is clearly hollowed as measured experimentally. The measured debris deposition radius is reproduced for the largest expansion (Fig. 7.10 (d)) and the lateral extent of the
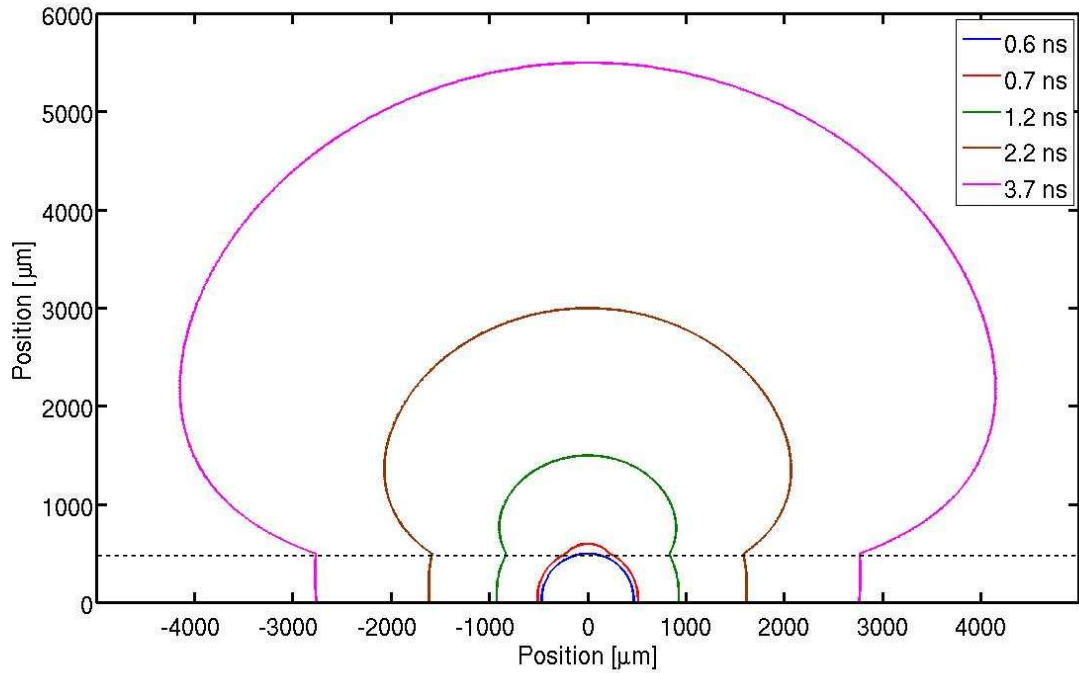
Figure 7.9: Shock induced expansion of the rear surface at given times for a 500 μm thick target. The dotted line represents the initial target rear surface. The laser is incident vertically from the bottom at (0,0).

shock front at the rear surface corresponds to a $\theta_s \simeq 80°$ in good agreement with the results shown in Fig. 7.7.

This indicates that the emission of the debris particulate is governed by the shock induced deformation of the target rear surface. A spherical deformation of the target surface may result in a hollow debris particulate distribution, while a planar deformation (induced by a 1D shock wave) is expected to result in a homogeneous deposition.

7.4.2 Debris size and density

Next the variation of the debris particulate size and density with varying target thickness is investigated. The density of the debris particulate is obtained by counting the number of impacts visible over the whole distribution and divided by the area of the distribution. The size of the debris particulate emitted is estimated by measuring the impacts in multiple sample areas of the Al foil. Fig. 7.11 shows the results of the size and density measurements.

147
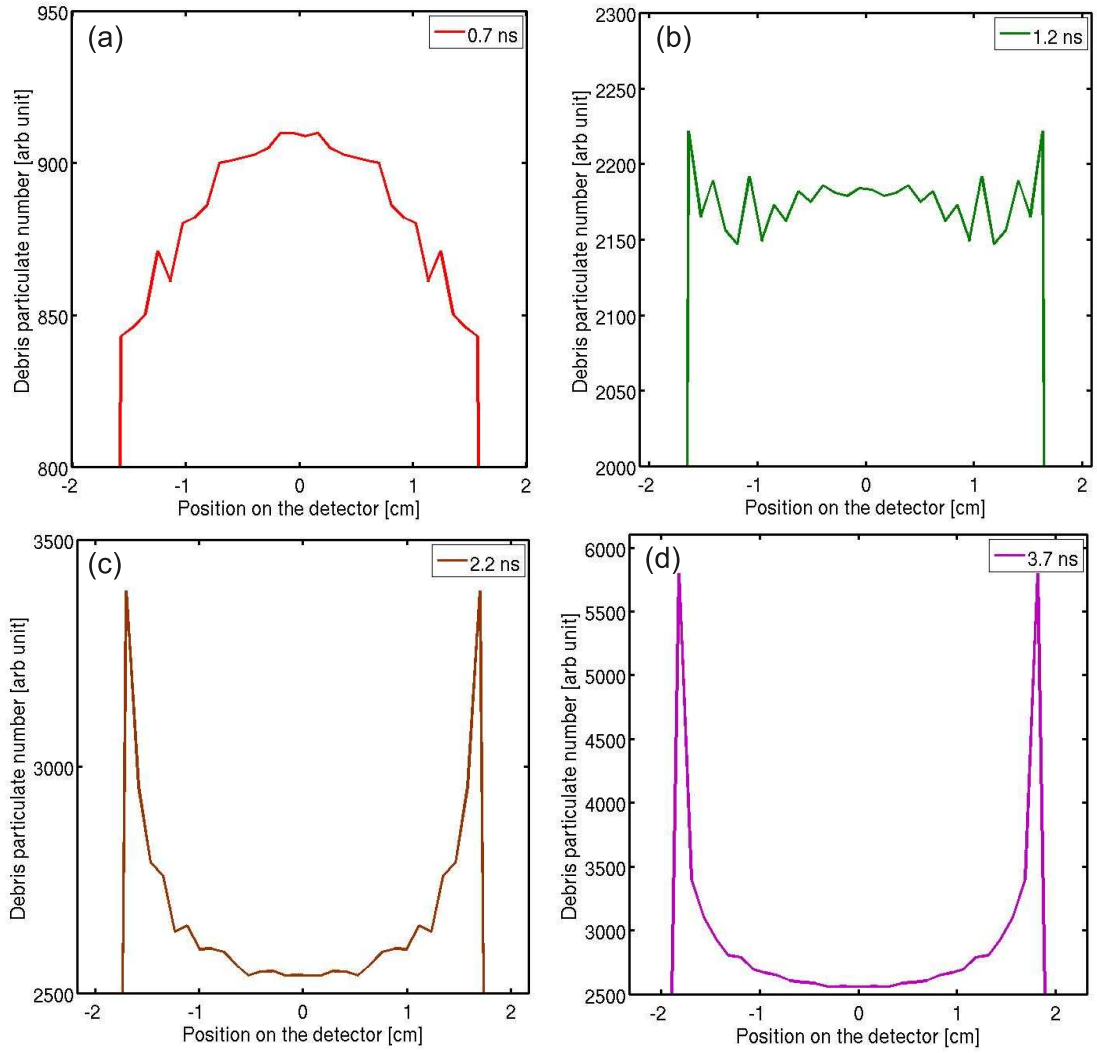
Figure 7.10: (a-d) Debris deposition profile for given rear surface expansion time. (a) 0.7 ns, (b) 1.2 ns, (c) 2.2 ns and (d) 3.7 ns.

The debris deposition density is found to increase with increasing target thickness as shown in Fig. 7.11 (a). The average size of the debris particulates is also found to increase with target thickness, as shown in Fig. 7.11 (b). The resolution of the image limits the size of the debris measurable to above $\sim$90 μm. The increase in debris particulate density can be explained by the larger volume of the thicker targets enabling more material to be ejected towards the Al witness plate. The density deposition of debris particulate ρ_d is defined as:

$$\rho_d = N_d/S_d \tag{7.11}$$

where N_d is the number of debris particulate emitted and S_d is the area of the debris deposition. N_d can be estimated by the ratio of the volume of target transformed into debris, V_t, with the volume of each particulate, V_p. All particulate are assumed to have the same volume. Therefore:

$$\rho_d = \frac{V_t}{S_d V_p} \tag{7.12}$$

V_t is assumed to be equal to the volume between the target rear surface and the expansion into the vacuum. S_d is also found to increase with target thickness as discussed in the previous section. Therefore, to reproduce the increasing trend of ρ_d, V_p must increase. Fig. 7.11 (b) shows the results from the calculation of V_p and the measured average debris particulate size. V_p is found to increase with increasing target thickness as expected, however it is consistently smaller than the experimental measurements. This is probably due to the experimental data being a measurement of the impact of the liquid droplets on the witness foil which can be greater than the radius of the droplet itself.

(a)   (b)
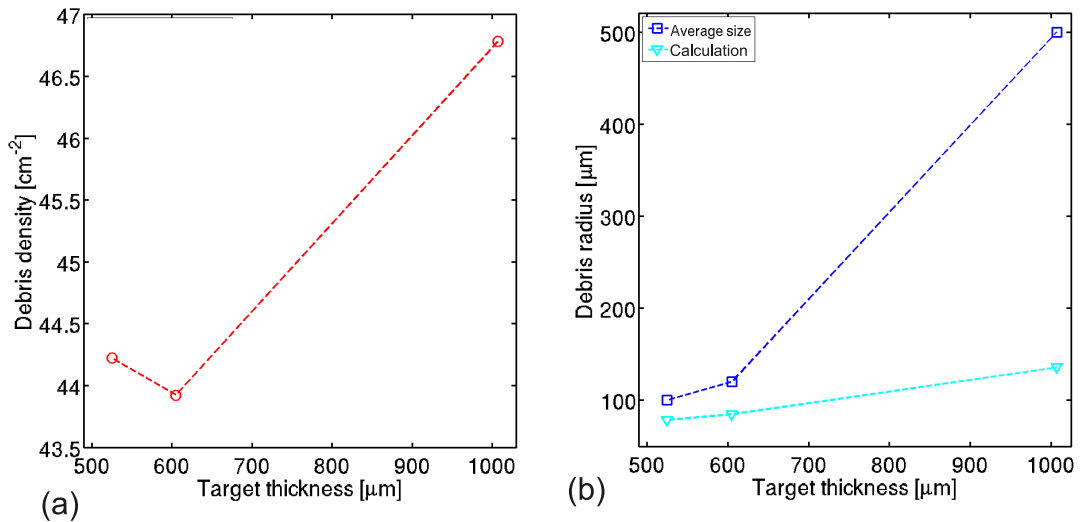
Figure 7.11: (a) Variation of the density of debris particulate deposited on Al witness foil with increasing target thickness. (b) Average size of the debris particulate measured on the Al witness foil (blue) and the results of the calculation described in the main text.

7.5   Ejection of buried layer and secondary debris source

7.5.1   Ejection of the target inner layer

As shown in Fig. 7.12, large pieces of Cu can be found embedded in the Al foil when layered (Al-Cu-CH) targets are used. In this case, the size of the Cu shrapnel is ∼3.6 mm long. The targets used in this work are square foils with lateral dimension of 5 mm×5 mm. Therefore, the Cu found in the Al foil constitute most of the target inner layer indicating that the inner layer survives the interaction of the laser with the target and is ejected at high velocity in the target normal direction. Such acceleration is similar to the flying plates [187] used for shock physics experiments. In that type of experiments the laser is focussed through a transparent substrate onto a layered target of Carbon, Aluminium and Aluminium Oxide layers. The flyer plate is placed on the rear surface of the layer target, and it is launched by the expanding plasma generated by the laser interaction on the layered target.
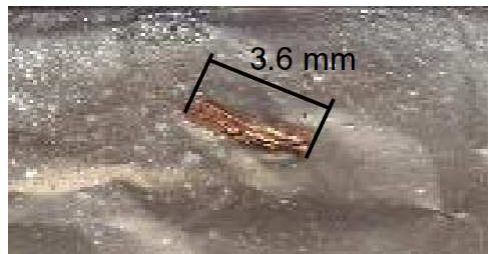
Figure 7.12: Cu shrapnel produced from Al-Cu-CH layered target embedded in an Al witness foil. The size of the shrapnel is ∼ 3.6 mm.

Layered targets are widely used in laser solid experiments and shrapnel of this size can cause a great deal of damage to the most sensitive equipment placed in the target normal direction, thus highlighting the need for debris shielding.

7.5.2   Secondary debris source

During high power laser solid interaction, the main source of debris is the target itself. However, it was observed experimentally that secondary sources can also

exist. As presented in chapter 4, several targets are positioned at the same time inside the interaction chamber. In the case of the VULCAN laser they are placed on a wheel typically holding 5 targets. Similarly, multiple stacks of RCF are placed on a wheel inside the target chamber to enable multiple shots to be fired without having to open the chamber between each shot. The RCF stacks that are not used on a particular shot are protected from protons and X-rays emission using a lead shield.

The survivability of thin targets, in the nm range, proved to be an issue during the experiment. Unused targets placed on the wheel were destroyed during the interaction of the laser with a neighbouring target. Typically only 2 to 3 targets were destroyed during a shot and in some cases all of the unused targets. This unexpected destruction of targets put a great deal of pressure on the experiment, as it takes longer to achieve the desired number of shots, and on target fabrication.

A deposition of lead particulate on the target wheel side facing the RCF stack indicates that the debris particulate originating from the shot target (primary source) hit the lead shield and create a secondary source of debris. The debris particulates originating from this secondary source are believed to be responsible for the destruction of the unused targets. To protect the targets a plastic debris shield (PTFE) was placed on the target wheel facing the RCF stack. The top edge of the shield was placed at the same height as the bottom of the stalk holding the target. The debris shield is shown in Fig. 7.13, with the lead deposition clearly visible. The use of this simple debris shield was sufficient to protect the unused target from the debris emission from the lead shield.

7.6   Conclusion

The emission of debris from a solid target irradiated by a tightly focussed (6 μm diameter) high intensity (4×10^{20} Wcm^{-2}) laser pulse has been investigated. It was found that the emission from the front surface of the target can be described by the expansion of a plasma into vacuum. It is shown to be directed along the target normal direction, and to be contained in a cone of half angle of $\sim$10°. As
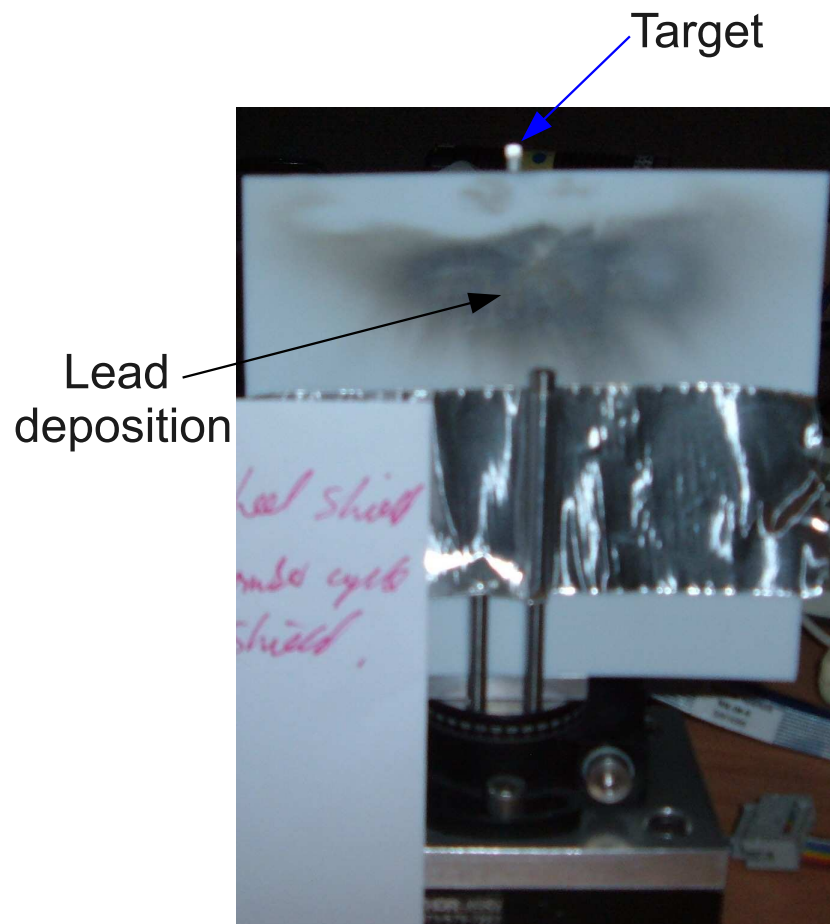
Figure 7.13: Secondary emission of lead particulate collected on a protective PTFE screen over 5 shots.

predicted by the plasma expansion models by Anisimov *et al.* [186] the emission cone increases when the laser focal spot diameter decreases.

The debris emission from the rear surface of the target has also been studied. It was found that the debris is deposited in a parabolic hollow distribution centred on the target normal direction. The hollow distribution is due to the spherical expansion of the target rear surface induced by the shock wave. An analytical model assuming a spherical shock wave propagation was developed and is in good agreement with the experimental data. The radius of the distribution is found to increase with increasing target thickness. This is explained by the propagation of a spherical shock wave inside the target at a fixed angle giving rise to the expansion of a portion of target of larger radius as the thickness is increased. The debris emission is found experimentally to be contained within a cone angle of

∼17°. The size of debris and the number of debris particulate emitted from the target rear surface is also found to be increasing with increasing target thickness. The increase in debris particulate number can be explained by the increase in material available to produce debris when the target thickness is increased.

It was also observed that the whole buried layer can survive the laser interaction and be accelerated forwards in the normal direction. This process is similar to the flying plates used for shock physics experiments. It was also observed that the debris emitted from the target can create a secondary debris source if a soft material, in this case lead, is placed close to the target. The debris particulate originating from this secondary source can result in the destruction of the unused targets placed on the target wheel. To protect them from the secondary emission a simple plastic shield can be used.

Chapter 8

Conclusions and future work

Despite the significant progress made in the past few years, the challenge remains to find new ways of optimising the properties of the ion beams before they can be used for the proposed applications discussed in chapter 1. This thesis presents an experimental investigation of the optimisation of laser driven ion beams in the relativistic laser intensity regime ($I_L > 10^{19}$ Wcm^{-2}). The contribution of this work to the advancement of laser driven ion acceleration is summarised in this final chapter.

8.1   Summary of the main results

8.1.1   Effects of laser incidence angle on ion energy

One of the most interesting result presented in this thesis is the measured effect of the laser incidence angle on ion acceleration, for ultra high contrast laser pulses focussed to intensities above 1×10^{20} Wcm^{-2}. Previous work conducted at lower intensities (5×10^{18} Wcm^{-2}) by Ceccotti *et al.* [65] has shown that higher energy protons are measured when the laser electric field is transverse to the target surface in the case of a high contrast interaction. This is explained by a more efficient laser energy absorption to electrons via the vacuum heating mechanism. This means that in the case of a linearly polarised laser pulse the absorption of laser energy to the fast electrons is more efficient at oblique laser incidence angle.

In addition Ping *et al.* [67] found that the total laser energy absorption fraction for laser intensities between 1×10^{17} Wcm^{-2} and 1×10^{20} Wcm^{-2} is consistently higher at oblique laser incidence that at normal incidence. This confirms the experimental results presented by Ceccotti *et al.* [65]. However, Ping *et al.* [67] also report that for laser intensities $\sim 1 \times 10^{20}$ Wcm^{-2} the fraction of laser energy absorbed by the target is similar for both normal and oblique laser incidences.

The results presented in section 5.6 of this thesis are in stark contrast to the findings presented by Ceccotti *et al.* [65]. Using linearly polarised laser pulses of intensity $\sim 1 \times 10^{21}$ Wcm^{-2} higher ion maximum energies were measured for normal laser incidence than for oblique incidence. This has been consistently measured for different target types over a wide range of thicknesses. The observed increase in ion energy cannot be explained by the change in laser intensity induced by the slightly smaller laser focal spot at normal incidence. The increase in energy is consistent for different ion species indicating that the ion acceleration mechanism (TNSA in this case) is not modified. This has been confirmed by 1D boosted PIC simulations.

This result points to a new laser absorption and electron acceleration mechanism accessible with ultrahigh contrast laser pulses with intensities greater than 1×10^{20} Wcm^{-2}. Baeva *et al.* [162] have recently proposed a mechanism called the Zero Vector Potential (ZVP) mechanism which should be accessible under these conditions. It hinges on the presence of moving zeros in the laser field potential enabling highly efficient electron acceleration. A comparison with the ponderomotive scaling shows that the ZVP mechanism is expected to dominate the hot electron acceleration for laser intensities above $\sim 1 \times 10^{20}$ Wcm^{-2}. The ZVP and ponderomotive scalings were used to estimate the maximum ion energy measured at different laser incidence angle for intensities of 1×10^{19} Wcm^{-2} and $\sim 1 \times 10^{21}$ Wcm^{-2}. It was found that in the lower laser intensity case the maximum ion energy is best reproduced with the ponderomotive scaling, while the ZVP scaling gives the best agreement to the data obtained at the higher laser intensity. Thus the results presented in section 5.6 could be the first experimental signature of this new absorption and electron acceleration mechanism.

8.1.2   Control of the spatial intensity distribution of ion beam

The ability to control the spatial intensity distribution, or 'shape', of a laser accelerated ion beam is required for many of the proposed applications discussed in chapter 1. A number of methods have been explored to achieved this experimentally, including the use of multiple laser pulses [168], complex target geometries [165, 166], RF cavities [167] and changing the shape of the laser focal spot [114].

In section 6.5 it is demonstrated for the first time that the shape of the TNSA proton beam can be modified by changing the shape of planar target foils. A variety of target shapes were investigated including a disk, triangle and square. It is observed that the spatial intensity distribution of the proton beam is strongly dependent on the geometry and lateral size of the target. A circular beam is observed when a disk target is shot, a square beam (rotated by 45° with respect to the original target orientation) when a small enough square target is shot, and a triangular beam (inverted with respect to the original target) when a triangular target is shot. These modifications of the proton beam shape are attributed to the laterally refluxing hot electron population. The electrons spread along the target rear surface and are reflected at the edges and the corners of the target. The electrons which return to the region of the TNSA field increase the duration of the field and therefore the maximum ion energy. By shaping the target the electrons return from the edges at different times giving rise to asymmetry in the field evolution and thereby shaping the proton beam. The dynamics of the laterally refluxing electrons are modelled analytically. From the hot electron density distribution an electric field map is obtained and is used to calculate the resulting proton expansion profile as measured on the detectors. It is found that the model reproduces the experimental results with good accuracy, confirming that the unusual shapes observed are the results of the laterally refluxing population.

In addition to confirming the role of laterally refluxing electrons in enhancing the maximum energy of ions accelerated from mass limited targets as reported

by Buffechoux *et al.* [172], the results reported in section 6.5 demonstrate for the first time that the laterally refluxing electron can be used to engineer the spatial intensity distribution of TNSA generated proton beams. This could prove to be particularly useful for many of the envisaged applications as this is a simple technique to control the ion beam shape.

8.1.3   Debris emission in high power laser solid interactions

Chapter 7 presents a characterisation of debris emission from high power laser solid interaction. Debris generation is a critical issue for any high repetition rate high intensity laser facility, and is of paramount importance when designing facilities for the applications discussed in chapter 1. A very limited number of previous studies of debris generation have been reported. These are generally carried out at lower laser intensity and the debris emission considered to result from a 1D planar shock wave launched inside the target. The limited number of investigations performed at higher laser intensity were mostly focussed on the effect of the debris on the laser optics.

In chapter 7, various solid targets were irradiated with a 1 ps laser pulse at an intensity of 10^{20} Wcm^{-2}, resulting in the propagation of a spherical shock wave inside the target. Different target thicknesses were investigated. The debris emission was collected using a plasma mirror optic positioned in front of the target, and the protective Al foil on the RCF stack at the rear of the target. Glass witness plates were also used to monitor the debris emission in the laser forward and backward specular reflection directions.

It was found that the emitted debris is mostly directed along the target normal at both the front and rear surface. It was also found that in the case of the front surface emission the size of the debris deposition pattern decreases when the size of the laser spot is increased. These two observations demonstrate that the front surface debris follows a similar dynamic expansion as a plasma expanding into vacuum. This is supported by the good agreement found between the exper-

imentally measured debris deposition profile and the results from application of the Anisimov plasma expansion model [186].

Forward directed debris from the target rear surface as a function of target thickness is also reported in chapter 7. An unexpected circular hollow (ring-like) distribution of the debris on the protective Al foil is observed. The measured distribution is reproduce by a simple analytical model which considers a laser generated spherical shock wave propagating through the target bulk and deforming the rear surface. The debris propagates in a cone of fixed angle towards the detector plane. This model is able to reproduce the measured debris distribution with good accuracy and in particular the variation of the debris deposition radius with target thickness. A clear increase in the debris deposition size is observed when the target thickness is increased. This is explained by the spherical shock wave propagating inside the target in a cone of fixed half angle of $\sim 80°$ and a propagation of the debris in a cone of half angle of $\sim 20°$. Once again the model is found to be in good agreement with the experimental measurements. Other results reported for the first time in this thesis include the observation of the acceleration of buried metal layers as a whole, leading to large volumes of shrapnel which can significantly damage nearby optics. These results shed new light on the production of debris in intense laser-solid interactions and will help inform the design of future high repetition rate high power laser facilities.

8.1.4 Enhancing and controlling the ion beam maximum energy

Despite the recent progress made in increasing the maximum energy of TNSA generated ions, further work is needed to reach the energies needed for some of the proposed applications. This is likely to be achieved in a number of ways, for example, by increasing the laser intensity to access more efficient ion acceleration scheme such as RPA, by decreasing the target thickness [93, 151, 152], by using stage proton acceleration [170], by accessing new laser absorption process as discussed in chapter 5 or by using mass limited targets [172, 173] as discussed in

chapter 6.

It was previously found, at laser intensities $\sim 1 \times 10^{19}$ Wcm^{-2}, by Kaluza *et al.* [93] that the maximum ion energy increases with decreasing target thickness. An optimal target thickness, below which the maximum ion energy decreases, exists. The decrease in energy is due to the laser ASE inducing the formation of a density gradient at the target rear surface thereby disrupting the TNSA acceleration. Neely *et al.* successfully showed that by increasing the laser contrast thinner targets could be used. This increase is attributed to the transverse refluxing of fast electron in thinner targets enhancing the TNSA field. In chapter 5 a similar investigation is conducted at laser intensities $\sim 1 \times 10^{21}$ Wcm^{-2} and at ultra-high contrast. A similar increasing energy scaling is found. A decrease of the maximum ion energy is observed for target thinner than 100 nm. This is attributed to a change in the acceleration mechanism as confirmed by the changes observed in the ion energy spectra. This approach is limited by the contrast of the laser pulse. The laser contrast can be improved by the use of plasma mirrors but this results in a consequent loss of laser energy. Therefore alternative techniques to increase the ion energy must be found.

The existence of a laterally refluxing electron population capable of generating secondary ion source at the edges of the target was first reported by McKenna *et al.* [160]. 2D PIC simulations showed that this electron population expands until it reaches the target edges. As no return current can be drawn from the vacuum, a strong electric field forms at the edges reflecting the electrons back inside the target. This field is also responsible for the secondary ion sources detected at the target edges. It was demonstrated by Buffechoux *et al.* [172] that this laterally refluxing electron population could be used to enhance the TNSA acceleration when targets of limited lateral size (from 3 mm down to 30 μm) were used. It is found that the maximum measured proton energy increases with decreasing target surface area for targets smaller than 300 μm. If the lateral extent of the target is small enough the laterally refluxing electrons have enough time to return to the center of the target while ion acceleration is still occurring, extending the field duration and thereby enhancing the maximum ion energy [171].

In section 6.3 the use of targets of limited lateral dimension (from 5 mm down to 100 μm) is investigated. It is found that for a longer pulse duration and larger target sizes as the ones used by Buffechoux *et al.* [172] the increase in maximum proton energy with decreasing target surface area is still observed. The fact that this increasing energy scaling is observed for larger targets is due to the longer laser pulse used in the work presented in this thesis (1 ps compared to 400 fs) giving more time for the laterally refluxing electrons to return to the target centre and enhance the TNSA acceleration whilst the electrostatic field is still present. Measurements of the maximum energy of the proton beam emitted from the edges of the target show a similar increasing trend with decreasing target surface area. 2D PIC simulations were conducted for disk target of varying radius and the results support these conclusions. The estimated maximum proton energy from the simulation results is found to reproduce the measured increasing trend of the maximum proton energy with decreasing target surface area, both at the rear and edges of the target.

8.2   Future work

In the last decade high power laser driven ion acceleration has attracted considerable interest and this is likely to continue as higher power lasers such as the proposed VULCAN-10PW and ELI facilities becomes available. At laser intensities in excess of 10^{21} Wcm^{-2} new acceleration mechanisms, such as RPA, can be investigated in detail. The RPA mechanism is expected to produce near mono-energetic ion beams with energy in the GeV range at $\sim 10^{23}$ Wcm^{-2}. On the other hand, if applications are to be developed in the near future, they will most likely rely on the TNSA mechanism as this the most established mechanism and has been shown to be robust for a very wide range of laser and target parameters. At present TNSA generated ion beams do not fully meet the requirements of real-world applications and optimisation of the beams is still needed. There are numerous research directions that can be taken to expand the work presented in this thesis to achieve this.

An obvious next step is to follow up on the interesting results on the influence of the laser incident angle on the ion maximum energy reported in chapter 5. Higher maximum ion energies were observed when the laser pulse was normally incident on the target compared to the oblique incidence case, and this has been attributed to a higher conversion efficiency of the laser pulse energy into fast electrons. Recent theoretical work by Baeva *et al.* [162] has investigated such a situation and confirmed the existence of a new highly efficient absorption mechanism of the laser energy into hot electrons at normal incidence for ultra short, ultra intense and ultra-high contrast laser pulses. Experimentally this new regime needs to be investigated further and in particular the dependence on the different laser pulse parameters (intensity, duration, energy, contrast) and target density needs to be determined. The angular dependence of this new mechanism also needs to be studied in detail.

The use of mass limited targets for ion acceleration yields the promising prospect of increased ion energies as presented in chapter 6. As suggested, it is the laterally refluxing electron that are responsible for the increased maximum ion energy. Therefore it would be interesting to investigate in detail the relation between the lateral size of the target and the laser pulse duration as it was demonstrated that enhancement in the proton energy can be obtained from larger targets if a longer pulse duration is used. Another approach requiring development involves using the laterally refluxing electrons to establish a secondary electric field for staged ion acceleration.

The engineering of the spatial intensity distribution of the proton beam reported in chapter 6 has very interesting prospects in terms of applications, especially in the medical domain. This could potentially be used to tailor the shape of the ion beam to the targeted tumour resulting in minimal damage to the surrounding healthy tissue. So far, this study has been limited to simple geometrical target shapes and would considerably gain from an extension to more complicated target geometries.

The characterisation of the debris generated in laser solid interaction, as presented in chapter 7 is of crucial importance in the development of high power

facilities. The results presented in this thesis consist of a first step in the understanding of the debris emission from solid target irradiated with high intensity laser pulses and should certainly be expanded to a wider range of laser and target parameters. The dependence of the laser intensity, pulse duration and wavelength could be explored. This work could also greatly benefit from a more systematic study with different target materials. One of the main reasons that little information is available on debris generation is that experimental studies with high power energy laser drivers, such as VULCAN, are limited due to the expense and pressure for access to these facilities. However as high repetition rate ultra-intense lasers come online further work on debris generation will need to be performed to prevent damage of expensive optics and diagnostics components located close to the laser focus.

Bibliography

[1] R. Wilderøe. *Archiv Elektronik und Ubertragungstechnik*, **21**: 387, 1928.

[2] E. O. Lawrence. Methods and apparatus for the acceleration of ions. *United States patent office*, pages 1948384, 1929.

[3] W. I. Linlor. Ion energies produced by laser giant pulse. *Appl. Phys. Lett.*, **3**: 11, 1963.

[4] S. J. Gitomer *et al.* Fast ions and hot electrons in t he laser-plasma interaction. *Phys. Plasmas*, **29**: 8, 1986.

[5] D. W. Forslund and J. U. Brackbill. Magnetic-field-induced surface transport on laser-irradiated foils. *Phys. Rev. Lett.*, **48**: 1614, 1982.

[6] S. P. D. Mangles *et al.* Monoenergetic beams of relativistic electrons from intense laser plasma interactions. *Nature*, **431**: 535, 2004.

[7] C. G. R. Geddes *et al.* High-quality electron beams from a laser wakefield accelerator using plasma-channel guiding. *Nature*, **431**: 538, 2004.

[8] J. Faure *et al.* A laser plasma accelerator producing monoenergetic electron beams. *Nature*, **431**: 541, 2004.

[9] W. P. Leemans *et al.* GeV electron beams from a centimetre-scale accelerator. *Nature Physics*, **2**: 696, 2006.

[10] V. Malka *et al.* Electron acceleration by a wake field forced by an intense ultrashort laser pulse. *Science*, **298**: 5598, 2002.

[11] E. L. Clark *et al.* Measurements of energetic protons transport through magnetized plasma form intense laser interaction with solids. *Phys. Rev. Lett.*, **84**: 670, 2000.

[12] R. A. Snavely *et al.* Intense high energy proton beams from petawatt laser irradiation of solids. *Phys. Rev. Lett.*, **85**: 2945, 2000.

[13] A. Maksimchuk *et al.* Forward ion acceleration in thin films driven by a high-intensity laser. *Phys. Rev. Lett.*, **84**: 18, 2000.

[14] M. Borghesi *et al.* Measurements of highly transient electrical charging following high intensity laser solid interactions. *Appl. Phys. Lett.*, **82**: 1529, 2003.

[15] T. E. Cowan *et al.* Ultralow emittance, multi-MeV proton beams from a laser virtual-cathode plasma accelerator. *Phys. Rev. Lett.*, **92**: 20, 2004.

[16] S. Gaillard *et al.* Proton acceleration from ultra-high intensity short pulse laser matter interactions with Cu micro-cone targets at an intrinsic 10^{-8} contrast. *Journal of Physics: Conferesnce Series*, **244**: 022034, 2010.

[17] R. R. Wilson. Radiological use of fast protons. *Radiology*, **47**: 487, 1946.

[18] G. Kraft. Tumortherapy with ion beams. *Nucl. Instr. Methods Phys. Res. Sect. A; Accelerators, Spectrometer, Detectors and Associated Equipment*, **454**: 1, 2000.

[19] W. Wieszczycka and W. H. Schaf. *Proton radiotherapy accelerators*. River Edge, New Jersey: World Scientific Publishing Co Pte Ltd, 2001.

[20] U. Amaldi *et al.* LIBO-a linac booster for proton-therapy: construction and tests of a prototype. *Nucl. Instr. Methods Phys. Res. Sect. A; Accelerators, Spectrometer, Detectors and Associated Equipment*, **521**: 512, 2004.

[21] V. S. Khoroshkov and K. K. Onosovsky. State of the art in proton therapy techniques. *Instruments and Experimental Techniques*, **38**: 149, 1995.

[22] `http://ptcog.web.psi.ch/`.

[23] T. Kadkhoda *et al.* *Radiation Oncology*, **3**: 4, 2008.

[24] David Whelan and Robert Langreth. *Forbes Magazine*, March 2009.

[25] Varian Medical Systems. Palo Alto, California.

[26] S. V. Bulanov *et al.* Oncology hadrontherapy with laser ion accelerators. *Phys. Lett. A*, **299**: 240, 2002.

[27] S. V. Bulanov and V. Khoroshkov. Feasibility of using laser ion accelerators in proton therapy. *Plasmas Phys. Rep.*, **28**: 453, 2002.

[28] E. Fourkal and C. Ma. Laser accelerated carbon ion beams. *Medical Physics*, **30**: 1448, 2003.

[29] E. Fourkal *et al.* Energy and intensity modulated radiation therapy using laser accelerated proton beams. *Medical Physics*, **31**: 1884, 2004.

[30] V. Malka *et al.* Practicability of proton therapy using compact laser systems. *Medical Physics*, **31**: 1587, 2004.

[31] K. Krushelnick *et al.* Ultra-high intensity laser produced plasmas as a compact heavy ion injection source. *IEEE transactions on plasma science*, **28**: 1184, 2000.

[32] S. Fritzler *et al.* Proton beams generated with high intensity lasers: applications to medical isotope production. *Appl. Phys. Lett.*, **83**: 3039, 2003.

[33] R. Richards. *Dark Sun: The Making of the Hydrogen Bomb*. New York: Simon & Schuster, 1995.

[34] G. P. Thomson and M. Blackman. Improvements in or relating to gas discharge apparatus for producing thermonuclear reactions. *British patent office*, pages 817681, 1946.

[35] J. D. Lawson. Some criteria for a power producing thermonuclear reactor. *Proceedings of the Physical Society B*, **70**: 6, 1957.

[36] J. Nuckolls *et al.* Laser compression of matter to super-high densities: Thermonuclear applications. *Nature*, **239**: 139, 1972.

[37] M. Tabak *et al.* Ignition and high gain with ultra powerful lasers. *Phys. Plasmas*, **1**: 1626, 1994.

[38] M. Roth *et al.* Fast ignition by intense laser accelerated proton beams. *Phys. Rev. Lett.*, **86**: 436, 2001.

[39] N. S. P. King *et al.* An 800 MeV proton radiography facility for dynamic experiments. *Nucl. Instr. Methods Phys. Res. Sect. A; Accelerators, Spectrometer, Detectors and Associated Equipment*, **424**: 84, 1999.

[40] M. Roth *et al.* Energetic ions generated by laser pulses: a detailed study on target properties. *Phys. Rev. ST. Accel. Beams*, **5**: 061301, 2002.

[41] L. Romagnani *et al.* Dynamics of electric fields driving the laser acceleration of multi-MeV protons. *Phys. Rev. Lett.*, **95**: 195001, 2005.

[42] P. K. Patel *et al.* Isochoric heating of solid density matter with ultrafast proton beam. *Phys. Rev. Lett.*, **91**: 125004, 2003.

[43] C. L. Ellison and J. Fuchs. Optimizing laser-accelerated ion beams for a collimated neutron source. *Phys. Plasmas*, **17**: 113105, 2010.

[44] H. Ottevaere *et al.* Two-dimensional plastic microlens arrays by deep lithography with protons. *J. Opt. A: Pure and applied optics*, **4**: S22, 2002.

[45] I. Rajta *et al.* Proton beam micro machining on pmma, foturan and CR-39 materials. *Nucl. Instr. Methods Phys. Res. Sect. B: Beam interaction with materials and atoms*, **210**: 260, 2003.

[46] C. Debaes *et al.* Deep proton writing: a rapid prototyping polymer microfabrication tool for macro-optical modules. *New J. Phys.*, **8**: 270, 2006.

[47] F. Chen. *Introduction to plasma physics and controlled fusion, vol. 1: plasma physics.* Springer, 1983.

166

[48] P. Mora. Introduction aux plasmas créés par laser. *Lectures notes from the Ecole Polytechnique (unpublished)*, 2006.

[49] J. J. Thomson. Cathode rays. *Philosophical Magazine*, **44**: 293, 1897.

[50] I. Langmuir. Oscillations in ionized gases. *Proc. Nat. Acad. Sci. U.S.*, **14**: 8, 1928.

[51] J. M. Rax. *Physique des plasmas.* Dunod, 2005.

[52] J. C. Maxwell. A dynamical theory of the electromagnetic field. *Phil. Trans. Royal Soc. London*, **155**: 459–512, 1865.

[53] L. Spitzer and R. Härm. Transport phenomena in a completely ionized gas. *Phys. Rev.*, **89**: 5, 1953.

[54] L. V. Keldysh. Ionization in the field of a strong electromagnetic wave. *Sov. Phys. JETP*, **20**: 1307, 1965.

[55] V. Tikhonchuk. Interaction of a beam of fast electrons with solids. *Phys. Plasmas*, **9**: 1416, 2002.

[56] M. V. Ammosov *et al.* Tunnel ionization of complex atoms and of atomic ions in an alternating electromagnetic field. *Sov. Phys. JETP*, **64**: 6, 1986.

[57] P. Gibbon. *Short pulse laser interaction with matter, an introduction.* Imperial College Press, 2005.

[58] S. Eliezer. *The interaction of high-power lasers with plasmas.* Institute of Physics Publishing, 2002.

[59] P. Mora and T. Antonsen. Electron cavitation and acceleration in the wake of an ultra intense, self-focussed laser pulse. *Phys. Rev. E*, **53**: 3, 1996.

[60] A. Pukhov and J. M. ter Vehn. Relativistic magnetic self-channelling of light in near critical plasma. *Phys. Rev. Lett.*, **76**: 3975, 1996.

[61] M. Borghesi *et al.* Relativistic channelling of a picosecond laser pulse in near critical preformed plasma. *Phys. Rev. Lett.*, **78**: 879, 1997.

167

[62] S. C. Wilks *et al.* Absorption of ultrashort, ultra-intense laser light by solids and overdense plasmas. *IEEE Journal of Quantum Electronics*, **33**: 1954–68, 1997.

[63] F. Brunel. Not-so-resonant, resonant absorption. *Phys. Rev. Lett.*, **59**: 52, 1987.

[64] S. Kato *et al.* Wave breaking and absorption efficiency for short pulse p-polarized laser light in a very steep density gradient. *Phys. Fluids B; Plasma Physics*, **5**: 564, 1993.

[65] T. Ceccotti *et al.* Proton acceleration with high-intensity ultra high contrast laser pulses. *Phys. Rev. Lett.*, **99**: 185002, 2007.

[66] A. B. Langdon. Non linear inverse Bremsstrahlung and heated-electron distributions. *Phys. Rev. Lett.*, **44**: 575, 1980.

[67] Y. Ping *et al.* Absorption of short laser pulses on solid targets in the ultra relativistic regime. *Phys. Rev. Lett.*, **100**: 085004, 2008.

[68] J. Lindl. Development of the indirect-drive approach to inertial confinement fusion and target physics basis for ignition and gain. *Phys. Plasmas*, **2**: 3933, 1995.

[69] O. Lundh *et al.* Influence of shock waves on laser-driven proton acceleration. *Phys. Rev. E*, **76**: 026404, 2007.

[70] M. Passoni *et al.* Target normal sheath acceleration: theory comparison with experiments and future perspectives. *New J. Phys.*, **12**: 045012, 2010.

[71] S. C. Wilks *et al.* Energetic proton generation in ultra-intense laser solid interaction. *Phys. Plasmas*, **8**: 2, 2001.

[72] S. P. Hatchett *et al.* Electron, photon, and ion beams from the relativistic interaction of petawatt laser pulses with solid targets. *Phys. Plasmas*, **7**: 2076, 2000.

[73] A. Maksimchuk *et al.* High energy ion generation by short laser pulses. *Plasmas Phys. Rep.*, **30**: 6, 2004.

[74] M. Zepf *et al.* Fast particle generation and energy transport in laser-solid interactions. *Phys. Plasmas*, **8**: 5, 2001.

[75] Y. Murakami *et al.* Observation of proton rear emission and possible gigagauss scale magnetic fields from ultra-intense laser illuminated plastic target. *Phys. Plasmas*, **8**: 9, 2001.

[76] J. Fuchs *et al.* Comparison of laser ion acceleration from the front and rear surfaces of thin foils. *Phys. Rev. Lett.*, **94**: 045004, 2005.

[77] J. S. Green *et al.* Effect of laser intensity on fast-electron-beam divergence in solid-density plasmas. *Phys. Rev. Lett.*, **100**: 015003, 2008.

[78] J. J. Santos *et al.* Fast electron transport in ultra-intense laser pulse interaction with solid targets by rear-side radiation diagnostics. *Phys. Rev. Lett.*, **89**: 025001, 2002.

[79] A. R. Bell *et al.* Fast electron transport in high intensity short pulse laser solid experiments. *Plasma Phys. Control. Fusion*, **39**: 653, 1997.

[80] H. Alfvèn. On the motion of cosmic rays in interstellar space. *Plys. Rev.*, **55**: 425, 1939.

[81] A. J. Mackinnon *et al.* Enhancement of proton acceleration by hot-electron recirculation in thin foils irradiated by ultraintense laser pulses. *Phys. Rev. Lett.*, **88**: 215006, 2002.

[82] Y. Sentoku *et al.* High energy proton acceleration in interaction of short laser pulse with dense plasma target. *Phys. Plasma*, **10**: 2009–15, 2003.

[83] P. Mora. Plasma expansion into a vacuum. *Phys. Rev. Lett.*, **90**: 185002, 2003.

[84] P. Mora *et al.* Thin foil expansion into vacuum. *Phys. Rev. E*, **72**: 056401, 2005.

[85] A. P. L. Robinson *et al.* Effect of target composition on proton energy spectra in ultraintense laser-solid interactions. *Phys. Rev. Lett.*, **96**: 035005, 2006.

[86] J. Schreiber *et al.* Analytical model for ion acceleration by high-intensity laser pulses. *Phys. Rev. Lett.*, **97**: 045005, 2006.

[87] M. Passoni *et al.* Theory of light-ion acceleration driven by a strong charge separation. *Phys. Rev. Lett.*, **101**: 115001, 2008.

[88] M. Nishiuchi *et al.* The laser proton acceleration in the strong charge separation regime. *Phys. Lett. A*, **357**: 339, 2006.

[89] A. V. Gurevich *et al.* Self-similar motion of a rarefied plasma. *Soviet Physics JETP*, **22**: 449, 1966.

[90] A. V. Gurevich *et al. Soviet Physics JETP*, **36**: 274, 1972.

[91] J. Fuchs *et al.* Laser-driven proton scaling laws and new paths towards energy increase. *Nat. Phys.*, **2**: 48, 2006.

[92] J. Fuchs *et al.* Spatial uniformity of laser-accelerated ultrahigh-current MeV electron propagation in metals and insulators. *Phys. Rev. Lett.*, **91**: 255002, 2003.

[93] M. Kaluza *et al.* Influence of the laser prepulse on proton acceleration in thin foil experiments. *Phys. Rev. Lett.*, **93**: 045003, 2004.

[94] T. Fuji *et al.* MeV order proton and carbon ion acceleration by irradiation of 60 fs TW laser pulses on thin copper tape. *Appl. Phys. Lett.*, **83**: 1524, 2003.

[95] I. Spencer *et al.* Experimental study of proton emission from 60 fs 200 mJ high repetition rate tabletop laser pulses interacting with solid targets. *Phys. Rev. E*, **67**: 046402, 2003.

[96] H. Kishimura *et al.* Enhanced generation of fast protons from polymer coated metal foil by a femtosecond intense laser field. *Appl. Phys. Lett.*, **85**: 2736, 2004.

[97] I. Spencer *et al.* Beam interactions with materials and atoms: laser generation of proton beams for the production of short-lived positron emitting radioisotopes. *Nucl. Instr. and Meth. in Phys. Rev. B*, **183**: 449, 2001.

[98] P. McKenna *et al.* Characterization of proton and heavier ion acceleration in ultrahigh-intensity laser interactions with heated target foils. *Phys. Rev. E*, **70**: 036405, 2004.

[99] L. Robson *et al.* Scaling of proton acceleration driven by petawatt laser plasma interactions. *Nature Physics*, **3**: 58, 2007.

[100] M. Passoni *et al.* Charge separation effects in solid targets and ion acceleration with a two-temperature electron distribution. *Phys. Rev. E*, **69**: 0264011, 2004.

[101] M. Borghesi *et al.* Fast ion generation by high intensity laser irradiation of solid targets and applications. *Fusion Sci. Technol.*, **49**: 412, 2006.

[102] H. Ruhl *et al.* The generation of micro-fiducials in laser accelerated proton flows, their imaging property of surface structures and application for the characterization of the flow. *Phys. Plasmas*, **11**: L17, 2004.

[103] E. d'Humières *et al.* Proton acceleration mechanisms in high intensity laser interaction with thin foils. *Phys. Plasmas*, **12**: 062704, 2005.

[104] A. Pukhov. Three dimensional simulations of ion acceleration from a foil irradiated by a short pulse laser. *Phys. Rev. Lett.*, **86**: 3562, 2001.

[105] Y. Sentoku *et al.* High density collimated beams of relativistic ions produced by petawatt laser pulses in plasmas. *Phys. Rev. E*, **62**: 7271, 2000.

[106] A. J. MacKinnon *et al.* Effect of plasma scale length on multi-MeV proton production by intense laser pulses. *Phys. Rev. Lett.*, **86**: 1769, 2001.

171

[107] K. Nemoto *et al.* Laser triggered ion acceleration and table top isotope production. *Appl. Phys. Lett.*, **78**: 595, 2001.

[108] M. Allen *et al.* Direct experimental evidence of back-surface ion acceleration from laser-irradiated gold foils. *Phys. Rev. Lett.*, **93**: 265004, 2004.

[109] J. Fuchs *et al.* Comparative spectra and efficiencies of ions laser-accelerated forward from the front and rear surfaces of thin solid foils. *Phys. Plasmas*, **14**: 053105, 2007.

[110] M. Hegelich *et al.* MeV ion jets from short pulse laser interaction with thin foils. *Phys. Rev. Lett.*, **89**: 085002, 2002.

[111] M. Hegelich *et al.* Laser acceleration of quasi-monoenergetic MeV ion beams. *Nature*, **439**: 441–4, 2006.

[112] S. M. Pfotenhauer *et al.* Spectral shaping of laser generated proton beams. *New J. Phys.*, **10**: 033034, 2008.

[113] M. Schollmeier *et al.* Laser ion acceleration with micro-grooved targets. *Nucl. Instrum. Meth. Phys. Research A*, **577**: 186–190, 2007.

[114] M. Schollmeier *et al.* Laser beam-profile impression and target thickness impact on laser-accelerated protons. *Phys. Plasmas*, **15**: 053101, 2008.

[115] M. Roth *et al.* Laser accelerated ions and electron transport in ultra intense laser matter interaction. *Laser Part. Beams*, **23**: 95, 2005.

[116] M. Borghesi *et al.* Multi-MeV proton source investigations in ultra intense laser foil interaction. *Phys. Rev. Lett.*, **92**: 055003, 2004.

[117] J. Schreiber *et al.* Source size measurements and charge distributions of ions accelerated from thin foils irradiated by high intensity laser pulses. *Appl. Phys. B: Laser and Optics*, **79**: 1041, 2004.

[118] T. Esirkepov *et al.* Highly efficient relativistic-ion generation in the laser-piston regime. *Phys. Rev. Lett.*, **92**: 175003, 2004.

[119] A. P. L. Robinson *et al.* Radiation pressure acceleration of thin foils with circularly polarized laser pulses. *New J. Phys.*, **10**: 013021, 2008.

[120] G. Marx. Interstellar vehicle propelled by terrestrial laser beam. *Nature*, **211**: 22, 1966.

[121] A. Macchi *et al.* Light sail acceleration re-examined. *Phys. Rev. Lett.*, **103**: 085003, 2009.

[122] S. V. Bulanov *et al.* On the ion acceleration by high power electromagnetic waves in the radiation pressure dominated regime. *C. R. Physique*, **10**: 216–226, 2009.

[123] S. V. Bulanov *et al.* Neutrino oscillation studies with laser driven beam dump facility. *Nucl. Instr. Methods Phys. Res. Sect. A*, **540**: 25–41, 2005.

[124] S. V. Bulanov *et al.* Interaction of electromagnetic waves with plasma in the radiation dominated regime. *Plasma Phys. Reports*, **30**: 196–213, 2004.

[125] F. Pegoraro *et al.* Photon bubbles and ion acceleration in a plasma dominated by the radiation pressure of an electromagnetic pulse. *Phys. Rev. Lett.*, **99**: 065002, 2007.

[126] S. C. Wilks *et al.* Absorption of ultra intense laser pulses. *Phys. Rev. Lett.*, **69**: 9, 1992.

[127] A. Macchi *et al.* Laser acceleration of ion bunches at the front surface of overdense plasma. *Phys. Rev. Lett.*, **94**: 165003, 2005.

[128] L. O. Silva *et al.* Proton shock acceleration in laser plasma interaction. *Phys. Rev. Lett.*, **92**: 015002, 2005.

[129] T. Schlegel *et al.* Relativistic laser piston model: ponderomotive ion acceleration in dense plasmas using ultraintense laser pulses. *Phys. Plasmas*, **16**: 083103, 2009.

[130] X. Zhang *et al.* Effect of plasma temperature on electrostatic shock generation and ion acceleration by laser. *Phys. Plasmas*, **14**: 113108, 2007.

[131] A. P. L. Robinson *et al.* Relativistically correct hole-boring and ion acceleration by circularly polarized laser pulses. *Plasma Phys. Control. Fusion*, **51**: 024004, 2009.

[132] C. A. J. Palmer *et al.* Monoenergetic proton beams accelerated by a radiation pressure driven shock. *Phys. Rev. Lett.*, **106**: 014801, 2011.

[133] A. Henig *et al.* Radiation-pressure acceleration of ion beams driven by circularly polarized laser pulses. *Phys. Rev. Lett.*, **103**: 245003, 2009.

[134] A. Einstein. On the quantum theory of radiation. *Phys. Zs.*, **18**: 121, 1917.

[135] T. H. Maiman. Stimulated radiation in ruby. *Nature*, **187**: 4736, 1960.

[136] D. Strickland and G. Mourou. Compression of amplified chirped optical pulses. *Opt. Commun.*, **56**: 219, 1985.

[137] C. Ziener *et al.* Specular reflectivity of plasma mirrors as a function of intensity, pulse duration and angle of incidence. *J. Appl. Phys.*, **93**: 768, 2003.

[138] G. Doumy *et al.* Complete characterization of a plasma mirror for the production of high-contrast ultraintense laser pulses. *Phys. Rev. E*, **69**: 026402, 2004.

[139] B. Dromey *et al.* The plasma mirror: a subpicosecond optical switch for ultrahigh power lasers. *Rev. Sci. Inst.*, **75**: 645, 2004.

[140] C. Thaury *et al.* Plasma mirrors for ultrahigh-intensity optics. *Nature*, **3**: 424, 2007.

[141] R. Baumgartner *et al.* Optical parametric amplification. *IEEE Journal of Quantum Electronics*, **15**: 432, 1979.

[142] J. J. Thomson. Rays of positive electricity. *Proceedings of the Royal Society A*, **89**: 1–20, 1913.

[143] D. C. Carroll *et al.* A modified thomson parabola spectrometer for high resolution multi-MeV ion measurements: Application to laser driven ion acceleration. *Nucl. Instrum. Meth. Phys. Research A*, **620**: 23, 2010.

[144] `http://www.srim.org`.

[145] K. U. Akli *et al.* Temperature sensitivity of Cu Kα imaging efficiency using a spherical Bragg reflecting crystal. *Phys. Plasma*, **14**: 023102, 2007.

[146] S. D. Baton *et al.* Relativistic electron transport and confinement within charge-insulated, mass-limited targets. *HEDP*, **3**: 358–364, 2007.

[147] M. N. Quinn *et al.* Refluxing of fast electrons in solid targets irradiated by intense, picosecond laser pulses. *Plasma Phys. Control. Fusion*, **53**: 025007, 2011.

[148] X. H. Yuan *et al.* Spatially resolved x-ray spectroscopy using a flat HOPG crystal. *Nucl. Instr. and Meth. A*, pages doi:10.1016/j.nima.2010.12.147, 2011.

[149] R. Prasad *et al.* Calibration of thomson parabolaMCP assembly for multi-MeV ion spectroscopy. *Nucl. Instr. and Meth. A*, 2010.

[150] I. J. Paterson *et al.* Image plate response for conditions relevant to laser-plasma interaction experiments. *Meas. Sci. Technol.*, **19**: 095301, 2008.

[151] D. Neely *et al.* Enhanced proton beams from ultra-thin targets driven by high contrast laser pulses. *Applied Phys. Lett.*, **89**: 021502, 2006.

[152] D. C. Carroll *et al.* Carbon ion acceleration from thin foil targets irradiated by ultrahigh-contrast, ultraintense laser pulses. *New J. Phys.*, **12**: 045020, 2010.

[153] A. Andreev *et al.* Fast-ion energy-flux enhancement from ultra-thin foils irradiated by intense and high-contrast short laser pulses. *Phys. Rev. Lett.*, **101**: 155002, 2008.

[154] A. Andreev *et al.* Optimal ion acceleration from ultra-thin foils irradiated by a profiled laser pulse of relativistic intensity. *Phys. Plasma*, **16**: 013103, 2009.

[155] T. Esirkepov *et al.* Laser ion-acceleration scaling laws seen in multi-parametric particle-in-cell simulations. *Phys. Rev. Lett.*, **96**: 105001, 2006.

[156] P. McKenna *et al.* Low- and medium-mass ion acceleration driven by petawatt laserplasma interactions. *Plasma Phys. Control. Fusion*, **49**: B223–31, 2007.

[157] M. Hegelich *et al.* Spectral properties of laser-accelerated mid-Z MeV/u ion beams. *Phys. Plasmas*, **12**: 056314, 2005.

[158] W. Ehler *et al.* Effect of target purity on laser-produced plasma expansion. *J. Phys. D: Appl. Phys.*, **13**: 29–32, 1980.

[159] A. Zangwill. *Physics at surfaces*. Cambridge: Cambridge University Press, 1988.

[160] P. McKenna *et al.* Lateral electron transport in high-intensity laser irradiated foils diagnosed by ion emission. *Phys. Rev. Lett*, **98**: 145001, 2007.

[161] P. Gibbon. Efficient production of fast electrons from femtosecond laser interaction with solid targets. *Phys. Rev. Lett.*, **73**: 664–7, 1994.

[162] T. Baeva *et al.* The zero vector potential mechanism of attosecond absorption. *Phys. Plasma*, **18**: 056702, 2011.

[163] D. C. Carroll *et al.* Dynamic control and enhancement of laser-accelerated protons using multiple laser pulses. *C. R. Phys*, **10**: 188, 2009.

[164] P. McKenna *et al.* Effects of front surface plasma expansion on proton acceleration in ultraintense laser irradiation of foil targets. *Las. Part. Beams*, **26**: 591, 2008.

[165] S. Kar *et al.* Dynamic control of laser-produced proton beams. *Phys. Rev. Lett.*, **100**: 105004, 2008.

[166] T. Toncian *et al.* Ultrafast laser-driven microlens to focus and energy-select mega-electron volt protons. *Science*, **312**: 5772, 2006.

[167] M. Ikegami *et al.* Radial focusing and energy compression of a laser-produced proton beam by a synchronous rf field. *Phys. Rev. ST Accel. Beams*, **12**: 063501, 2009.

[168] D. C. Carroll *et al.* Active manipulation of the spatial energy distribution of laser-accelerated proton beams. *Phys. Rev. E*, **76**: 065401, 2007.

[169] K. Quinn *et al.* Laser-driven ultrafast field propagation on solid surface. *Phys. Rev. Lett*, **102**: 194801, 2009.

[170] M. Burza *et al.* Hollow microspheres as targets for staged laser-driven proton acceleration. *New J. Phys.*, **13**: 013030, 2010.

[171] T. Kluge *et al.* Enhanced laser ion acceleration from mass-limited foils. *Phys. Plasma*, **17**: 123103, 2010.

[172] S. Buffechoux *et al.* Hot electrons transverse refluxing in ultraintense laser-solid interactions. *Phys. Rev. Lett.*, **13**: 013030, 2010.

[173] O. Tresca *et al.* Controlling the properties of ultraintense laserproton sources using transverse refluxing of hot electrons in shaped mass-limited targets. *Plasma Phys. Control. Fusion*, **53**: 105008, 2011.

[174] X. H. Yuan *et al.* Effect of self-generated magnetic fields on fast-electron beam divergence in solid targets. *New J. Phys.*, **12**: 063018, 2010.

[175] E. Lescoute *et al.* Experimental observations and modelling of nanoparticle formation in laser-produced expanding plasma. *Phys. Plasmas*, **15**: 063507, 2008.

[176] E. Lescoute *et al.* Soft recovery technique to investigate dynamic fragmentation of laser shock-loaded metals. *Appl. Phys. Lett.*, **95**: 211905, 2009.

[177] E. Lescoute *et al.* Ejection of spalled layers from laser shock-loaded metals. *J. Appl. Phys.*, **108**: 093510, 2010.

[178] T. de Rességuier *et al.* Spallation in laser shock-loaded tin below and just above melting on release. *J. Appl. Phys.*, **102**:073535, 2007.

[179] J. E. Andrew *et al.* Operational experience of contamination and damage of the larger aperture optics in the HELEN laser facility vacuum system at 1053 and 527 nanometres. *SPIE proceedings*, pages 6720, 2007.

[180] J. E. Andrew and A. J. Comley. Characterisation of plasma mirrors on the HELEN laser infra red CPA beam. *SPIE proceedings*, pages 7132, 2008.

[181] J. E. Andrew and K. A. Wallace. The effects on glass surfaces of shrapnel and debris emissions from petawatt laser driven solid targets. *SPIE proceedings*, pages 7504, 2009.

[182] J. E. Andrew and K. A. Wallace. Characterisation of contaminant plumes arising from laser-solid target interactions. *SPIE proceedings*, pages 7842, 2010.

[183] B. Toftmann and J. Schou. Angular distribution of electron temperature and density in a laser-ablation plume. *Phys. Rev. Lett.*, **84**:17, 2000.

[184] P. E. Dyer. Electrical characterization of plasma generation in KrF laser Eu ablation. *Appl. Phys. Lett.*, **55**:1630, 1999.

[185] B Doggett and J. G. Lunney. Expansion dynamics of laser produces plasma. *J. Appl. Phys.*, **109**:093304, 2011.

[186] S. I. Anisimov *et al.* An analytical model for three-dimensional laser plume expansion into vacuum in hydrodynamic regime. *Appl. Surf. Sci.*, **96**:24, 1996.

[187] D. C. Swift *et al.* Laser-launched flyer plates for shock physics experiments. *Rev. Sci. Instr.*, **76**:093907, 2005.